

# Oil & Natural Gas Technology

DOE Award No.: DE-FE0028895

## Final Scientific/Technical Report

### Dynamic Behavior of Natural Seep Vents: Analysis of Field and Laboratory Observations and Modeling

Project Period (10/01/2016 to 09/30/2020)

Submitted by:  
Scott A. Socolofsky



---

Signature

Co-authors: B. Wang, B. Kim, and I. Jun

Texas A&M Engineering Experiment Station  
DUNS #:847205572  
3136 TAMU  
College Station, TX 77843-3136  
Email: socolofs@tamu.edu  
Phone number: (979) 845-4517

Prepared for:  
United States Department of Energy  
National Energy Technology Laboratory

Submitted 12/21/2020



U.S. DEPARTMENT OF  
**ENERGY**



NATIONAL  
ENERGY  
TECHNOLOGY  
LABORATORY

Office of Fossil Energy

DISCLAIMER:

This report was prepared as an account of work sponsored by an agency of the United States Government. Neither the United States Government nor any agency thereof, nor any of their employees, makes any warranty, express or implied, or assumes any legal liability or responsibility for the accuracy, completeness, or usefulness of any information, apparatus, product, or process disclosed, or represents that its use would not infringe privately owned rights. Reference herein to any specific commercial product, process, or service by trade name, trademark, manufacturer, or otherwise does not necessarily constitute or imply its endorsement, recommendation, or favoring by the United States Government or any agency thereof. The views and opinions of authors expressed herein do not necessarily state or reflect those of the United States Government or any agency thereof.

# Contents

<b>Executive Summary</b>	<b>11</b>
<b>1 Introduction</b>	<b>13</b>
<b>2 Analysis of NETL Water Tunnel Data</b>	<b>16</b>
2.1 Data analysis methods . . . . .	17
2.2 Mass transfer coefficients in absense of hydrate . . . . .	23
2.3 Mass transfer coefficients in the presence of hydrate . . . . .	31
<b>3 Hydrate Formation Time</b>	<b>34</b>
<b>4 Refinement and Validation of Natural Seep Numerical Model</b>	<b>40</b>
4.1 Numerical modeling methods . . . . .	40
4.2 Discrete particle model . . . . .	40
4.2.1 Fluid particle types: shape and circulation . . . . .	41
4.2.2 Equation of state for mixtures . . . . .	42
4.2.3 Slip velocity . . . . .	42
4.2.4 Mass Transfer . . . . .	43
4.3 Lagrangian particle model . . . . .	44
4.3.1 Trajectory of bubbles . . . . .	44
4.3.2 Dissolution of bubbles . . . . .	44
4.3.3 Adaptation based on the HPWT experiment conditions . . . . .	45
4.4 Validation of seep model to HPWT data . . . . .	45
4.4.1 Examples for no-hydrate cases . . . . .	45
4.4.2 Examples for cases with hydrate formation . . . . .	48
4.4.3 Quantification of model performance using HPWT dataset . . . . .	57
4.5 Application of seep model to GISR and other field data . . . . .	60
4.5.1 Gulf of Mexico . . . . .	61
4.5.2 Pakistan offshore in the Arabian Sea . . . . .	62
4.5.3 Data comparison method . . . . .	63
4.5.4 Results . . . . .	64
<b>5 Apply Seep Model to Interpret GISR Multibeam Data</b>	<b>68</b>
5.1 Application of seep model to GISR M3 data . . . . .	69

5.1.1	Calibration experiments in the OTRC wave basin . . . . .	69
5.1.2	M3 sonar calibration results . . . . .	71
5.1.3	Model to predict gas flow rate from M3 observations . . . . .	76
5.1.4	Further insights gained from the M3 field data . . . . .	78
5.2	Application of seep model to GISR EM 302 data . . . . .	87
<b>6</b>	<b>Summary and Conclusions</b>	<b>90</b>
<b>7</b>	<b>Impact Statement</b>	<b>93</b>
<b>A</b>	<b>Summary of Project Outcomes by Task and Subtask</b>	<b>99</b>
A.1	Task 1.0: Project Management Planning . . . . .	99
A.2	Task 2.0: Analyze NETL Water Tunnel Data . . . . .	99
A.3	Task 3.0: Synthesize GISR Field Data . . . . .	101
A.4	Task 4.0: Refine and Validate Seep Model . . . . .	102
A.5	Task 5.0: Conduct No-Hydrate M3 Calibration Experiment in OTRC . . . . .	104
A.6	Task 6.0: Apply Seep Model to GISR Multibeam Echosounder Data . . . . .	104
A.7	Task 7.0: Document Model Validation . . . . .	108
A.8	Task 8.0: Data Distribution / Archiving . . . . .	108
<b>B</b>	<b>Hydrate Formation Time and Bubble Size Distributions</b>	<b>111</b>
B.1	Introduction . . . . .	111
B.2	Hydrate Formation Time . . . . .	112
B.3	<i>In situ</i> Bubble Characteristics . . . . .	115
B.4	Digital Appendix . . . . .	116
B.4.1	Subtask 2.1 - Hydrate Formation Time . . . . .	117
B.4.2	Subtask 3.1 - <i>In situ</i> Bubble Characteristics . . . . .	118
<b>C</b>	<b>Tracking of Hydrate Crystals on Bubble Interfaces</b>	<b>119</b>
C.1	Methods . . . . .	119
C.2	Available Data . . . . .	121
C.3	Results . . . . .	123
C.4	Conclusions . . . . .	124
<b>D</b>	<b>Acoustic Measurements from the GISR Cruises</b>	<b>127</b>
D.1	Introduction . . . . .	127

D.2	Matlab Analysis Tools for <i>in situ</i> Acoustic Data . . . . .	128
D.2.1	Kongsberg EM 302 Multibeam Echo Sounder . . . . .	128
D.3	Kongsberg M3 Multibeam Echo Sounder . . . . .	131
D.3.1	Calibration of M3 using <i>in situ</i> camera observations . . . . .	135
D.3.2	Other quantitative aspects of the M3 data . . . . .	136
D.4	Comparison of Acoustic Measurements with Model Predictions . . . . .	138
D.5	Matlab Scripts . . . . .	141
D.6	Amplitude Level in EM Water Column Datagram . . . . .	142
<b>E</b>	<b>Rise Heights of Bubble Flares for the GISR Cruises</b>	<b>143</b>
<b>F</b>	<b>M3 Calibration Experiment in the Offshore Technology Research Center</b>	<b>147</b>
F.1	Introduction . . . . .	147
F.2	M3 Calibration . . . . .	148
F.3	Application of M3 to Laboratory Bubble Plumes . . . . .	149
F.4	<i>In Situ</i> Imaging of Laboratory Bubble Plumes . . . . .	150
F.5	Experimental Matrix . . . . .	152

## List of Figures

1	Project Timeline. . . . .	15
2	Example of image processing for HPWT experiments. . . . .	18
3	Comparison of image processing results between NETL and the present study. . . . .	20
4	Various bubble shrinkage rates using different data durations. . . . .	21
5	Error analysis of shrinkage rate data. . . . .	22
6	Training and validation statistics for analysis of mass transfer coefficient from the HPWT dataset. . . . .	25
7	Mass transfer rates for empirical and observed values in the HPWT dataset without hydrate shells: Calibration data. . . . .	27
8	Mass transfer rates for empirical and observed values in the HPWT dataset without hydrate shells: Validation data. . . . .	29
9	Mass transfer rates for empirical and observed values in the HPWT dataset with hydrate shells: All data. . . . .	32
10	Prediction of hydrate transformation time using the data in Rehder et al. (2009). . . . .	37
11	Model data comparison for simulation of the Rehder et al. (2009) dataset. . . . .	38
12	Validation plot of derived model for hydrate formation time. . . . .	39
13	Example system information from HPWT experiment on June 15, 2012. . . . .	46
14	TAMOC simulation for a CH <sub>4</sub> bubble in RO water. . . . .	46
15	Predicted variation of bubble density during a natural gas experiment in seawater. . . . .	47
16	TAMOC simulation of a natural gas bubble in seawater. . . . .	48
17	System information for the HPWT during an experiment on June 21, 2013. . . . .	49
18	Sample images of hydrated bubble for an experiment on June 21, 2013. . . . .	50
19	TAMOC simulation of a natural gas bubble compared to data for an experiment on June 21, 2013. . . . .	51
20	System information in the HPWT during an experiment on June 11, 2012. . . . .	53
21	Sample images of hydrated bubble for an experiment on June 11, 2012. . . . .	54
22	TAMOC simulation of a methane bubble with hydrate shell for an experiment on June 11, 2012. . . . .	54
23	System information for the HPWT during an experiment on March 13, 2014. . . . .	56
24	TAMOC simulation of an experiment in the HPWT for March 13, 2014. . . . .	56
25	Error quantification between TAMOC simulations and observed bubble shrinkage in the HPWT. . . . .	59

26	Computed acoustic target strength of a methane bubble under different acoustic forcing in the oceans. . . . .	60
27	Prediction of seep flare height compared to acoustic observations. . . . .	65
28	Model performance for predicting natural seep flare height as observed by multibeam sonar. . . . .	66
29	Photographs of the experimental setup in the OTRC. . . . .	70
30	Sample images of bubble generated by different diffusers in the OTRC. . . . .	71
31	Calibration procedure for the M3 in the OTRC experiments. . . . .	72
32	Sample sonar images during the calibration experiment in the OTRC. . . . .	73
33	Model fit for acoustic calibration of the M3 multibeam sonar. . . . .	73
34	Comparison between transmission directivity due to the combined transmitter and receiver (Tx+Rx) and due to the side lobe effect of beam forming pattern. . . . .	75
35	Measured bubble size distribution for two diffusers in the OTRC experiments. . . . .	77
36	Calculated target strength for gas bubble plume experiments in the OTRC basin. . . . .	78
37	Comparison of predicted and observed gas flow rate for bubble plumes in the OTRC experiments. . . . .	79
38	Example M3 acoustic images and seep model results for field experiments during the GISR cruises. . . . .	80
39	Lateral diffusivity of bubble flare spreading rate. . . . .	81
40	M3 sonar target strength and seep model prediction for GISR G07 Dive H1355. . . . .	83
41	G07 Dive H1353 at GC600 Mega plume . . . . .	84
42	M3 sonar target strength and seep model prediction for GISR G07 Dive H1354. . . . .	85
43	M3 sonar target strength and seep model prediction for GISR G07 Dive H1352. . . . .	86
44	Comparison between seep model prediction of acoustic target strength and observation from the EM 302 during the GISR Cruise G08 on Dive H1403. . . . .	88
45	Comparison between the measured and modeled acoustic data from the EM 302 multibeam sonar. . . . .	107
46	An example of time series of ambient conditions for a bubble before, during, and after hydrate formation. . . . .	113
47	An example of morphological change of a bubble before, during, and after hydrate formation. . . . .	114
48	Volumetric bubble size distribution for the measured data and a fitted log-normal distribution. . . . .	116
49	Measured rise velocity versus bubble size. . . . .	117

50	High-speed camera image for two adjacent frames of the video sequence. . . . .	120
51	Speed of moving hydrate plates on a pure methane bubble recorded on May 18, 2012 for the first bubble. . . . .	123
52	Speed of moving hydrate plates on a pure methane bubble recorded on June 11, 2012 for the third bubble. . . . .	124
53	Speed of moving hydrate plates on a pure methane bubble recorded on June 29, 2012 for the third bubble. . . . .	125
54	Sample plot of the EM 302 water column data during one ping. . . . .	129
55	Visualization of seeps along the ship track during the total of 388 pings. . . . .	130
56	Profile of target strength for the seep of interest showing in Figure 55 . . . . .	131
57	Example of an M3 sonar image. . . . .	132
58	Cumulative distribution function of relative intensity of the bubble scattering shown in Figure 57. . . . .	133
59	Time series of M3 sonar operation during a profiling survey, including the survey at the seep source and flare tracking through the water column. . . . .	134
60	Comparison between the calculated target strength obtained from bubble character- istics observed by the <i>in situ</i> cameras and the calculated sonar intensity from the M3 acoustic imaging. . . . .	135
61	Range-averaged relative intensity of bubble scattering in the M3 sonar field-of-view after removing all noise (signal < -25 dB). . . . .	137
62	Histogram of relative intensity of bubble scattering in the Sonar field-of-view after removing all noise (signal < -25 dB). . . . .	137
63	Comparison of the observed acoustic backscatter from the EM 302 with the predicted target strength of bubbles as a function of height from a simulation of the same flare using our numerical model. . . . .	138
64	Comparison of the M3 raw acoustic backscatter after thresholding to remove noise to the predicted target strength of bubbles at each measured height from a simulation of the same flare using our numerical model. . . . .	140
65	Combined surveys of bubbles emanating from the Sleeping Dragon vent (Woolsey Mound) in MC 118 during the G07 (July 2014) cruise. . . . .	144
66	Combined surveys of bubbles emanating from the Sleeping Dragon vent (Woolsey Mound) during the G08 cruise. . . . .	146
67	Tungsten carbide calibration sphere. . . . .	148
68	Acoustic image from M3 of the calibration sphere at a single location. . . . .	149

69 Acoustic image from M3 of an airstone bubble plume at 3.0 NI/min gas flow rate at 12.0 m above the source. . . . . 150

70 Acoustic image from M3 of a natural seep flare at MC 118 imaged at 190 m above the sea floor (700 m depth). . . . . 151

71 CCD video camera image of an airstone bubble plume at 3.0 NI/min gas flow rate at 11.45 m above the source. . . . . 151

72 Bubble size distribution for an airstone bubble plume at 3.0 NI/min gas flow rate at 11.45 m above the source. . . . . 152

## List of Tables

1	Statistics of the training and validation datasets for gas bubbles without hydrate in the HPWT. . . . .	26
2	Summary of goodness-of-fit statistics for the training and validation datasets with various points removed. . . . .	30
3	Parameters for each bubble release case and the statistical analysis of the performance of the developed model. . . . .	35
4	Summary of the simulation results for the prediction of flare rising height . . . . .	67
5	Measured flow rate and median bubble diameter for each case. . . . .	70
6	Summary of data repositories for GISR cruises G07 and G08. . . . .	110
7	Summary of individual CH <sub>4</sub> and C1C2C3 bubble observations . . . . .	112
8	Table of experiments in the NETL High-pressure Water Tunnel having high-speed image data. . . . .	122
9	The combined survey periods for acoustic surveys during the G07 cruise. . . . .	143
10	The combined survey periods for acoustic surveys during the G08 cruise. . . . .	144

## Executive Summary

By: Scott A. Socolofsky, Binbin Wang, Byungjin Kim, and Inok Jun

In this project, we have analyzed data collected by the U.S. Department of Energy (DOE), National Energy Technology Laboratory (NETL) in a high pressure water tunnel (HPWT) and data from two research cruises to natural seeps in the Gulf of Mexico to adapt and validate a numerical model to predict the dynamics of natural seeps in the deep oceans. The HPWT data include video observations of the shrinkage rate of individual methane and natural gas bubbles under simulated deep-water conditions. Field data were collected during two cruises by the Gulf Integrated Spill Research (GISR) Consortium led by Texas A&M University and funded by the Gulf of Mexico Research Initiative (GoMRI). These data included *in situ* observations from a remotely operated vehicle (ROV) of gas bubbles at two natural seep sites in the Gulf and acoustic observations of the natural seep bubble flares in the ocean water column. The acoustic data were from multibeam echosounders, one mounted in a forward-looking orientation on the ROV and another mounted down-looking in the haul of the ship. All of these laboratory and field data were focused on the dynamics of natural gas bubbles at temperatures and pressures favorable for clathrate hydrate formation between the gas and water.

Our analyses of this data focused on understanding the mechanisms responsible for gas bubble dissolution within the hydrate stability zone (HSZ) of the oceans. Ice-like hydrate shells may form on the bubble-water interface under these conditions, and it was unknown how this might affect the mass transfer of gas into the ocean. We were able to extract bubble shrinkage rates from the HPWT datasets. Using this data we determined that mass transfer coefficients with and without a hydrate shell match empirical values for bubbles in contaminated systems (so-called dirty bubbles, coated in naturally occurring, dissolved surfactants in the water). Using these mass transfer coefficients, our numerical model of bubble dissolution matched the over 200 HPWT experiments with an average error of 10% for predicting the bubble size at the end of an experiment. This is a very good level of performance for this integrative metric.

From field data in the literature, we also observed that gas bubbles dissolve faster when they are initially released, following mass transfer coefficients for so-called clean-bubbles (those not yet contaminated by surfactants). Shortly after release within the HSZ, a hydrate shell forms on the bubble-water interface, and the mass transfer reduces to rates matching those of dirty bubbles. We correlated this transition time from clean to dirty bubble behavior with the initial bubble surface area and the hydrate sub-cooling, given by the temperature difference between the ambient water

and the temperature of hydrate formation.

With this model for hydrate formation time and using the mass transfer coefficients deduced from the HPWT data, we validated our numerical model for predicting the rise heights of natural seep flares in the oceans. Flare heights are commonly observed in haul-mounted acoustic multibeam data. The numerical model predicts bubbles to rise high in the ocean water column owing to the slower mass transfer rates for dirty bubbles that accompany the majority of their rise time. We found that the numerical model predictions matched the observed flare heights within 5% to 10% accuracy when we compared the rise heights of the largest bubbles released from the seafloor with the multibeam data. Bubbles become acoustically transparent as they shrink to sizes of order 1 mm in diameter for the multibeam frequencies used in the field. Hence, the predicted rise heights were the depths at which these largest gas bubbles shrank to about 1 mm in diameter.

The forward-looking multibeam on the ROV also provided data on the lateral spreading of bubbles in natural seep flares. Our analysis of this data showed that spreading follows a diffusion process, with the effective diffusivity correlating with the wobbling length scale of these ellipsoidal bubbles. When we apply this diffusivity in a random displacement model of bubble spreading, our numerical simulations match closely the lateral spread observed by the M3 in the ocean water column.

Finally, we compared the seep model predictions for the cross-sectionally integrated acoustic backscatter in these natural seep plumes with that observed by the acoustic instruments in the field. The M3 and EM 302 observations were converted to relative values of target strength using a calibration we obtained in the laboratory for the M3 and using an algorithm from the manufacturer for the EM 302. Comparing the model to these data, we obtain good agreement over the whole height of rise of these bubble flares. This further validates the numerical model and also reinforces our conclusions for observed rise height that natural seep flares are observed to disappear when bubbles become smaller than the resonant bubble size in an acoustic beam. Overall, our validated seep model captures the key dynamics of gas bubbles released from natural seeps in the oceans and helps to predict the fate of methane in the water column.

## 1 Introduction

The *overarching goal* of this project was to develop a computer model to predict the trajectory and dissolution of hydrate-armored methane bubbles originating from natural seeps. The model is based on the Texas A&M Oilspill (Outfall) Calculator (TAMOC), developed by Dr. Socolofsky, and which has been refined and validated through this project to explain fundamental laboratory and field observations of methane bubbles within the gas hydrate stability zone of the ocean water column. *Our approach* was to synthesize fundamental observations from the National Energy Technology Laboratory’s (NETL) High-Pressure Water Tunnel (HPWT) and field observations from the Gulf Integrated Spill Research (GISR) seep cruises (cruises G07 and G08), conducted by the PIs in the Gulf of Mexico, to determine the dissolution pathways and mass transfer rates of natural gas bubbles dissolving in the deep ocean water column. We sought to achieve these objectives by pursuing the *following specific objectives*:

1. Analyze existing data from the NETL HPWT (see Section 2).
2. Synthesize data from the GISR natural seep cruises (see Section 5 and Appendix B).
3. Refine and validate the seep model to predict available data (see Section 4).
4. Demonstrate the capability of the seep model to interpret multibeam data (see Section 5).

Ultimately, the *main outcome and benefit* of this work was to clarify the processes by which hydrate-coated methane bubbles rise and dissolve into the ocean water column, which is important to predict the fate of methane in the oceans, to understand the global carbon cycle, and to understand how gas hydrate deposits are maintained and evolve within geologic and oceanic systems, both at present baselines and under climate-driven warming.

The data sources used by this project include both the laboratory data collected by NETL and field data collected by the PI’s as part of the GISR consortium. NETL conducted experiments for single gas bubbles in their HPWT facility (Warzinski, Shaffer, Lynn, Haljasmaa, Schellhaas, Anderson, Velaga, Leifer and Levine, 2014; Levine et al., 2015). This included experiments with pure methane and with a natural gas mixture and for pressures above and below the threshold for hydrate formation. In many experiments, regardless of the pressure, hydrates did not form; in some experiments, hydrates did form as a coating on the bubble-water interface. Most experiments were conducted at constant pressure, and in some experiments, the pressure was reduced to simulate the rise of a bubble through the ocean water column. The raw data collected by the HPWT facility includes operational time series of the water tunnel pressure, temperature, and flow rate as well as

camera images of the gas bubbles suspended in the expanding, counterflow section of the HPWT measurement window. Our main goal in this project was to analyze this data to understand what information it contains about gas dissolution from rising bubbles with and without hydrate shells and to use this data to improve and validate the natural seep module (single bubble model) of TAMOC.

Similar data to that obtained in the HPWT was also collected during the GISR G07 and G08 cruises to natural seeps in the Gulf of Mexico. The project PI's developed a stereoscopic, high-speed camera system (Wang and Socolofsky, 2015a; Wang et al., 2016) which they deployed from the ROV *Hercules* from the *E/V Nautilus* to both observe hydrate formation on natural seep bubbles and to measure bubble sizes and rise velocity. They conducted experiments in 2014 (cruise G07) in Mississippi Canyon lease block 118 (MC 118) at Woosley Mound and in Green Canyon lease block 600 (GC 600); they returned to MC 118 in 2015 (cruise G08). Other measurements during these cruises included forward-looking multibeam sonar using a Kongsberg M3 mounted on the ROV and haul-mounted multibeam sonar using a Kongsberg EM 302 mounted on the exploration vessel. Chemical analyses were also conducted on free gas and water samples collected within and around the bubble columns rising from these natural seeps. Data collected during the G07 cruise were reported in Wang et al. (2016); this project further analyzed the data from the G08 cruise. Our main goal in using this data was to compare observations from the HPWT with those from the field, to further validate the TAMOC single bubble model, and to apply the TAMOC model to interpret multibeam acoustic data for natural seeps.

Figure 1 shows the project time line with each of the tasks and subtasks identified in the Project Management Plan (PMP). A complete accounting of the work conducted for each task and subtask is provided in Appendix A. Each of the project deliverables are provided in Appendices B through F.

The main body of this report focuses on the key outcomes of the project. The initial tasks of the project during Budget Period 1 (Tasks 2 and 3) were to assemble the HPWT and GISR field data, analyze them to extract their raw data products, and to extract the quantitative insights contained in these data that are independent of the seep model. The main outcome of these activities was evaluation of the bubble mass transfer coefficient and dissolution model from the HPWT data, detailed here in Section 2. We also used the GISR field data and data from the literature to compute the formation time of hydrate on the bubble water interface (Section 3). Following the extraction of these data, we used the mass transfer coefficients obtained from the HPWT data throughout Budget Period 2 to validate the TAMOC seep model to the HPWT and GISR field data (Task 4). In Section 4, we show that the model has good skill to reproduce the laboratory

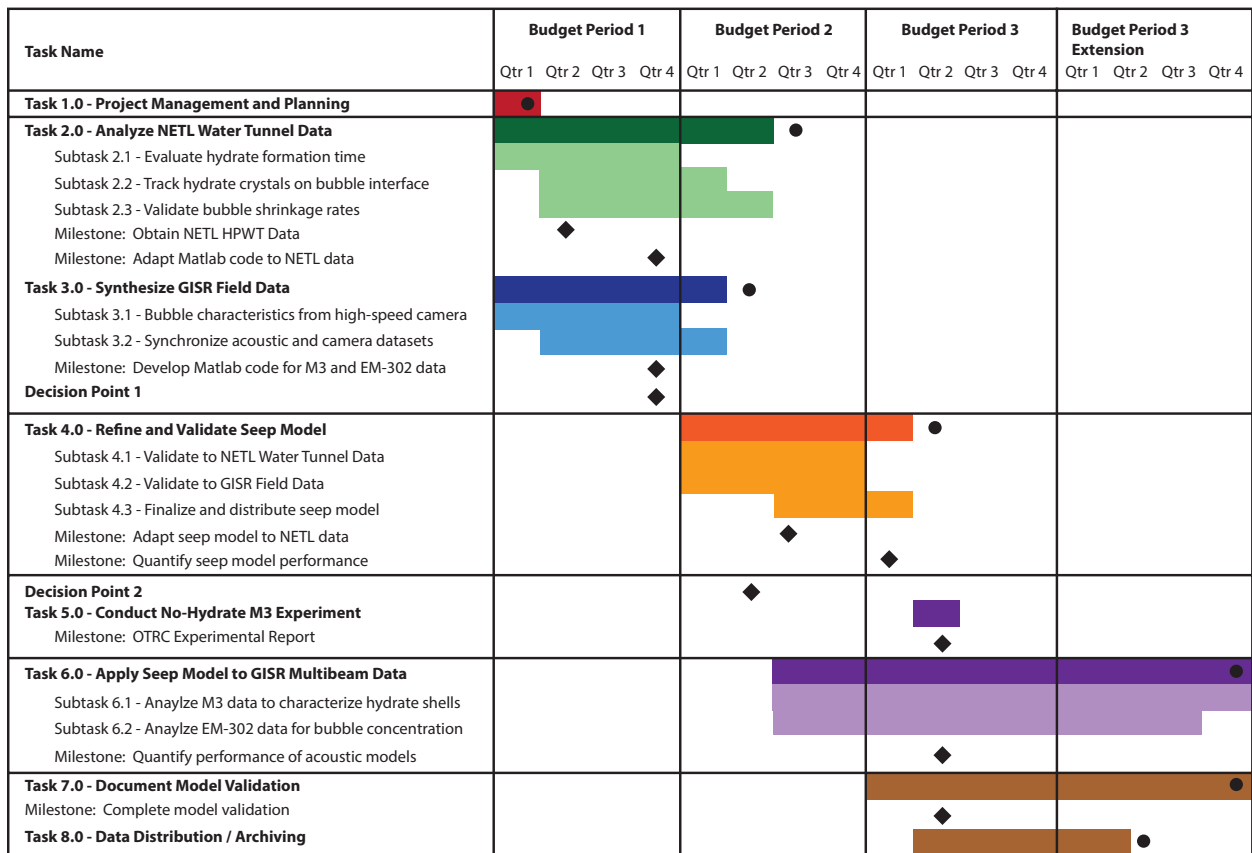


Figure 1: Project Timeline.

and field data, including experiments with hydrate skins on the bubbles, provided that the hydrate sub-cooling is less than  $11^{\circ}\text{C}$  or that the pressure reduces to simulate rise through the ocean water column. To extract quantitative data from the M3 multibeam sonar, we conducted a calibration experiment in the Offshore Technology Research Center (OTRC) during Budget Period 3 (Task 5; see Appendix F), and used that data together with a Kongsberg calibration for the EM 302 during the full period of Budget Period 3 and its extension, to validate the seep model to the GISR acoustic field data (Task 6). We report good agreement between the acoustic properties of simulated natural seep bubble columns and the field observations in Section 5. This final effort of the project was also recently reported in Wang et al. (2020). This report concludes with a summary of the major findings in Section 6 and the project impact statement in Section 7.

## 2 Analysis of NETL Water Tunnel Data

We obtained a complete set of the NETL HPWT data from DOE at the beginning of our project. This dataset was previously described by Warzinski, Shaffer, Lynn, Haljasmaa, Schellhaas, Anderson, Velaga, Leifer and Levine (2014) and Warzinski, Lynn, Haljasmaa, Leifer, Shaffer, Anderson and Levine (2014), and included high-speed and standard video images, camera calibration data, and time series of system operating parameters, including temperature, pressure, and water tunnel flow rate. We analyzed this data to validate the bubble shrinkage rates published by NETL in Warzinski, Shaffer, Lynn, Haljasmaa, Schellhaas, Anderson, Velaga, Leifer and Levine (2014), to investigate hydrate formation time, and to track hydrate crystals on the interfaces of bubbles in the high-speed camera data. From the observed shrinkage rates, we further evaluated the mass transfer coefficient and dissolution model appropriate for the HPWT for pure bubbles and bubbles with hydrate shells.

Bubbles were injected into the HPWT by slowly filling an inverted cup that was then rotated to release the complete bubble. We report the hydrate formation times in Appendix B, but because this gas filling time was relatively long and occurred very close to the hydrate stability pressure, it was not possible to develop a relationship between hydrate formation time and the experimental parameters. Instead, we used data from the literature and our own field experiments (GISR G07 and G08 cruises) to develop a predictive equation for the time required to coat a free gas bubble with hydrate under hydrate-forming conditions. Analysis of this data is presented in Section 3.

Tracking of hydrate crystals on the interfaces of bubbles as hydrates formed or dissociated provided insight on the mobility of the bubble-water interface. The results of our analyses are presented in Appendix C. We found that during hydrate formation, large plates of hydrate could

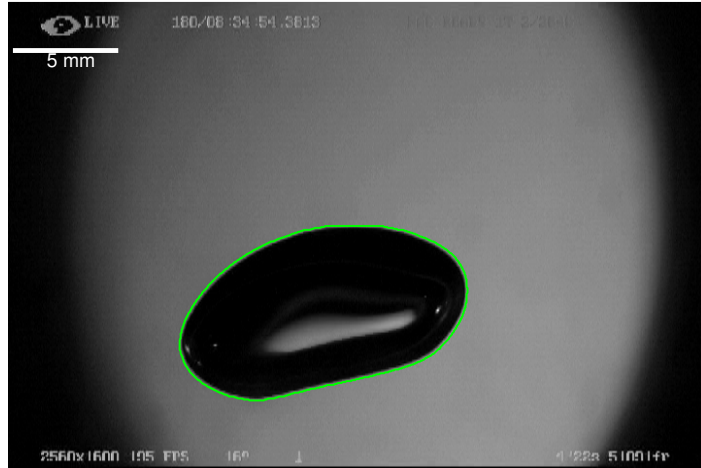
move across the leading face of a bubble at speeds approaching the rise velocity of the bubbles (about 20 cm/s). Hydrate plates at the lee edge of bubbles and hydrate particles forming during dissociation did not move, but appeared to float on an immobile bubble-water interface. From these observations, we conclude that bubbles in the HPWT may have mobile interfaces early in the experiments, but that for later times, bubble-water interfaces become immobilized. These two types of behavior generally correlate with clean bubble mass transfer processes (mobile interfaces) and dirty bubble mass transfer (immobile interfaces) (Clift et al., 1978). Interfaces generally become immobilized by the generation of Marangoni forces as surfactants build up on the bubble-water interface, causing a surfactant gradient from the leading edge to lee of the bubble. This observation is revisited below as we analyze the mass transfer coefficients.

In the remainder of this section, we discuss our analysis of the bubble shrinkage rates observed in the HPWT, our data on hydrate formation time taken from field observations, and our evaluation of the mass transfer rates for pure and hydrate-coated bubbles in the NETL HPWT.

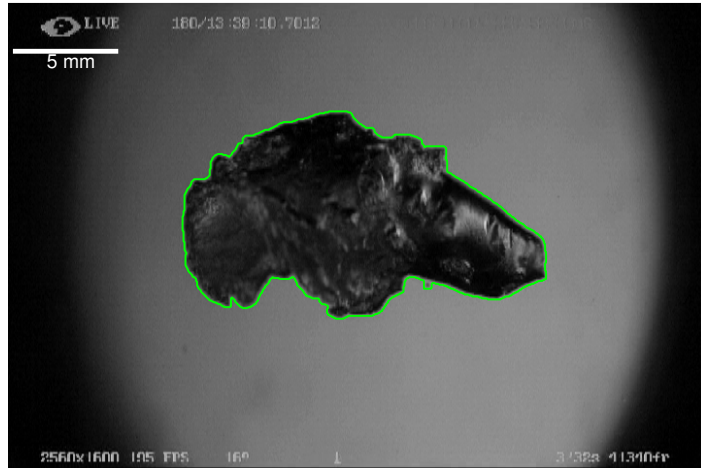
## 2.1 Data analysis methods

The raw data from the HPWT for bubble size include camera images of the bubbles, the camera calibration information, and the image timing. Bubble size is computed by identifying the bubble in the camera image and converting its apparent area to an equivalent spherical diameter.

We use the Matlab image processing tool box to identify the edge of the bubble in each sequential video frame. Figure 2 shows an example result of our image processing methods for one pure methane bubble and one methane bubble with a complex hydrate surface. The video images are saved in color (RGB) format. We convert these to grayscale using the Matlab function `rgb2gray()`. We then find the edge of the bubble using the Matlab function `edge()` using the Canny method applied to the grayscale image. We use the `edge()` function iteratively, increasing the threshold value by three times for the second pass. The edge detected by this method may be discontinuous and may contain holes. We use the Matlab function `imdilate()` with two line stencils (each with length 5 pixels and both orthogonal to each other) to create connected objects where the edges may be incomplete. To fill in holes, we use the `imfill()` function with the `fill` option. We remove small objects that may still remain identified in the image and that do not correspond to the bubble using the Matlab function `bwareaopen()` with a threshold value of 2000 pixels. The final object may still be connected to other identified objects (e.g., the shadow region); we remove these using the `imclearborder()` function with a pixel connectivity value of 4. The boundary line plotted in Figure 2 is extracted using the Matlab function `bwboundaries()` with the parameter `noholes` applied to the final image of our image processing chain.



(a) 1st bubble on June 28th 2012: pure methane bubble



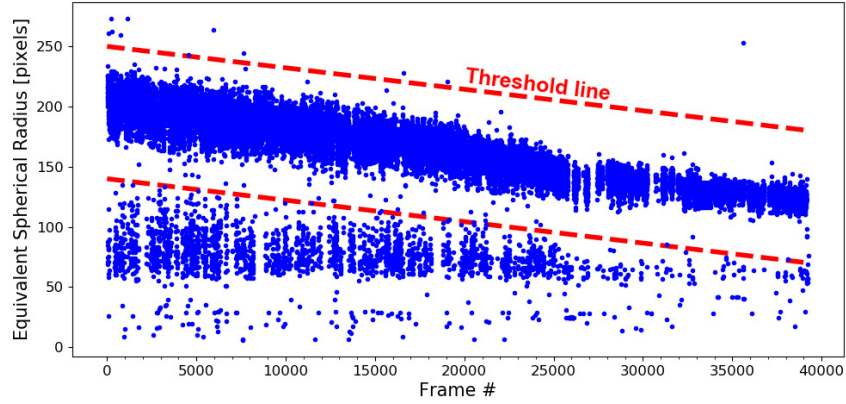
(b) 2nd bubble on June 28th 2012: methane bubble with complex hydrate shell.

Figure 2: Grayscale video images from the HPWT experiments with the identified bubble object (green line) using our Matlab image processing analysis methods.

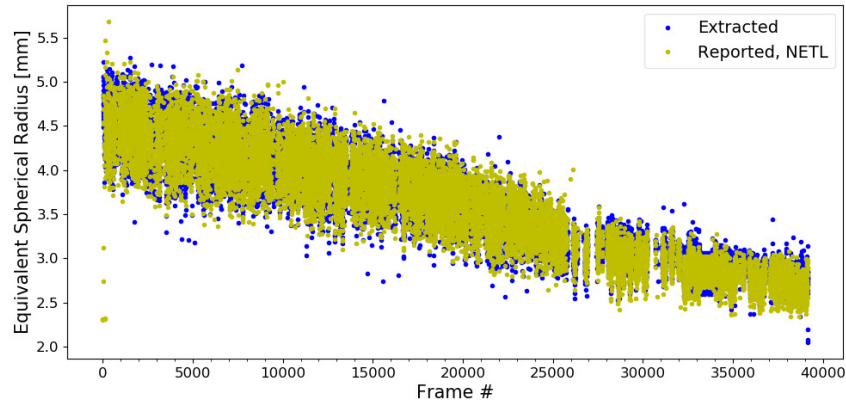
We extract the statistics of the identified bubbles using the Matlab `regionprops()` function, which returns results for the area, centroid, perimeter, major and minor axis length, orientation, and eccentricity. In the multiphase literature, the size of an irregularly-shaped particle is normally reported using the equivalent spherical diameter, which is the diameter of a sphere having the same volume. In the two-dimensional images analyzed here, the true shape, hence, the volume, of the bubble is unknown. Two common approaches are to either create an object of revolution having the cross-section shown in the image or to use the major and minor axis lengths to compute the volume of an ellipsoid. Wang and Socolofsky (2015*b*) shows for air bubbles at room temperature that both of these methods are slightly different for ellipsoidal wobbling bubbles, with errors in volume in the range of 5% to 10%. Here, we use the `EquivDiameter` property returned by `regionprops()`, which uses the pixel area of revolution method.

Figure 3 shows the results of our image processing algorithm applied to an image sequence of a pure methane bubble. Figure 3(a) shows the raw output of our Matlab image processing algorithm. The true bubble size shrinks over time and is identified within the region of results between the two, red threshold lines. Spurious, much smaller bubble sizes are identified when the bubble moves in the field of view to overlap the shadow region or to exit the camera field of view. We remove these data using the threshold values shown in the figure. In Figure 3(b), we compare our image processing results to the equivalent bubble sizes reported by NETL in Warzinski, Shaffer, Lynn, Haljasmaa, Schellhaas, Anderson, Velaga, Leifer and Levine (2014). The small differences result from different choices in the image-processing algorithm, but are negligible compared to the variability of the measured value.

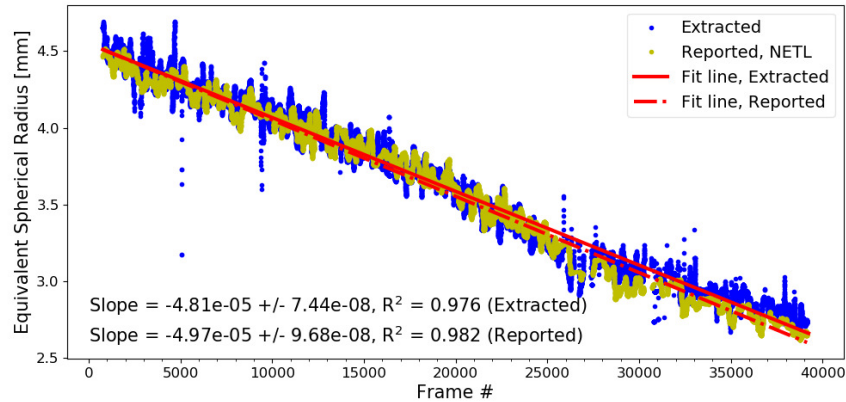
The bubble sizes identified by our image-processing algorithm vary over short time periods (e.g., create the wide cloud of data in Figure 3(b)) for two main reasons. First, the bubbles are large, in the ellipsoidal-wobbling size range, so that they have interfacial waves traveling about their bubble-water interfaces and their shapes are constantly varying. Although the volume remains constant, the complex bubble shape cannot be fully extracted from a single camera viewpoint. Second, the present data were obtained using one camera, which suffers from parallax error, instead of using a stereoscopic setup. As the bubble moves closer to the camera, it appears larger, and vice versa as it moves away. We use a constant magnification of 0.0024 mm/pixel for the data in Figure 3 to convert the pixel areas to real bubble sizes. Hence, even for perfectly spherical bubbles, their computed sizes would fluctuate due to parallax error as they move around the sample volume. Together, these effects give a measurement uncertainty for the equivalent bubble diameter of about 0.5 mm out of 4.5 mm, or about 10%. Because the bubble moves throughout the sample volume, we may assume that the parallax error eventually cancels. Figure 3(c) shows the result using a



(a) Extracted bubble size data from MATLAB image processing methods. Only data within the threshold lines are considered. Image calibration is 0.0024 mm/pixel.



(b) Comparison between the extracted data using our tool and that reported by NETL (Warzinski, Shaffer, Lynn, Haljasmaa, Schellhaas, Anderson, Velaga, Leifer and Levine, 2014).



(c) Bubble sizes for a 100-frame moving average (symbols), including the NETL-reported data and a best-fit line.

Figure 3: Comparison of the present data post-processing results for the same bubble as Figure 2 with those reported previously by NETL (Warzinski, Shaffer, Lynn, Haljasmaa, Schellhaas, Anderson, Velaga, Leifer and Levine, 2014).

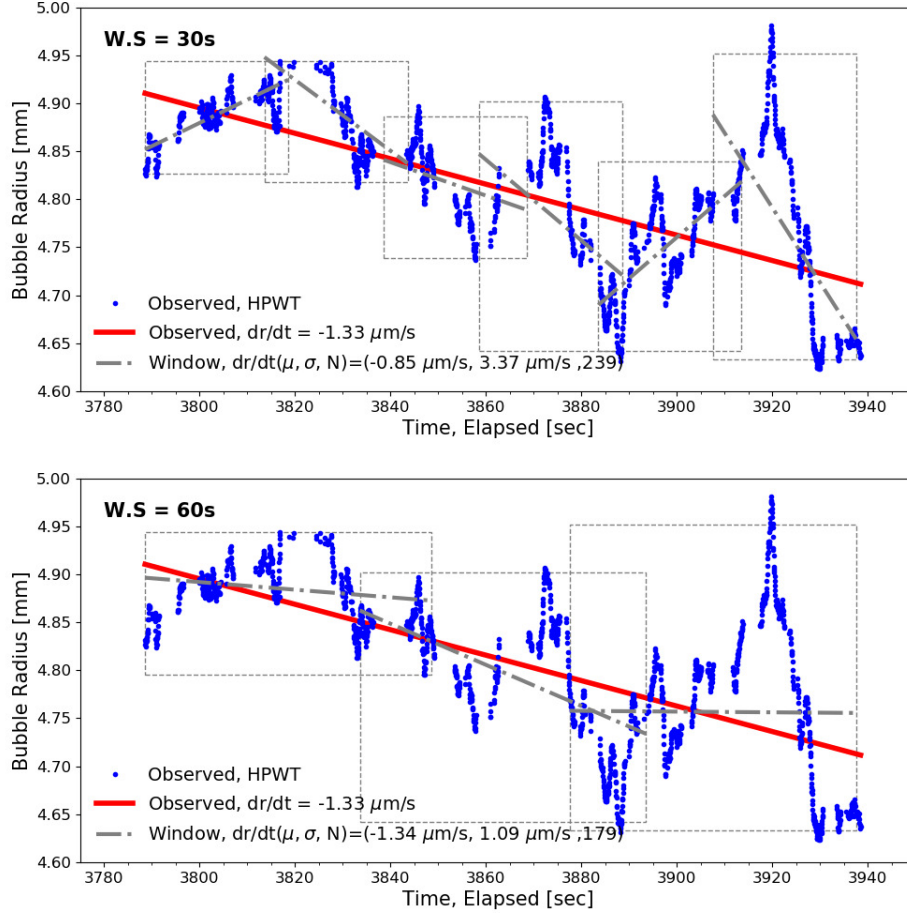


Figure 4: Best-fit lines for shrinkage rate using moving windows (gray dash-dot lines) of 30 s (upper panel) and 60 s (lower panel); best-fit lines for entire measurement sequence shown in red solid line.

100-frame moving average. The best-fit linear regression lines for the NETL (dash-dot) and our (solid) image processing results are also shown. The slopes of these lines, which give the shrinkage rates, are very similar, equal to  $-(4.8 \pm 0.2) \cdot 10^{-5}$  mm/frame.

On closer inspection, the frame-to-frame results for bubble sizes vary gradually, with consecutive estimates for bubble size largely in agreement. Figure 4 shows a short sequence of data for a pure methane bubble recorded on May 11, 2012. The blue dots show the frame-by-frame results; gaps occur when the bubble moves out of the frame or overlaps the shadow region. In the figure, it is apparent that there are short-term, minor fluctuations in computed bubble size overlain on gradual oscillations in the size estimates. Over longer times, the trend is toward bubble shrinkage. The short-term, minor fluctuations likely correlate closely with minor errors due to the irregular shapes of bubbles as interfacial waves traverse their surfaces and they rotate on their axes. The more gradual oscillations result from the bubble wandering throughout the measurement volume,

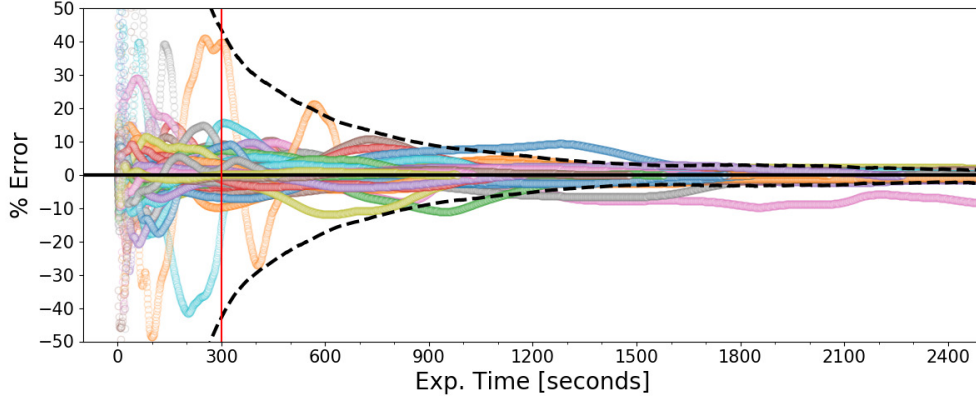


Figure 5: Error analysis for shrinkage rate using different window sizes compared to the shrinkage rate of the whole time sequence (colored symbols). The dashed line represents the ensemble average % Error,  $(\Gamma_{fit} - \Gamma_{95})/\Gamma_{fit}$ . A window size of 300 s (red vertical line) is taken as the minimum sequence size necessary to obtain convergence of shrinkage rate within an error bound of  $\pm 40\%$ .

sometimes being located closer to the camera, and sometimes farther away. For a long period of measurement, as in Figure 3, these fluctuations are much shorter than the measurement period, and are averaged out by the best-fit lines. In other experiments, shorter measurement periods were used, and it became important to determine the minimum measurement period necessary to have converged statistics for bubble shrinkage rate.

To this end, we fitted lines to different periods of the measured time series of bubble size. Figure 4 shows this method applied using two different data sizes: in the upper figure, a data window-size of 30 s was used, in the lower figure, the window-size was 60 s. The figure shows the best fit line using all of the data (red solid line), and best fit lines for groups of data equal to the various window sizes (gray dash-dot lines). For the shorter window sizes, the slopes of each estimate are highly variable, not even agreeing from fit-to-fit on the sign of the slope (shrinkage or growth). For longer window sizes, the slope estimates become more stable. We also compared the statistics of the slopes for the various fitted lines using different window sizes. Using any window size, the average of all slope estimates (shrinkage rates) does agree with the shrinkage rate of the overall best-fit line. However, for shorter window sizes, the variation of these slope estimates (standard deviation) is greater than for longer window sizes.

Figure 5 summarizes the errors using different window sizes for all of the measured data for pure methane bubbles. The  $x$ -axis reports the window size in seconds and the the  $y$ -axis the percentage error of the slope estimates for each sub-window compared to the slope obtained using the whole dataset. The dashed line in the figure shows the 95% confidence interval on bubble shrinkage rate as a function of the window duration used in the regression analysis. Beginning at about 300 s, the

shrinkage rate data become accurate to an error of  $\pm 40\%$ . This duration also agreed with Fourier transform analysis of the time-series of bubble size, and corresponds to about 50 to 100 times the peak oscillation frequency in the data.

Based on this analysis, we applied our Matlab image processing algorithm to compute time series of bubble sizes for all experiments in the NETL HWPT dataset. We included only experiments with duration greater than 300 s in our analysis on bubble shrinkage rate and, hence, mass transfer rates. From these data we could compute the mass transfer rates for pure bubbles (no hydrate) and hydrate-coated bubbles in the HWPT experiments, as described below.

## 2.2 Mass transfer coefficients in absence of hydrate

Over 200 different experiments (video sequences of bubble dynamics) were conducted in the NETL HPWT for gas bubbles without a hydrate shell and with greater than 300 s of data. These include a few experiments at pressures below the hydrate stability pressure, with most experiments conducted at pressures above the hydrate stability pressure. For these experiments within the hydrate stability zone, hydrates did not form when the background dissolved gas concentration was below a necessary threshold, usually, saturation or slight super-saturation concentration for the hydrate-water equilibrium point. Under those conditions, crystals of hydrate could form in the water phase and act as nucleation sites to initiate hydrate growth on the bubble-water interface. In this section, we only consider those experiments for which the dissolved gas concentration was low enough that hydrate shells did not form, yielding mass transfer rates for pure gas bubbles in the absence of hydrate.

**Mass Transfer Model.** As explained in the methods above, the raw camera images were analyzed to compute bubble equivalent spherical diameter  $d_e$  as a function of time  $t$ , and linear regression was used to compute the best-fit slope for the shrinkage rate, yielding a calculated value for  $dd_e/dt$ . To relate these shrinkage rate measurements to the mass transfer coefficient of each bubble, a dissolution model is required. We assume the mass transfer is limited by the water phase (gas is always available from the gas phase at the bubble-water interface), which is normally modeled by the mass transfer equation

$$\frac{dm_i}{dt} = -A\beta_i(C_{s,i} - C_{a,i}) \tag{1}$$

where the subscript  $i$  represents each chemical component in the gas mixture,  $m_i$  is the mass of each component in the bubble,  $A$  is the surface area of the bubble,  $\beta_i$  is the mass transfer coefficient for each component in the bubble,  $C_{s,i}$  is the solubility of component  $i$ , and  $C_{a,i}$  is the concentration of

component  $i$  in the ambient fluid, far away from the bubble. This equation averages the non-uniform mass transfer over the whole surface of the bubble.

The mass loss rate  $dm_i/dt$  is related to the bubble shrinkage rate through the density  $\rho$  and volume  $V$ . Using the chain rule, we have

$$\frac{dm}{dt} = \frac{d(\rho V)}{dt} = V \frac{d\rho}{dt} + \rho \frac{dV}{dt} \quad (2)$$

When the HPWT is operated at constant pressure and temperature, and neglecting changes in gas density as the composition changes (which would only change in the natural gas bubbles over longer experimental times), we can neglect  $d\rho/dt$ . Substituting  $V = (\pi d_e^3)/6$ , we have

$$\frac{dm}{dt} = \rho \frac{d}{dt} \left( \frac{\pi d_e^3}{6} \right) = \frac{\pi \rho d_e^2}{2} = \frac{\rho A}{2} \frac{dd_e}{dt} \quad (3)$$

where we have used the surface area of a sphere  $A = \pi d_e^2$ . Hence, we may directly relate the measured shrinkage rates in the HPWT ( $dd_e/dt$ ) to the mass transfer coefficients in Equation (1) if we know the density of the bubble, the ambient gas concentration, and the saturation concentration at the bubble-water interface.

The gas density is a thermodynamic property that depends on the gas composition, the temperature, and the pressure. We assume thermal equilibrium between the gas and surrounding water in the HPWT system. The operational temperature and pressure are available as a function of time in the NETL dataset. Here, we use the Peng-Robinson cubic equation of state with volume translation to compute the gas bubble density from the given composition and thermodynamic state (Gros et al., 2016). Likewise, the system ambient gas concentration was also measured and reported by NETL.

To determine the saturation concentration in Equation 1, we must decide on the phase of each constituent that is dissolving and use an appropriate equation of state. In the case of bubbles without a hydrate shell, it is the free gas that is dissolving, and we use the same Peng-Robinson equation of state to estimate the solubility of gasses in the bubble at the bubble-water interface (Gros et al., 2016). When a hydrate shell begins to form, further mass transfer may either be from the free gas inside the bubble or from the hydrate phase on the bubble-water interface. We address this question later in Section 2.3. Hence, for pure gas bubbles without hydrates, all of the necessary variables in Equation (1) are known thermodynamic properties or were observed in the camera images; we compute these properties using the Peng-Robinson equation of state available in the TAMOC modeling suite (Gros et al., 2016; Dissanayake et al., 2018) and compare observed mass transfer (shrinkage rate) with predictions using empirical equations for mass transfer coefficient.

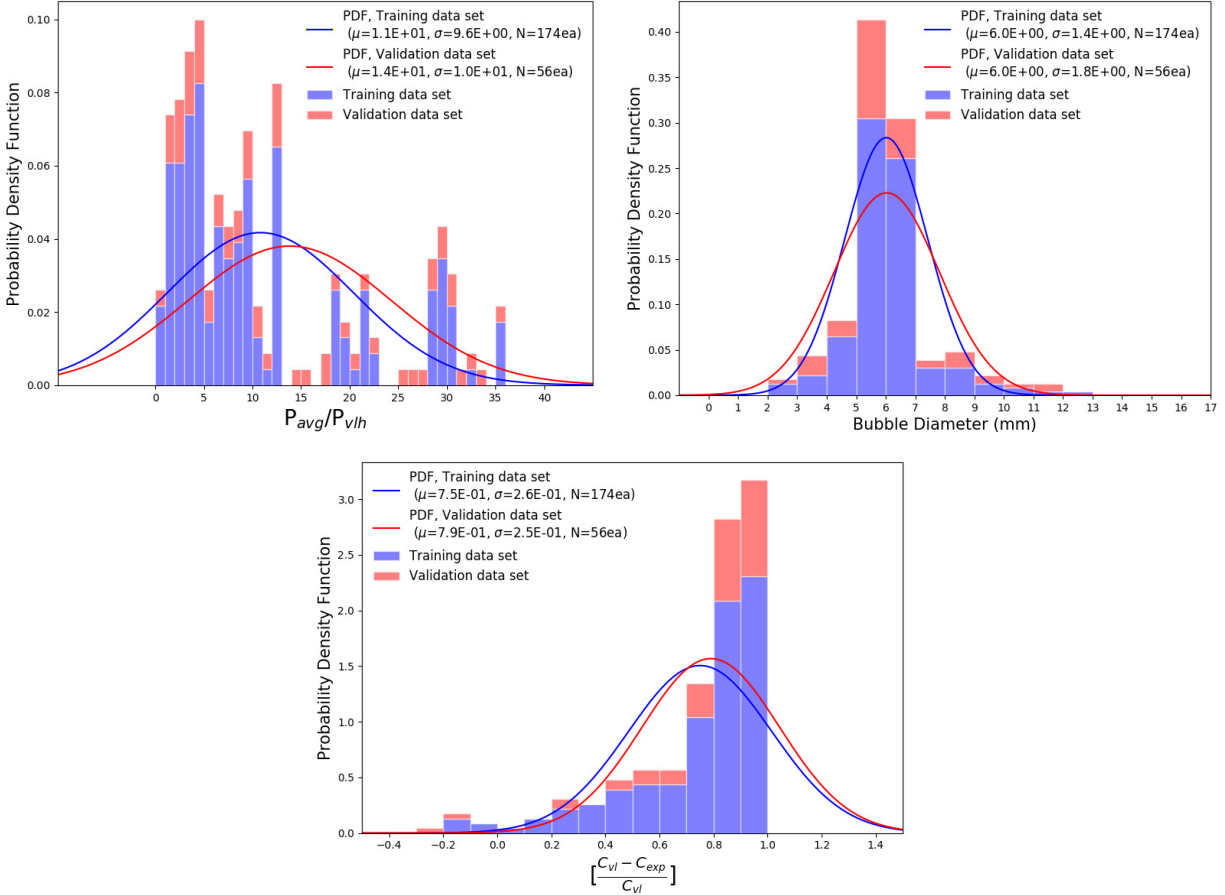


Figure 6: Graphical presentation of the statistics of the training and validation datasets for gas bubbles in the HPWT.

**Training and Validation Datasets.** We compute the best-fit mass transfer rate using the computed bubble shrinkage rates in the HPWT experiments and the dissolution model in Equation 1. To make this estimate, we stratify the dataset of 230 experiments on gas bubbles without hydrate into a training set for estimating  $\beta$  and a validation set to test our best-fit  $\beta$ .

We separate the full dataset into training and validation data using the system pressure as the stratification parameter and a random-split function. Figure 6 Shows the statistics of the training and validation data sets for their average pressure, bubble diameter, and ambient concentration. In the figure, each bar represents the total number of experiments within a given range, the blue-shaded region, the fraction of data used in the training dataset, and the red-shaded region, the fraction of data used in the validation dataset. We also plot a Gaussian fit to each dataset, which helps to confirm that the training and validation datasets each have very similar statistics. Table 1 shows further characteristics of the training and validation datasets, including the numbers of experiments conducted with pure methane (C1), natural gas (C123), and with different ambient

Table 1: Statistics of the training and validation datasets for gas bubbles without hydrate in the HPWT.

Gas <sup>1</sup>	Water <sup>2</sup>	# Total	# Training	# Validation	% Ratio [ $\frac{\#Training}{\#Total}$ ]
C1	RO	97	79	18	81
C123	RO	24	14	10	58
C123	SW	95	73	22	77
C123	SW + D	14	8	6	57
<b>Total</b>		230	174	56	76

<sup>1</sup> Bubbles were composed of pure methane (C1) or a natural gas mixture of methane, ethane, and propane (C123).

<sup>2</sup> Ambient water consisted of reverse osmosis water (RO), artificial seawater (SW), or artificial seawater with added dispersant (SW + D).

fluids, including reverse-osmosis water (RO), artificial seawater (SW) and seawater plus dispersant (SW + D). From these statistics, the training and validation datasets are shown to have very similar composition with respect to system thermodynamic state, gas bubble size and composition, and ambient water type.

**Mass Transfer Coefficients in HPWT.** Using the training dataset, we estimate the mass transfer coefficient using the computed shrinkage rate data. We perform this analysis using  $dm/dt$  as the fit variable rather than  $\beta$  because of the form of the mass transfer equation, Equation (1). Consider the solution for  $\beta$  given by

$$\beta = -\frac{dm/dt}{A(C_s - C_a)}. \quad (4)$$

This equation become undefined as  $C_s$  approaches  $C_a$ , and many HPWT experiments were conducted close to this condition. Also, the state variable directly computed from the measurements is  $dd_e/dt$ , which is directly related to  $dm/dt$ ; hence, it would be the most reliable to fit to this parameter rather than any other, more distant, derived parameter. Hence, we compute  $dm/dt$  from the measured data using Equation (3) and the density of gas estimated from TAMOC.

To compute the best-fit value of  $\beta$ , we compare the value of  $dm/dt$  measured in the HPWT using Equation (3) to a value computed using the mass transfer equation, Equation (1). We compute the right-hand-side of Equation (1) using the equations of state in TAMOC and an empirical model for  $\beta$ . Empirical equations for  $\beta$  depend on the composition of the bubble, its size and hydrodynamic properties, and whether the interface is clean or dirty. Here, we use mass transfer models from Clift

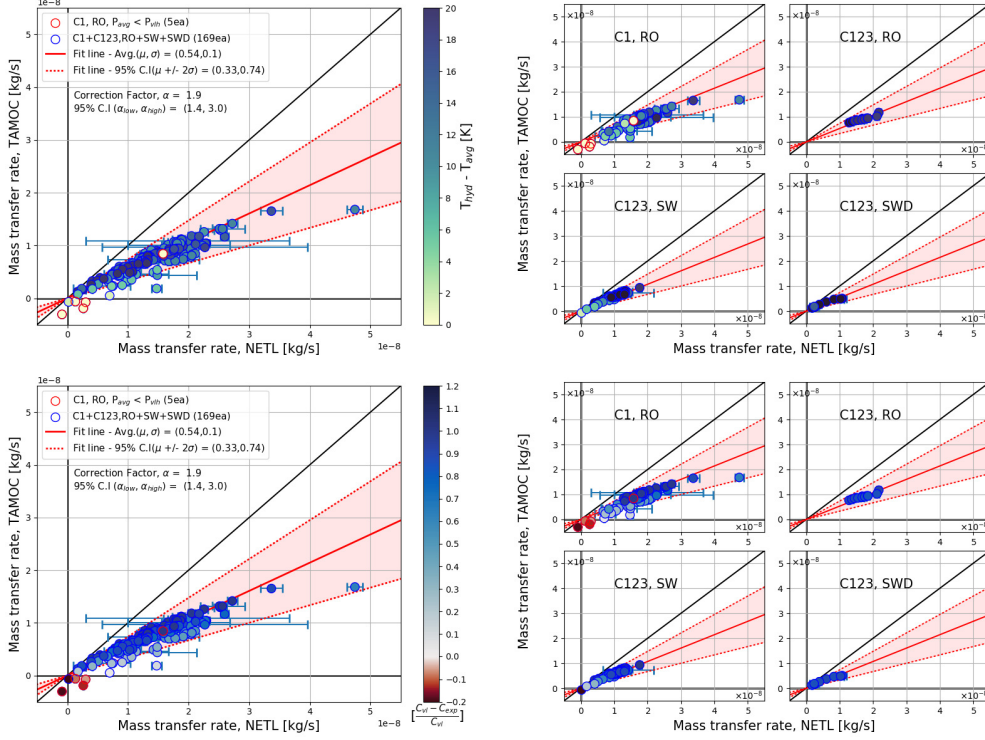


Figure 7: Mass transfer loss rates  $(dm/dt)_{TAMOC}$  versus  $(dm/dt)_{NETL}$  for the training dataset. The two left-hand plots present all of the data; plots on the right-hand-side are for different gases and water systems. The upper row of plots are colored by the experimental sub-cooling; the lower row of plots are colored by the degree of gas saturation in the ambient water.

et al. (1978), which are readily available in the TAMOC modeling system. Hence, we compare

$$\left. \frac{dm}{dt} \right|_{NETL} = \frac{\rho A}{2} \frac{dd_e}{dt} \quad (5)$$

where  $\rho$  is the density of gas computed using the equations of state in TAMOC, to

$$\left. \frac{dm}{dt} \right|_{TAMOC} = \beta_{emp} A (C_s - C_a) \quad (6)$$

where  $\beta_{emp}$  are the empirical mass transfer coefficients from Clift et al. (1978) as implemented in TAMOC,  $A$  is the average measured value for each experiment ( $\pi \bar{d}_e$ ) as evaluated by our image processing algorithm,  $C_s$  is computed from the equations of state in TAMOC for the given, initial gas composition and thermodynamic state, and  $C_a$  is reported in the HPWT dataset.

Figure 7 presents a comparison of these two mass transfer rates for each experiment in the training dataset. The black, 45°-line would give a perfect agreement between the empirical and observed mass loss rates. The data in Figure 7 instead show that the observed mass loss rates are faster than those predicted from the empirical equation; however, the offset between the observed and empirical values is consistent and well-correlated. We tested empirical mass transfer models for

both clean and dirty bubbles. The results in the figure are for dirty bubbles, as they are closer in agreement to the observations than the results using clean empirical mass transfer models. Because the observed data lie below the 45°-line, the mass transfer rates in the NETL HPWT are slightly faster than those predicted using dirty mass transfer coefficients. This could be expected since mass transfer equations are derived for bubbles rising in quiescent water; whereas, the conditions surrounding the bubbles in the HPWT are for turbulent pipe flow, where mixing may be enhanced.

In the upper row of plots in Figure 7, it is apparent that the degree of correlation between the observed and empirical mass loss is independent of the sub-cooling (the difference between the hydrate formation temperature  $T_{hyd}$  at the given system pressure and the ambient temperature  $T_{ave}$ ), and is consistent across all gas types and ambient water used. In the bottom row of plots, it is evident that the experimental cases with negative empirical mass loss are all for experiments conducted with dissolved gas concentration above the saturation concentration predicted by TAMOC (red-colored symbols). These conditions were only used in a few pure methane experiments, and the the empirical and observed mass loss values for these few experiments do not agree well. This disagreement stems from the very low mass loss rates (hence, larger uncertainty in the observed value of  $dm/dt$ , which is close to zero) and from the fact that the sign of the empirical value is very sensitive to estimating the saturation concentration accurately. In previous work, we have validated that the saturation predictions by TAMOC are within a 5% error for methane bubbles at a range of temperatures and pressures. This small error only become important in the present analysis as the ambient concentration approaches saturation. For the bulk of the experiments in under-saturated conditions, where the bubbles were observed to shrink, there is good correlation between an empirical mass loss rate and that observed.

The red, best-fit curve in the plots of Figure 7 provides the correction factor that adjusts literature values for the empirical mass transfer coefficient to the values observed in the HPWT. The shaded region in each plot shows the 95% confidence interval. We call the slope of this correlation line  $\alpha$ , such that

$$\beta_{NETL} = \alpha\beta_{emp} \tag{7}$$

where  $\beta_{NETL}$  is the mass transfer coefficient appropriate to the HPWT experiments. For the training dataset, we compute the best-fit value of  $\alpha = 1.9$ , with the 95% confidence interval spanning  $\alpha = (1.4, 3.0)$ .

Figure 8 shows the comparison of the mass loss rates observed in the HPWT to the empirical values for the validation dataset. In the figure, the red line is identical to that in Figure 7 (i.e., we do not fit a second regression). From Figure 8, we see that most points lie within the 95%

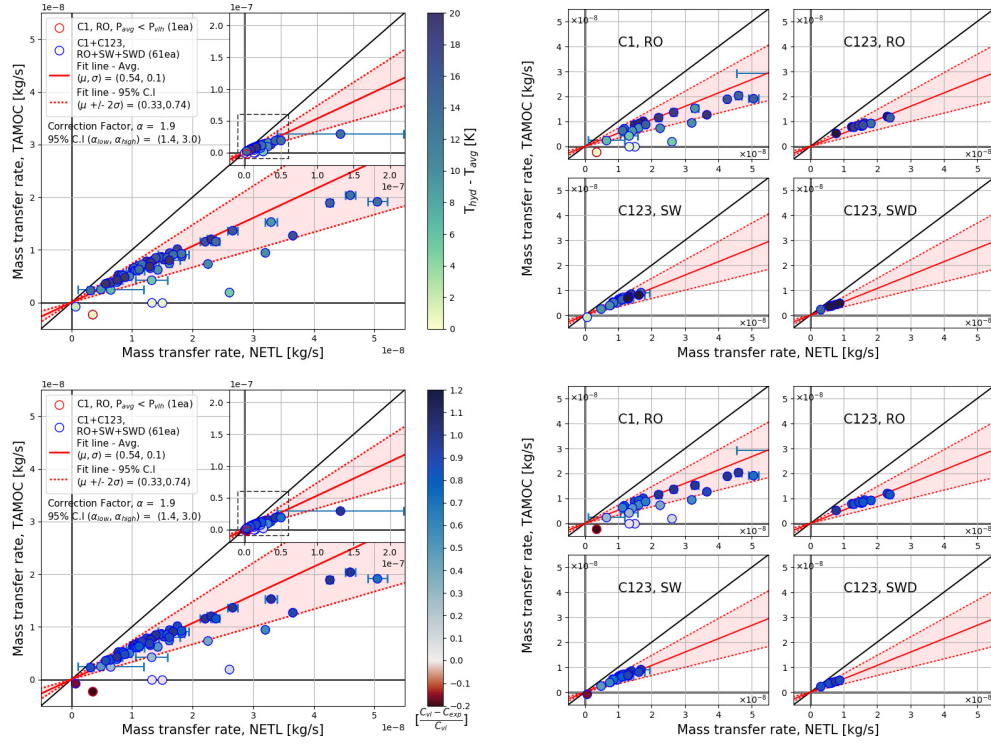


Figure 8: Mass transfer loss rates  $(dm/dt)_{TAMOC}$  versus  $(dm/dt)_{NETL}$  for the validation dataset. The two left-hand plots present all of the data; plots on the right-hand-side are for different gases and water systems. The upper row of plots are colored by the experimental sub-cooling; the lower row of plots are colored by the degree of gas saturation in the ambient water.

Table 2: Summary of goodness-of-fit statistics for the training and validation datasets with various points removed.

Case	Pearson	% Error	Sample#
Training set	0.90	19.71	173
Training set, excluding supersaturation points (5ea)	0.90	13.68	168
Validation set	0.85	37.17	63
Validation set, excluding an outlier (1ea)	0.86	36.83	62
Validation set, excluding supersaturation points (5ea)	0.89	15.03	58
Validation set, excluding an outlier and supersaturation points (6ea)	0.90	14.26	57

confidence interval of the training dataset, and we find that each of the conclusions from Figure 7 equally apply: the results are biased toward faster mass transfer in the observations than the empirical models, results are largely independent of the gas type, sub-cooling, and ambient water, and the results do not correlate well when the ambient dissolved gas concentration approaches the saturation concentration. Figure 8 does have a few more outliers than observed in the training set. For the second row of figures, these appear to correlate with conditions where the background gas concentration was close to saturation, but the observed mass loss rate was not small. Overall, the model developed through the training set remains valid for the validation data.

We report the statistics of our estimates of  $\beta_{NETL}$  in Table 2. We use the Pearson correlation coefficient  $PCC$ , given by

$$PCC = \frac{COV(X_m, X_{cal})}{\sigma_{X_m} \sigma_{X_{cal}}} \quad (8)$$

where  $COV$  is the coefficient of variation,  $X_m$  is the observed mass transfer rate,  $X_{cal}$  is the mass transfer rate computed using  $\beta_{NETL} = 1.9\beta_{emp}$  and  $\sigma_{X_m}$  and  $\sigma_{X_{cal}}$  are the standard deviations of  $X_m$  and  $X_{cal}$ , respectively. We also report the mean percentage error between the observed and computed mass transfer rates using

$$\%Error = \frac{1}{n} \sum_{i=1}^n \left| \frac{X_m^i - X_{cal}^i}{X_m^i} \right| \cdot 100\%. \quad (9)$$

$PCC$  is a measure of the linear correlation between two variables  $X_m$  and  $X_{cal}$ . It has a value between +1 and -1, where 1 is total positive linear correlation, 0 is no linear correlation, and -1 is total negative linear correlation. From the table, the overall best performance of our model for  $\beta_{NETL}$  is for the training set with the super-saturated points removed, giving a  $PCC = 0.9$  and an overall percentage error of 14% for 168 data points. The validation set with the super-saturated points removed have nearly identical performance, with  $PCC$  slightly lower, at 0.89, and percentage error slightly higher, at 15%. It is normally expected for the performance to be slightly less for the validation data compared to the training data. Overall, this degree of correlation is very good, and the error metrics are quite low for mass transfer calculations; hence, we conclude that the

mass transfer rates for gas bubbles in the HPWT can be predicted using empirical mass transfer coefficients for dirty bubbles multiplied by an amplification factor of 1.9, with a 90% confidence interval spanning (1.4, 3.0).

### 2.3 Mass transfer coefficients in the presence of hydrate

The previous section considered experiments at pressures both above and below the hydrate stability pressure, but in all cases, hydrates did not form on the bubble-water interface. Additional experiments were conducted with background dissolved gas concentrations closer to the hydrate saturation concentration, and these did form hydrate shells on the gas bubbles. Two main types of experiments were conducted in these cases: experiments at constant temperature and pressure to evaluate mass transfer (bubble shrinkage) rates and experiments with variable system pressure, simulating the rise of a bubble through the ocean water column. We evaluate the constant-pressure experiments here to assess the effects of hydrate shells on the mass transfer coefficient.

We define the hydrate formation temperature and pressure as  $T_{hyd}$  and  $P_{hyd}$ . When the HPWT system is operated at temperatures below the hydrate formation temperature or pressures above the hydrate formation pressure, there is the potential for hydrates to form. The driving, thermodynamic potential for hydrate formation is greater as the system is operated further away from the hydrate formation boundary. Hence, we characterize the experimental conditions by their sub-cooling  $\Delta T_{hyd}$  and excess pressure  $\Delta P_{hyd}$ , defined as:

$$\begin{aligned}\Delta T_{hyd} &= T_{hyd} - T \\ \Delta P_{hyd} &= P - P_{hyd}\end{aligned}\tag{10}$$

where  $T$  and  $P$  are the operational temperature and pressure in the HPWT at any time.

Figure 9 shows the mass loss rates predicted for dirty bubbles using empirical equations versus the bubble shrinkage rates observed in the HPWT in terms of mass loss rates. In evaluating the empirical mass loss rates ( $y$ -axis), we used mass transfer coefficients for dirty bubbles (immobile interfaces) to account for the hydrate shell.

To estimate empirical mass transfer rates, we also had to make a choice for the appropriate solubility  $C_s$  in the concentration term in Equation (6). There are two possible dissolution mechanisms for hydrate-coated bubbles. On the one hand, free gas may be the primary phase dissolving, leaking through cracks and fissures in the hydrate shell and dissolving directly from the free gas inside the bubble. In this case, the gas-water saturation concentration for gas should be used for  $C_s$ . On the other hand, the free gas could be trapped inside the hydrate shell so that bubbles

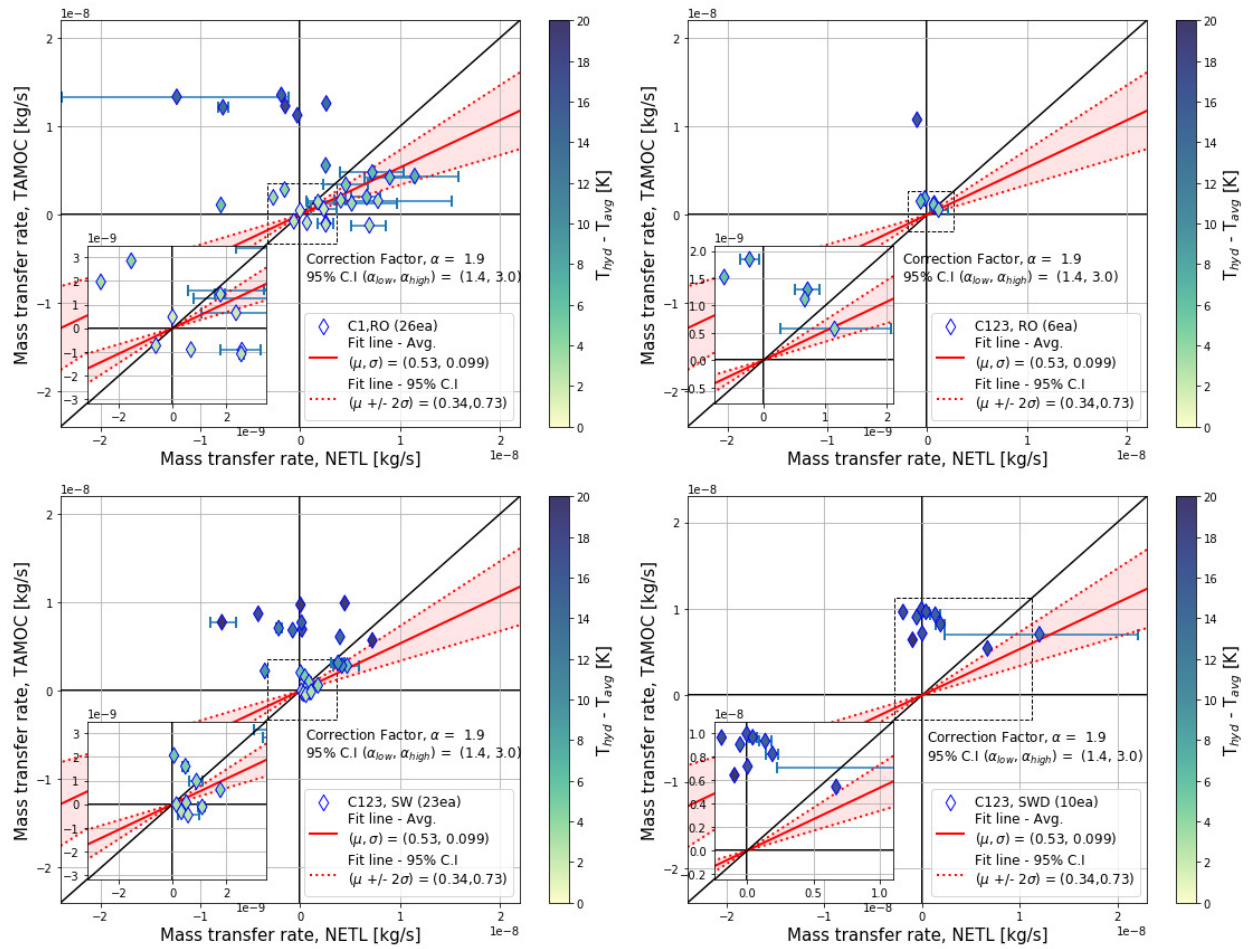


Figure 9: Mass transfer rates predicted by TAMOC for dirty bubbles versus the measured data from the NETL HPWT for hydrate cases. The upper-left frame is for methane in RO water, the upper-right frame is for natural gas in RO water, the lower-left frame is for natural gas in seawater, and the lower-right frame is for natural gas in seawater plus dispersant.

shrink by dissolution of hydrate at the hydrate-water interface and formation of new hydrate as gas molecules diffuse through the hydrate shell and encounter the water. In this case, the hydrate-water saturation concentration for gas hydrate should be used for  $C_s$ . In Figure 9, we use the gas-water saturation concentration, assuming that free gas is leaking through the hydrate shell and that dissolution of this gas into the water is the primary mechanism of bubble shrinkage.

From Figure 9, several observations can be made. First, the great majority of shrinkage rates with hydrate are much lower than those for the no-hydrate cases plotted in the previous section. This is because the HPWT must be operated with greater background gas concentration in order to form hydrate; hence,  $(C_s - C_a)$ , which is the driving chemical potential for dissolution, is lower in the hydrate cases than in the no-hydrate experiments. Second, like the no-hydrate experiments, there is a group of experiments near the solid red line that have good correlation and show mass transfer rates in the HPWT that are higher than rates predicted by the empirical equations. Third, like the no-hydrate experiments, experiments conducted very near saturation (zero or negative mass transfer rate) have larger uncertainty. This, again, stems from the small error in the predicted solubility becoming important as the difference  $(C_s - C_a)$  goes to zero. Since this becomes the subtraction of two large numbers, the error in the result becomes high. Fourth, unlike the no-hydrate experiments, there is a group of experiments at high sub-cooling for which the empirical mass transfer rates are much higher than those observed.

Considering these experiments at high sub-cooling, we also considered empirical mass transfer rates using the hydrate-water saturation concentration for  $C_s$  in Equation (6). These results (not shown) were more consistent with the observed mass transfer rates, but suffered from the fact that the experiments were conducted either at or more commonly slightly above the saturation concentration for hydrate in the HPWT. Hence, again, the concentration difference  $(C_s - C_a)$  approaches zero, and the model errors for predicting  $C_s$  become important. Because using  $C_s$  for the hydrate-water saturation moves these high sub-cooling points close to a predicted zero or negative mass transfer, which also agrees with the observations, we conclude that when the system pressure is maintained constant, dissolution is primarily from the hydrate phase at high sub-cooling.

One final observation to note is that all of the hydrate cases were conducted at constant system properties for shorter time periods than the no-hydrate experiments. This means that errors due to parallax did not fully even out. It also means that the bubble size change over the course of one experiment was less than in the no-hydrate case. Both of these effects increase the uncertainty of the hydrate-case data, witnessed by the larger error bars in Figure 9.

Our conclusions for the hydrate-case experiments based on observations at constant system temperature and pressure are the following. For hydrate sub-cooling  $\Delta T_{hyd} < 11^\circ\text{C}$ , results are

consistent with our observations for the no-hydrate case. Mass transfer rates observed in the HPWT are on average 1.9 times higher than that predicted by empirical models for dirty bubbles. Moreover, these mass transfer rates are predicted using the gas-water saturation concentration in the mass transfer estimate—indicating that it is predominantly free gas that is escaping from inside the bubble that is responsible for the bubble shrinkage. When the sub-cooling  $\Delta T_{hyd} > 11^\circ\text{C}$  and the system pressure remains constant, the hydrate shell appears to fully contain the free gas inside the bubble. In these cases, the mass transfer rate continues to agree with the dirty-bubble model, but with the hydrate-water saturation concentration being the driving chemical potential in the mass-transfer equation. Because these experiments at high  $\Delta T_{hyd}$  were conducted close to saturation conditions, it is not possible to validate the amplification factor  $\alpha$ ; however, it seems to be a consistent characteristic of the turbulence in the HPWT that a factor of  $\alpha = 1.9$  should be used until additional data with a more definitive value is available. Hence, for our seep model simulations comparing to the HPWT data, we will apply mass transfer rates of  $1.9\beta_{emp}$  with dirty bubble mass transfer coefficients in the model validation of Section 4.

### 3 Hydrate Formation Time

As discussed previously above, the NETL HPWT experiments were conducted by slowly filling a cup with gas under system conditions close to hydrate stability, then releasing the accumulated gas as a single bubble and rapidly changing the system pressure to match the desired experimental conditions. Because the injected gas accumulated in the cup over several minutes and because the pressure was high, close to the hydrate stability pressure, the gas release mechanism in the HPWT was quite different from that of gas released at the seafloor. We noted the hydrate formation times in the NETL experiments and reported these in Appendix B. Under these conditions, it was difficult to establish an initial time  $t = 0$  from which a hydrate formation time could be evaluated. If we used the moment a small amount of gas was first introduced into the inverted cup, then the hydrate formation time was fairly arbitrary as the time required to fill the cup varied considerably from experiment to experiment and was based on the user choices, such as injection rate and desired bubble volume. On the other hand, if we used the moment the gas bubble was released, the initial condition of the gas is that of a pool of gas that has equilibrated to conditions near the hydrate stability pressure in a stagnant cup, which is quite different from field conditions. Hydrate formation times based on this latter condition did not closely correlate with system state variables, such as  $\Delta T_{hyd}$ ,  $T$ ,  $\Delta P_{hyd}$ , or  $P$ . In the end, we were forced to conclude that the hydrate formation times in the HPWT experiments could not be predicted from experimental conditions.

Table 3: Parameters for each bubble release case and the statistical analysis of the performance of the developed model.

Case	$z_{reported}$ [m]	$d_{reported}$ [mm]	$t_i$ [s]	$u_s$ [m/s]	$z_{adjusted}$ [m]	$\mu_e$ [mm]	$\sigma_e$ [mm]	bias [%]
590	587.7	6.4	38	0.239	596.8	0.014	0.160	0.437
593	593.8	7.4	53	0.235	606.3	-0.006	0.402	1.982
704	683.3	9.2	57	0.228	696.3	-0.024	0.392	0.282
802	799.0	6.2	5	0.238	800.2	-0.015	0.219	0.141
825	824.6	5.0	117	0.246	853.4	-0.013	0.140	-0.240
1098	-	-	-	-	-	0.009	0.227	0.686
1209	1207.5	7.0	70	0.231	1223.7	0.005	0.227	0.329
1495	1492.5	6.2	160	0.233	1529.7	0.011	0.261	0.566
1511	1509.7	5.8	190	0.235	1552.3	0.012	0.201	0.500

To derive a model for hydrate formation time nonetheless, we resorted to data published in the literature and from our own observations for free gas bubbles in the ocean water column. This work was previously published in the doctoral dissertation Jun (2018). Like our analysis above, we use separate calibration and validation data. For model calibration, we used data for methane gas bubbles released artificially in Monterey Bay Canyon and tracked by ROV as reported in Rehder et al. (2009). Table 3 summarizes the initial conditions for each of the experiments within the hydrate stability zone reported in Rehder et al. (2009). To validate the model, we use literature data from the HPWT reported in Warzinski, Lynn, Haljasmaa, Leifer, Shaffer, Anderson and Levine (2014) and from the GISR field experiments, reported in Wang et al. (2016).

The model development proceeded in two phases. First, we analyzed the Rehder et al. (2009) dataset to determine the initial bubbles sizes the hydrate formation time. Second, we developed an empirical model to predict the hydrate formation time that depends on the initial bubble sizes and the hydrate sub-cooling,  $\Delta T_{hyd}$ . Bubbles were released in the Rehder et al. (2009) field experiments similarly to the HPWT, but with potentially shorter accumulation times and without changing the system pressure at the moment of bubble release. Rehder et al. (2009) report measurements some few minutes after release. Hence, we must extrapolate the bubble shrinkage rates backward to time  $t = 0$  to estimate the initial bubble sizes. The reported bubble size data typically show two different shrinkage rates: an initially faster rate followed by a slower rate. Here, we assume that the hydrate formation time agrees with the time at which the mass transfer coefficients switch from clean-bubble mass transfer to dirty-bubble mass transfer. We call this the mass transfer transition time.

To determine the initial bubble size and mass transfer transition time, we used the following methods. In the Rehder et al. (2009) experiments, the bubbles were kept near the ROV by releasing

them within a plexiglass sleeve. This avoided the extra turbulence of the inverted cone used in the HPWT experiments; hence, for these experiments, we assume the amplification factor  $\alpha$  is 1.0. Because the experiments utilized one camera and the bubble could move laterally within the plexiglas sleeve, the bubble size data show significant scatter, similar to the HPWT data described above. Thus, some form of curve fitting is necessary to determine the actual shrinkage rates.

We chose to fit the Rehder et al. (2009) data by applying our seep model (described in detail in Section 4) rather than fitting straight lines. This was necessary as the pressure reduces as the bubble rise, a process that was avoided in the HPWT experiment described above. We initialize the model with an assumed initial bubble size  $d_{e,i}$  and using the ambient temperature and pressure reported by Rehder et al. (2009). We then compute the bubble size as a function of time, initially using clean bubble mass transfer coefficients and switching to dirty bubble mass transfer coefficients after a given mass transfer transition time  $t_{trans}$ . We fit the initial bubble size and mass transfer transition time using a parameter estimation method called the Markov Chain Monte Carlo (MCMC) method, which is a type of Bayesian calibration. From the iterative process of calibration, the MCMC algorithm randomly generates both the initial bubble size and the transition time parameters and optimizes the parameter set through non-linear regression. Using on the MCMC method, we randomly generate 1000 appropriate pairs of initial bubble size and the transition time for each experiment in the Rehder et al. (2009) dataset. The model performance compared to the measured data using each combination of initial bubble size and transition time from the MCMC method is shown in Figure 10. Each dot represents a measured bubble diameter from Rehder et al. (2009). The grey area shows the range of random sample sets, and yellow lines show TAMOC simulation results for the selected samples from the MCMC method. The slope of the curve is set by the rise velocity and mass transfer rate predicted by the seep model; hence, it is not part of the calibration. Only the initial point the time where the solution slope changes from clean bubble mass transfer to dirty bubble mass transfer  $t_{trans}$  are included in the calibration. The optimal model results for each case are also shown in the textbox for each subplot.

To develop a predictive equation for  $t_{trans}$ , we apply a kinetics-based model. We assume that the rate of hydrate growth (area per time) is proportional to the sub-cooling  $\Delta T_{hyd}$  at the release depth and that the total area to be covered by hydrate is the initial surface area of the bubble (Wang et al., 2020). Then, we can derive that the transition time should follow the model

$$t_{trans} = \frac{\pi d_{e,i}^2}{\gamma \Delta T_{hyd}^\beta} \quad (11)$$

where  $\gamma$  and  $\beta$  are empirical coefficients. Using the data for  $d_{e,i}$  and  $t_{trans}$  obtained from the MCMC algorithm and our seep model, we find the best-fit parameter values  $\gamma = 0.255 \text{ m}^2/(\text{sK}^{1/3})$

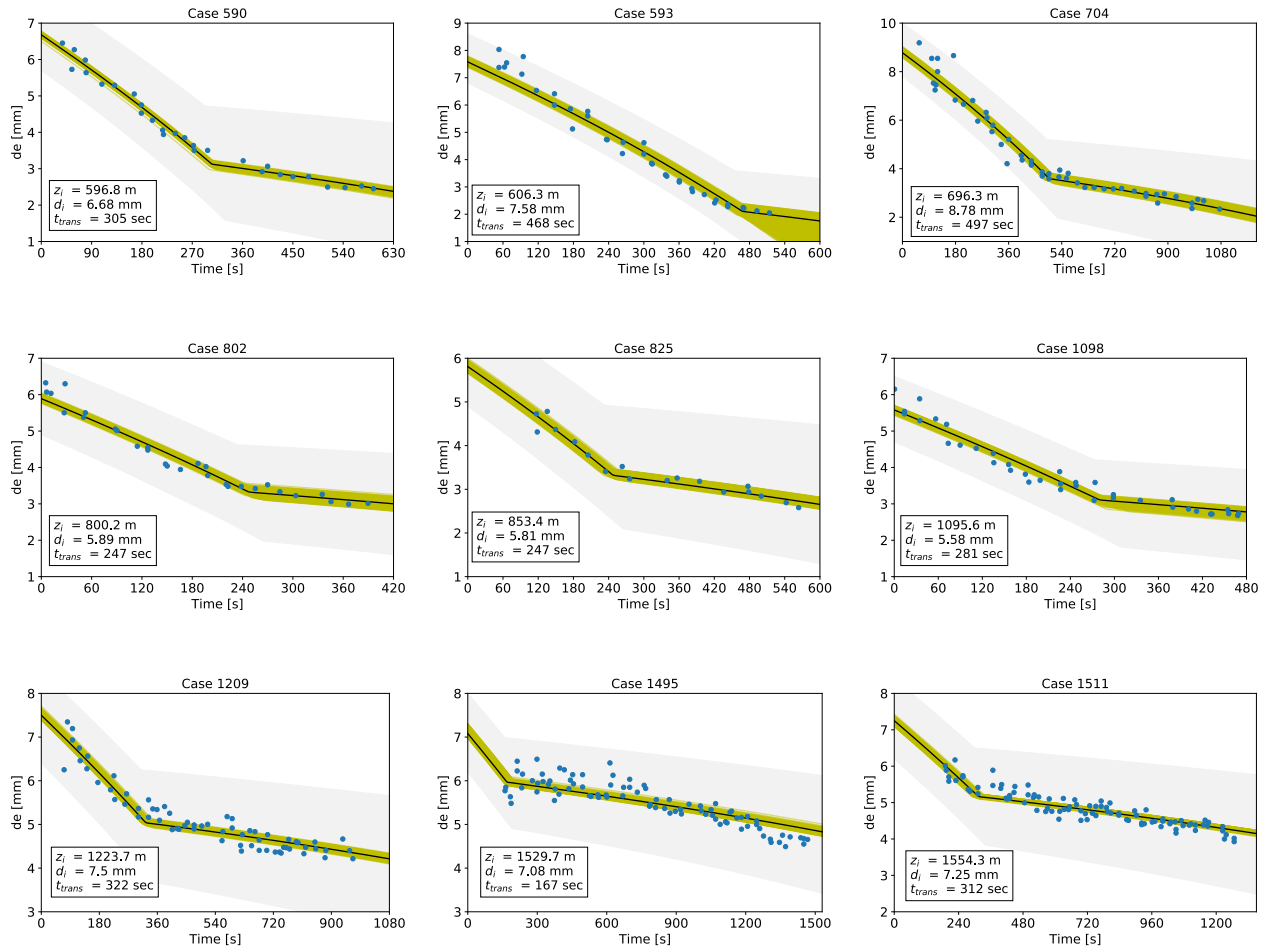


Figure 10: Simulation results using the MCMC algorithm (shaded region) and best fit model (solid line) with the observed data (dot) from Rehder et al. (2009).

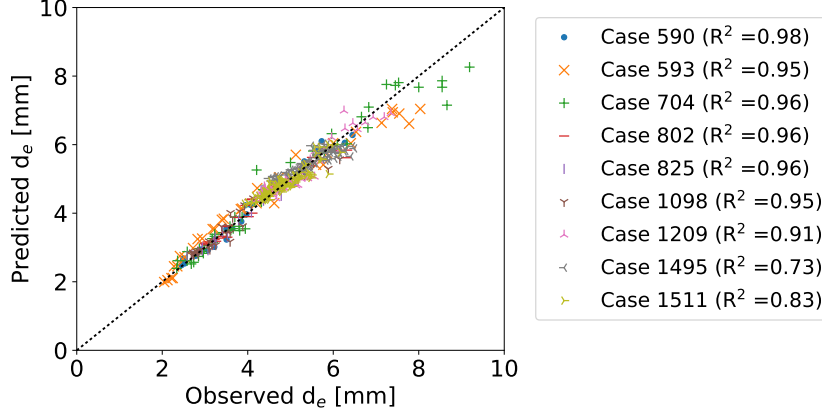


Figure 11: The comparison between model prediction with the measurement of bubble size for each case.

and  $\beta = 1/3$ .

We evaluate the fit statistics of Equation (11) using the Rehder et al. (2009) data. To do this, we run our seep model again, using the transition time predicted by Equation(11) instead of the optimal transition time obtained from the MCMC algorithm; we initialize the model, though, with the optimal guess for  $d_{e,i}$ . Figure 11 shows the results for each of the model runs in Figure 10, plotting as predictions versus observations. The  $45^\circ$  line gives the perfect correlation. The comparison shows that  $R^2 > 0.9$  for most of the cases, with Case 1495 having  $R^2 = 0.73$  and Case 1511 having  $R^2 = 0.83$ . These two cases have the deepest release depths, and comparing to Figure 10 these cases have the greatest scatter in the experimental observations. Indeed, much of the difference between the model and the measurements arises from the inherent measurement error due to parallax as the bubble wanders throughout the retaining, plexiglas sleeve.

As another naïve metric of the model error, we compute the mean ( $\mu_e$ ), standard deviation ( $\sigma_e$ ), and bias of errors between the model prediction and observed data; these are also reported in Table 3. The averaged errors between the modeled and measured diameters are 0.002 mm, with a standard deviation of 0.3 mm. The averaged bias for predicting bubble diameter is 0.5 %. The mean and standard deviation of these errors are similar to the scatter in the measurements observed in Figure 10. Likewise, the model bias is negligible over the whole dataset. The model does show a weak tendency to underestimate the bubble diameter for shallow cases ( $500 \text{ m} < z < 1,000 \text{ m}$ ) and overestimate for deep cases ( $z > 1,000 \text{ m}$ ). However, within the scatter of the observations, there is no basis to reject the model simulations.

While the previous fit statistics measure the performance for predicting the bubble diameters using the seep model, we also directly compare the transition time predicted by Equation (11) with

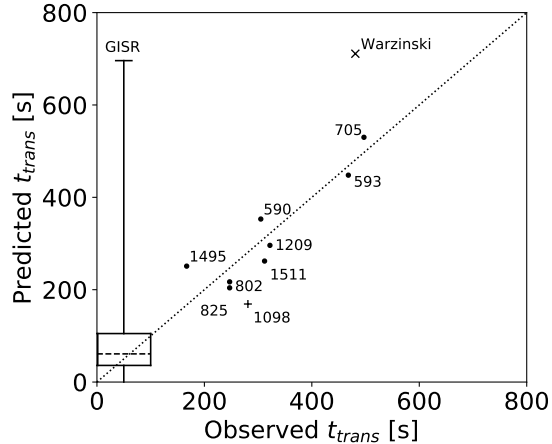


Figure 12: Comparison the predicted transition time ( $t_{trans}$ ) with the observed experimental data.

the optimal values determined from the MCMC algorithm. These results are shown as the dots in Figure 12. Each datapoint in the figure is labeled by the corresponding release depth from Table 3. In this validation plot, we also include data not used in the model calibration. These include the experiment reported in Warzinski, Lynn, Haljasmaa, Leifer, Shaffer, Anderson and Levine (2014) for the HPWT and the observations at one seep for the GISR experiments. As discussed previously, the HPWT transition times are somewhat uncertain due to the bubble injection method; however, this experiment reported by Warzinski, Lynn, Haljasmaa, Leifer, Shaffer, Anderson and Levine (2014) is in reasonable agreement with the present model for transition time. For the GISR data, bubbles with a modest size spectrum are released from a small seep feature on the seafloor. Hydrate formation was observed in highspeed camera images, and is taken as the height for which bubble-water interfaces appear frozen (interfacial waves have ceased). Observations were made at 0.5 m, 2 m, and 20 m above the release. While many bubbles formed hydrates with 2 m of rise, some bubbles were not fully hydrated; all bubbles at 20 m height had formed hydrate. Based on the bubble rise times, we estimated that all bubbles had formed hydrates between 2.5 s and 100 s. In the figure, the transition time is calculated as 60 s for the population-median bubble size ( $d_{50}$ ), 35 s for the lower quartile bubble size ( $d_{25}$ ), and 105 s for the upper quartile bubble size ( $d_{75}$ ), which is shown as a box-and-whiskers plot in Figure 12.

For all of the data in Figure 12, we computed basic fit statistics of the 45° perfect correlation line, which has an  $R^2$  value of 0.8. From these data, there appears to be good correlation between the observed transition times and those predicted by Equation (11). We use this hydrate formation time to validate the developed seep model to field data. In the HPWT, we always use the observed transition times to ensure the model selects the appropriate mass transfer models.

## 4 Refinement and Validation of Natural Seep Numerical Model

From the HPWT data and selected field observations presented in the previous two sections, we determined the appropriate mass transfer coefficients and mass transfer model for bubbles released under deep ocean conditions. In this section, we implement these models in a comprehensive model for predicting gas dynamics of natural seep bubbles. The seep model developed here is adapted from the single bubble model, which is an element of the TAMOC modeling suite. TAMOC is a comprehensive modeling system for predicting the dynamics of oil and gas bubbles in the ocean for either tracking individual bubbles (single bubble model) or following swarms of bubbles in subsea oil and gas blowouts (bent plume and stratified plume models). The numerics of this modeling suite have been presented in Dissanayake et al. (2018), which also includes a comprehensive validation of the plume model modules. The equations of state were validated in Gros et al. (2016) for oil samples from the *Deepwater Horizon* oil well blowout, and the bent plume model module was further validated to field data from *Deepwater Horizon* in Gros et al. (2017). Here, we present a brief overview of the elements of TAMOC important for the single bubble model and then adapt and use this model to predict the HPWT data and to compare to observations from the GISR cruises. Together, this model refinement and validation results in a reliable model for predicting the gas dynamics of subsea natural seeps.

### 4.1 Numerical modeling methods

TAMOC is coded in Python and Fortran and is freely available at <http://github.com/socolofs/tamoc>. TAMOC contains modules for predicting fluid particle properties (Discrete Particle Model, DPM) and for tracking an individual fluid particle (Lagrangian Particle Model, LPM). Here, the term fluid particle refers to both liquid droplets and gas bubbles. Other modules within TAMOC provide integral models for simulating strong blowout plumes, both in stratification and crossflow. Since we are interested in natural seeps at weak gas flow rate with limited entrained water and ambient crossflows, the coupled DPM and LPM were used for the work in this study. See Wang et al. (2019) for a detailed justification for why we consider natural seep bubbles to behave as individual bubbles rather than as plumes with entrainment and significant upwelling velocity of the entrained seawater.

### 4.2 Discrete particle model

TAMOC calculates the thermodynamic, chemical, and hydrodynamic properties of the individual fluid particle in seawater and applies their predicted dynamics to the particles along their path. This

method is known as the Discrete Particle Model (DPM) approach in multiphase plume literature. Wüest et al. (1992) first introduced the DPM for modeling aeration plumes in lakes and reservoirs, and the method was further developed for lakes by Bryant et al. (2011), Little and McGinnis (2001), McGinnis et al. (2004), and Singleton and Little (2006). McGinnis et al. (2006) adapted the DPM to non-ideal gases for predicting methane dissolution from seeps in the Black Sea; TAMOC uses a similar approach to non-ideal gas behavior. The main differences between TAMOC and the model in McGinnis et al. (2006) are in the way hydrates are treated. There are also some minor differences in choices for the thermodynamic equations-of-state and a few other particle properties, but although different methods are used, similar results are attained for these elements of both models. A brief overview of the solution used in TAMOC follows.

#### 4.2.1 Fluid particle types: shape and circulation

Hydrodynamic properties of fluid particles, including rise velocity and mass transfer rates, depend on their shape and boundary conditions at the water-particle interfaces (Clift et al., 1978). The shape of fluid particles can be grouped into different regimes, based on the value of dimensionless numbers. Fluid particle shapes vary from spherical to ellipsoidal to spherical-cap, depending on the particle size and the properties of the particle and ambient water. Clift et al. (1978) correlate particle shape with several dimensionless numbers which can describe fluid particle characteristics, including the Eötvös number ( $EO$ ), the Morton number ( $M$ ), and the Reynolds number ( $Re$ ). There is some ambiguity regarding the boundaries of the ellipsoidal shape regime. We use the parameter  $H$  defined in Clift et al. (1978) to help define the boundaries. The boundary between spherical and ellipsoidal particles is taken as  $H = 2$ ; spherical-cap particles are assumed when  $EO > 40$  or  $M > 0.001$  or  $H > 1,000$ . Ellipsoidal-shaped particles are assumed between these two boundaries.

The mobility at the water-particle interface determines the circulation inside a bubble or droplet. When the interface is flowing, internal circulation occurs, and rising velocity and mass transfer rates are maximized. On the other hand, if the interface is immobilized, there is no internal circulation. In this case, the no-slip boundary condition on the immobile interface gives a larger drag and a lower rising velocity. The lack of internal circulation also stops the internal convection, leading to slower mass transfer rates. The immobile interface can occur for solid particles, fluid particles with solid shells, and fluid particles in contaminated systems. For contaminated particles, naturally occurring surfactants populate the water-particle interface and the gradients of the concentration of these surfactants on the interface produce Marangoni forces, which arrest the interfacial motion. Because surfactants are ubiquitous in nature, bubbles or droplets in the environment become contaminated quickly after they are released. Moreover, since the primary mechanism for fluid particles to behave

as rigid is by surfactant contamination, we refer to particles with moving interfaces as clean bubbles or droplets and particles with immobile interfaces as dirty bubbles or droplets.

Both clean and dirty fluid particles have different correlation equations for rising velocity and mass transfer rates. Differences between these rates are largest for ellipsoidal particles, which are in the size range of about 3 mm to 8 mm diameter for natural gas bubbles in the oceans across a wide range of depths. This is a typical bubble size observed at natural seeps; hence, both clean and dirty fluid particle behavior may be observed for bubbles from natural seeps.

#### 4.2.2 Equation of state for mixtures

The fundamental thermodynamic properties needed to simulate the fate of hydrocarbon fluid particles include density, fugacity, solubility, diffusivity, viscosity, and surface tension. TAMOC uses the Peng-Robinson equation of state (PR-EOS) with volume translation to predict the fluid density and fugacity (McCain, 1990; Michelsen and Mollerup, 1986). The PR-EOS with volume translation accounts for the non-ideal behavior of the compressible gas and liquid hydrocarbons in complex mixtures at high-pressure and low-temperature (Peng and Robinson, 1976; Robinson and Peng, 1978; Gros et al., 2016). The solubility is computed from the modified Henry’s law, with the correction for temperature and pressure following King (1969) and the correction for salinity using a Setschenow salting out coefficient (Schwarzenbach et al., 2003).

Molecular diffusivity, dynamic viscosity, and surface tension are computed from correlations in the literature (Danesh, 1998; Hayduk and Laudie, 1974; Pedersen et al., 2015). Some of these correlations depend on the properties of seawater, which we obtain from the seawater equation of state in Gill (1982) and from correlations summarized in Sharqawy et al. (2010). Hydrocarbon mixtures are represented in the DPM module by their explicit composition on a component mass basis. The properties of the pure compounds needed by these equations of state and correlations (e.g., critical point properties, acentric factors, Henry’s law constants, Setschenow constants, the heat of solution, and molar volume at infinite dilution) are distributed in a database within TAMOC. For the mixtures of light gases, these thermodynamic constants were obtained directly from data in the literature (McCain, 1990; Poling et al., 2001).

#### 4.2.3 Slip velocity

The DPM calculates the terminal rise velocity, or slip velocity  $u_s$ , of bubbles or droplets using the correlation equations in Clift et al. (1978). For dirty particles, we follow the criteria in Section 4.2.1 to define the particle shape and then apply the correlations for the corresponding shape regime.

The clean particle slip velocity  $u_s|_{clean}$  is evaluated from the dirty particle velocity  $u_s|_{dirty}$  following the expression from Clift et al. (1978) given by

$$u_s|_{clean} = u_s|_{dirty} \left( 1 + \frac{\Gamma}{1 + \kappa} \right). \quad (12)$$

The analytical equation for  $\Gamma$  is only provided as a figure in the reference, and we fit  $\Gamma$  from their figure as

$$\Gamma = 2 \exp \left[ \frac{-(\log_{10} \chi + 0.6383)^2}{(0.2598 + 0.2(\log_{10} \chi + 1.0))^2} \right] \quad (13)$$

where  $\chi = Eo(1 + 0.15\kappa)/(1 + \kappa)$ . Together, these equations are applicable to oil droplets, gas bubbles, and hydrate particles.

#### 4.2.4 Mass Transfer

The mass transfer coefficient is an empirical parameter that gives the bulk gas transfer velocity averaged over the surface of a fluid particle, and this coefficient depends on both the boundary layer and wake hydrodynamics around the bubble and diffusion coefficient in the continuous phase Clift et al. (1978). The dissolution process is occurring at the water-particle interface, inside of a non-uniform concentration boundary layer surrounding the particle. Turbulent motion in the continuous phase transports dissolved material away from the particle. Integrated over the particle surface, the total mass transfer rate (dissolution) from a particle to dissolved form can be described by the empirical Ranz-Marshall equation:

$$\frac{dm_i}{dt} = -A\beta_i (C_{s,i} - C_{a,i}) \quad (14)$$

(see also Equation (1), above). The mass transfer coefficient  $\beta_i$  groups the physical process of turbulent transport around the bubble together with the thermodynamic process of molecular diffusion at the water-particle interface. Since we express  $dm_i/dt$  in terms of  $C_{s,i}$  and  $C_{a,i}$  we are explicitly assuming that there is adequate methane transport inside the particle to maintain the concentration  $C_{s,i}$  at the interface; hence, we assume the mass transfer is limited on the seawater side of the particle. This is a valid assumption for gas bubbles that have efficient mixing within their boundaries.

Similar to the slip velocity, TAMOC combines correlation equations for mass transfer from Clift et al. (1978) and Johnson et al. (1969) for dirty and clean particles, respectively. Equations for dirty particles follow Clift et al. (1978), with spherical and ellipsoidal particles modeled by correlations for solid spheres and spherical-cap particles by a separate correlation. Johnson et al. (1969) gave a correlation for clean particles valid over the full shape regime from spherical to spherical-cap. For

some cases, the Johnson et al. (1969) correlation predicts slower mass transfer than those using the dirty-particle equations in Clift et al. (1978); in those cases, TAMOC uses the higher prediction as the mass transfer coefficient, so that mass transfer rates for clean particles could never be lower than those for dirty particles.

### 4.3 Lagrangian particle model

Using the particle properties from the DPM, the Lagrangian Particle Model (LPM) tracks the evolution of individual bubbles or droplets rising through the water column. The LPM simulates the rising bubble or droplet by the advection equation for a single particle coupled with the mass transfer equation for each chemical component in a particle, Equation (14), and the heat transfer equation for the whole particle, similar to Equation (14), but using a heat transfer coefficient and replacing concentration with absolute temperature). These equations yield a coupled set of non-linear Ordinary Differential Equations (ODE), which are solved with a variable step size numerical solver designed for stiff ODEs (the `vode` solver of the `integrate.ode` module of Scipy using the backward difference formula).

#### 4.3.1 Trajectory of bubbles

The mean trajectory of a stream of particles is assumed to be the superposition of the vertical slip velocity of a bubble  $u_s$  computed for a stagnant ambient and the three-dimensional, ambient current velocity  $\vec{u}_a$ . This advection equation ignores the random walk due to turbulence and is expressed as

$$\frac{d\vec{x}}{dt} = \vec{u}_a + u_s \vec{k} \tag{15}$$

Equation (15) predicts well the centerline trajectory of bubbles rising from a natural seep during steady current conditions. In the oceans, this type of particle dynamics may occur for very weak plumes rising from a natural seep or for small oil droplets rising out of the intrusion layer formed in an accidental oil well blowout.

#### 4.3.2 Dissolution of bubbles

Mass transfer depends on the mass transfer coefficient, surface area, and the driving potential, as shown in Equation (14). The total mass transfer from the bubble or droplet is simulated through Equation (14) expressed for each component in the mixture. The mass transfer equations are coupled to the advection equation through the slip velocity, which depends on particle properties,

the mixture composition, and ambient conditions. Hence, together the DPM and LPM can simulate the evolving composition and trajectory of natural gas bubbles released in the deep ocean.

### 4.3.3 Adaptation based on the HPWT experiment conditions

Using the results from Section 2, the single bubble model of TAMOC was updated in two main ways. First, the standard model solves for the changing water depth of the bubble and extracts the ambient water properties from a database of water properties versus depth (e.g., a vertical profile of ocean water properties). In the HPWT experiments, the bubble remains suspended at a point, and the ambient temperature and pressure are selected by the operator. We updated TAMOC so that ambient data are stored as a function of time, rather than water depth, and we use the model simulation time to look up the relevant water properties. Water depth is effectively eliminated from the model solution; hence, Equation (15) is not solved when simulating a bubble in the HPWT—only Equation (14) and the corresponding heat transfer equation must be considered.

Second, we utilize the observed mass transfer rates from Section 2 in the TAMOC simulations to validate the TAMOC model to the HPWT experiments. This is done through the mass transfer amplification factor  $\alpha$ , which varies over a modest range. We run the TAMOC model with the mean measured value of  $\alpha = 1.9$  and the  $\alpha$ -values corresponding to the 95% confidence intervals in order to see the spread in model predictions. When comparing the model to field observations, we set  $\alpha = 1$ , as  $\alpha$  accounts for the elevated turbulence in the pipe flow of the water tunnel that is absent in the deep ocean.

## 4.4 Validation of seep model to HPWT data

The submodules for all of the elements of TAMOC that go into its equations of state and fluid properties (e.g., density, solubility, slip velocity, etc.) have all been validated using data from the original sources for those algorithms. Here, we validate the model solution for the total bubble mass as a function of time  $m(t)$ , expressed using the density as an equivalent spherical radius (ESR)  $r(t) = [3m/(4\pi\rho)]^{1/3}$ , where both  $m$  and  $\rho$  vary with time in the TAMOC simulations.

### 4.4.1 Examples for no-hydrate cases

We simulate each bubble in the HPWT starting from its release into the water tunnel and using the reported time series for system properties in the HPWT (e.g., pressure, temperature, and recirculation flow rate). Figure 13 shows an example time series of system properties for the 1st bubble recorded on June 15, 2012. The dashed line in the figure shows the triple-point equilibrium

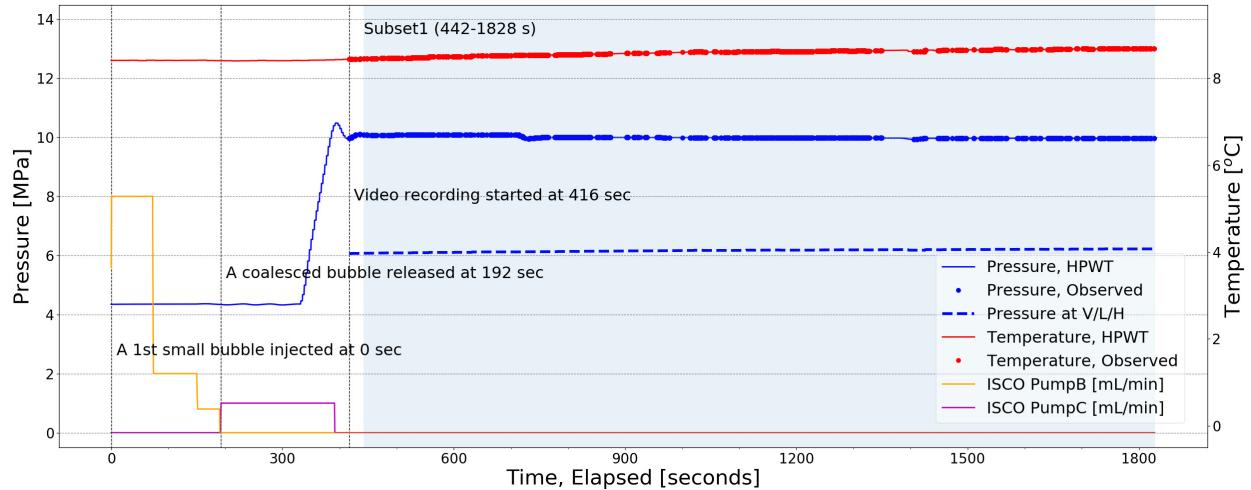


Figure 13: System information of NETL HPWT facility during the experiment for a CH<sub>4</sub> bubble in RO water, June 15, 2012 1<sup>st</sup> bubble. The ISCO PumpB injets gas into the collection cup; ISCO PumpC is used to flush the line as the cup is inverted and the bubble is released.

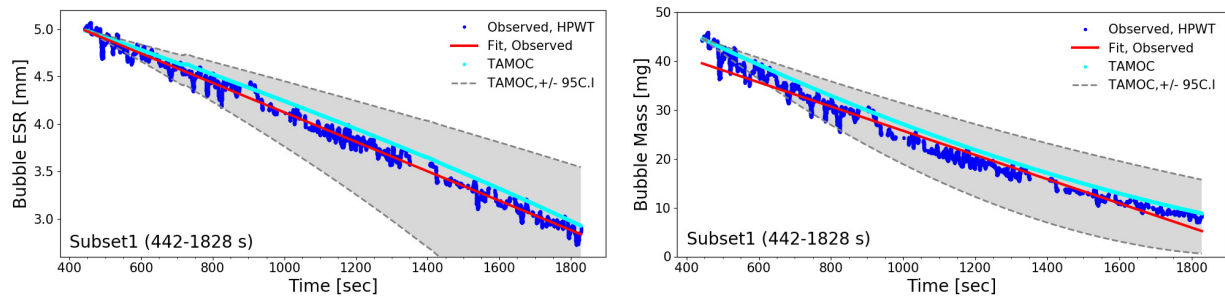


Figure 14: TAMOC simulation for a CH<sub>4</sub> bubble in RO water, June 15<sup>th</sup> 2012 1<sup>st</sup> bubble. System conditions are those in Figure 13. The left subplot shows results as ESR versus time; the right subplot shows results as bubble mass versus time.

line of the vapor-liquid-hydrate (VLH) system. In this experiment, the bubble was injected into the inverted cup (ISCO PumpB) while the system pressure was below the VLH line (up to 200 s). Shortly after 300 s, the system pressure was increased to 10 MPa (4 MPa above the VLH line) as the gas collection cup was inverted, releasing the bubble, and the gas line was flushed (ISCO PumpC). As the experiment progressed, the pressure was maintained constant at 10 MPa, and the temperature gradually increased due to heat transfer from the pump and from the ambient air in the laboratory.

Figure 14 shows a comparison of the TAMOC simulation results with the observed bubble size data and the best-fit line to the observations. The initial bubble size in TAMOC is taken as the initial value on the best-fit line fit to the experimental observations. The figure shows results both for the ESR  $r(t)$  (left plot) and for the bubble mass  $m(t)$  (right plot). The cyan lines in the figure

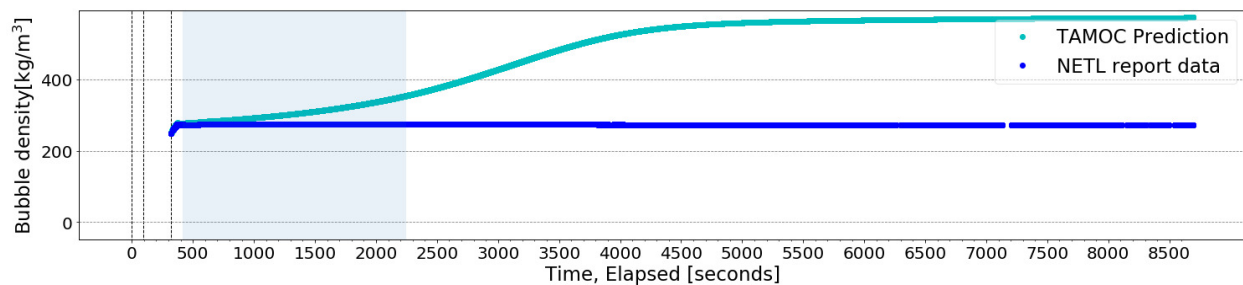


Figure 15: Bubble density during the experiment for C1C2C3 in Seawater on February 28, 2013, 1st bubble; pressure was constant during the experiment. The NETL reported value is a computed density using the initial composition of the bubble.

give the TAMOC result using a mass transfer amplification factor  $\alpha = 1.9$ ; the grayed region shows the TAMOC results using  $\alpha$ -values spanning the 95% confidence interval for  $\alpha$ . Both subplots show that the best-fit value of  $\alpha$  together with the TAMOC model simulation (the cyan line) gives excellent agreement between the model and the observations.

The validation conducted in Figure 14 is a particularly challenging validation for the model. Each time-step the model computes a small mass loss due to dissolution and updates the bubble total mass. Tiny errors at each calculation step, thus, add together as simulation time progresses. Hence, small errors in the TAMOC solution to Equation (14) each time step could add up to significant errors by the end of the experiment. This is somewhat evident by the simulation extremes given by the dashed lines, following  $\alpha$ -values corresponding to the 95% confidence interval. Because the TAMOC simulations using the best-fit  $\alpha$  match these data so well, this gives high confidence that the model performs well when using the correct parameterizations.

When simulating natural gas bubbles (C1C2C3), the bubble composition changes as the experiment progresses. Methane is the more soluble of these gases and the more abundant in the gas mixture used, hence, it is the primary gas dissolving early in the experiment. Eventually, most of the methane is dissolved away, and ethane begins to dissolve, followed finally by propane. Because the density of methane, ethane, and propane are different, the density of the gas bubble also changes with the composition. Figure 15 shows the density of a C1C2C3 bubble released in seawater on February 28, 2013 (1st bubble) as a function of experimental time. The cyan line shows the density computed by TAMOC; the blue line shows the density of a bubble having a fixed composition matching the initial gas composition. Pressure and temperature were effectively constant during this experiment. Because gas bubble rise velocity depends on the bubble buoyancy, which is a function of the bubble size and density, this variation of the bubble density is important for predicting the rise velocity and, hence, the fate of a natural gas bubble released into the environment.

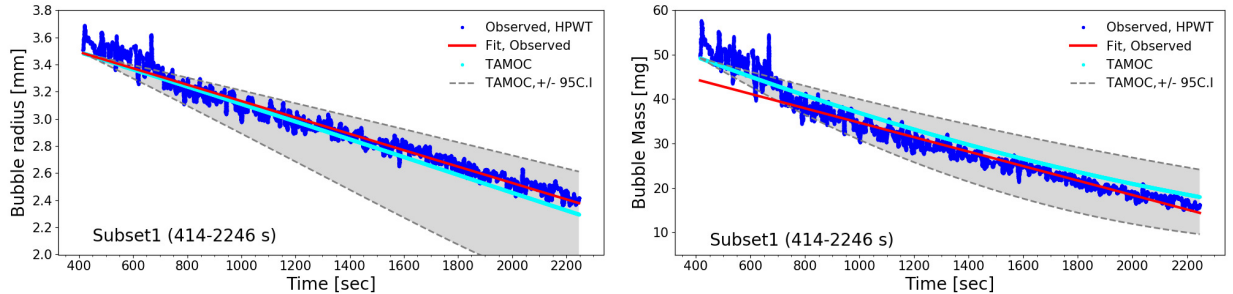


Figure 16: TAMOC simulation in for a C1C2C3 in Seawater on February 28, 2013, 1st bubble; same experimental conditions as Figure 15.

Figure 16 shows the TAMOC simulation for this same C1C2C3 bubble on February 28, 2013. The TAMOC initial condition, taken from the red, best-fit line to the observations of ESR, slightly under-predicts the initial bubble size. Nonetheless, the simulation results track the observed data quite well. The computed data for bubble mass (blue line in the right-hand subplot of Figure 16) are based on the density assuming constant composition, which is shown to under-predict the density in Figure 15 as methane dissolves out of the natural gas bubble. Hence, the NETL results shown for  $m(t)$  in Figure 16 would be expected to lie below the simulation results as they assume a lower than actual density. Because the observed ESR is the fundamental quantity measured in the laboratory and is unaffected by errors in the assumed density, we use the ESR rather than computed data for  $m(t)$  to quantify the model performance here.

#### 4.4.2 Examples for cases with hydrate formation

As explained in Section 2, of the experiments conducted at pressures within the hydrate stability zone, some bubbles formed a hydrate shell and others did not. The examples in the previous section were for bubbles without a hydrate shell and at constant system pressure. In those cases, the TAMOC single bubble model using the best-fit mass transfer amplification factor  $\alpha = 1.9$  matched the observed bubble sizes  $r(t)$  quite well. In this section, we consider experiments with a hydrate shell. Because these experiments were conducted with elevated ambient dissolved gases and for shorter observation periods, we could not estimate a separate  $\alpha$ -value for the hydrate cases in Section 2, though we could postulate that free gas continues to be the main dissolving phase up to a hydrate sub-cooling of  $11^\circ\text{C}$ , above which hydrate appears to become the dominant dissolving phase in constant-pressure experiments. Here, we run the TAMOC simulations using the same  $\alpha = 1.9$  and adjusting  $C_s$  depending on the system sub-cooling to validate the TAMOC simulations and the dissolution model in the hydrate cases.

Figure 17 shows the system information for a hydrate experiment of a natural gas bubble on

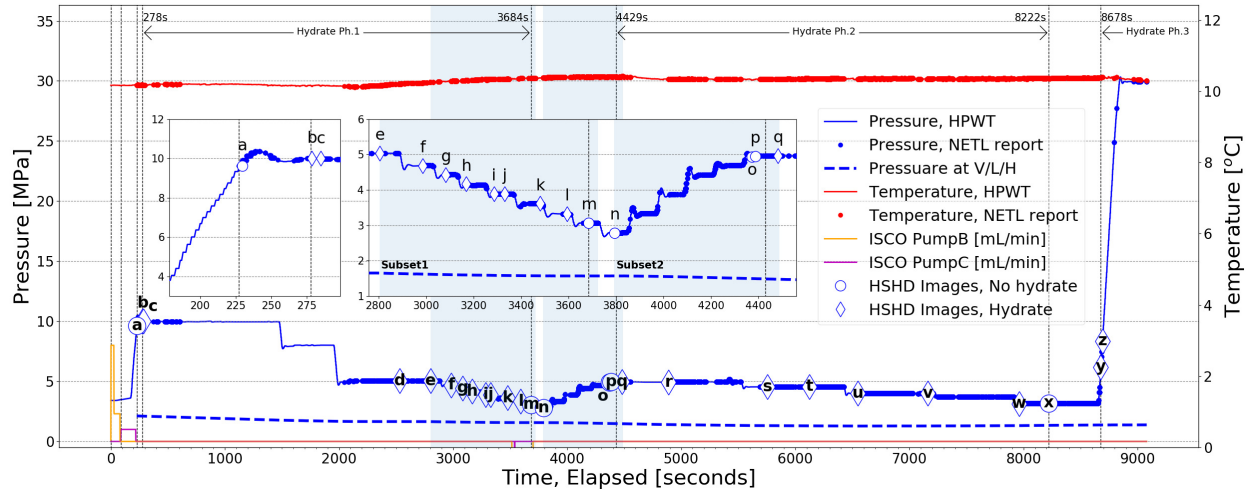


Figure 17: System information of NETL HPWT facility during an experiment for a C1C2C3 bubble in Seawater water on June 21, 2013, 1st bubble.

June 21, 2013. The main horizontal axis shows the entire experimental time; two inset plots expand the system pressure information for selected time periods. We identify several key events during the experiment, denoted by the letters ‘a’ through ‘q’ in the figure. Camera video frames corresponding to these experimental times are shown in Figure 18. The bubble appears clear of a hydrate shell (time ‘a’) as the experiment initially reaches 10 MPa (4 MPa above hydrate formation pressure). About 50 s later, hydrate begins to coat the bubble (time ‘b’), and hydrate formation rapidly covers the whole bubble (time ‘c’). The system pressure is then slowly released, and the hydrate shell remains on the bubble until after the system pressure drops below the hydrate stability pressure (points ‘d’ through ‘e’). As hydrate dissociates, small plates of hydrate remain floating on the bubble water interface (times ‘f’ through ‘j’). Eventually, the bubble is again free of hydrate (time ‘k’). The system pressure is then sequentially increased, this time with hydrate forming more quickly once a stable hydrate-forming pressure is reached (points ‘p’ and ‘q’).

Figure 19 shows the TAMOC simulation for two time-periods during the experiment in Figures 17 and 18. In both subplots, we assume a dirty-bubble mass transfer coefficient in TAMOC with a mass transfer amplification factor of  $\alpha = 1.9$ ; we also show results for  $\alpha$  values within their 95% confidence intervals. In the upper subplot, the system pressure is reducing; hence, the bubble expands each time the pressure is reduced. In the lower subplot, the situation is reversed as the system pressure is increased. From the TAMOC simulation line using the best-fit  $\alpha$  (cyan), it is clear that the bubble is not predicted to shrink much during the intervals that the pressure remains constant, but that the bubble size responds with a greater signal when the pressure is changed. The TAMOC equations of state appear to predict these size changes resulting the density changes

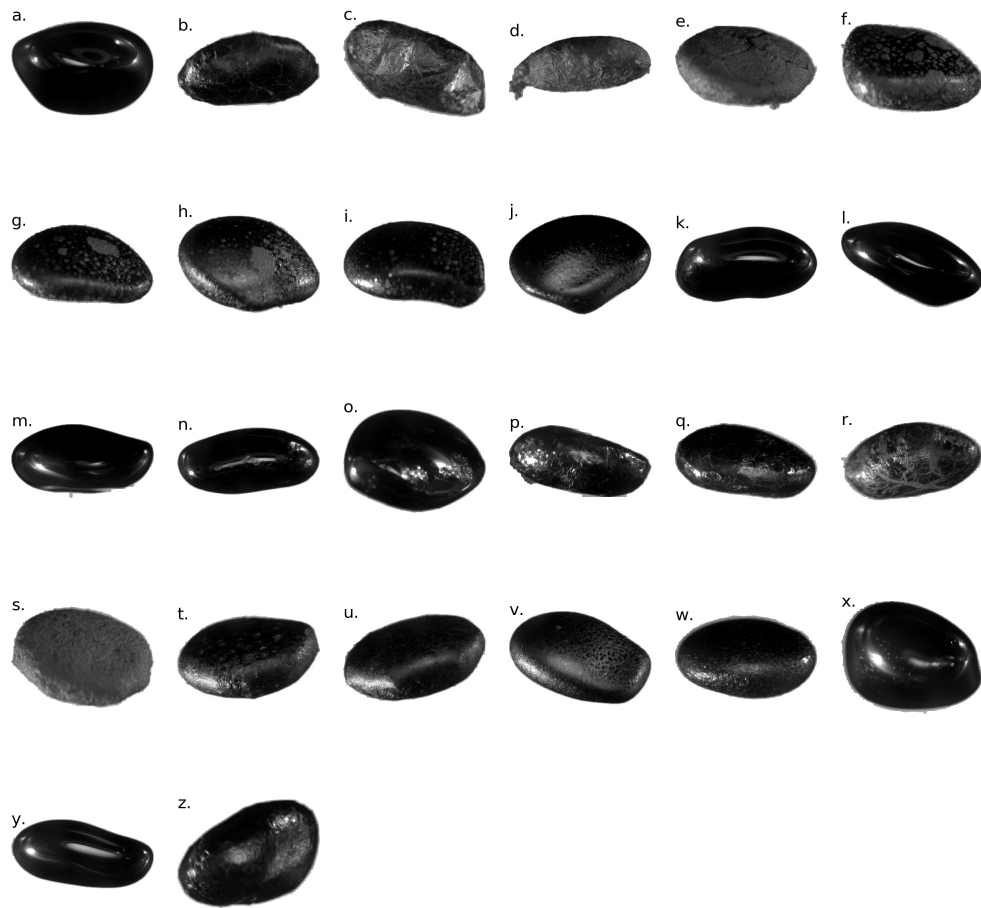


Figure 18: Bubble morphology evolution during the experiment for a C1C2C3 bubble in Seawater on June 21, 2013. Letters 'a' through 'q' correspond to the denoted experimental times 'a' through 'q' in Figure 17.

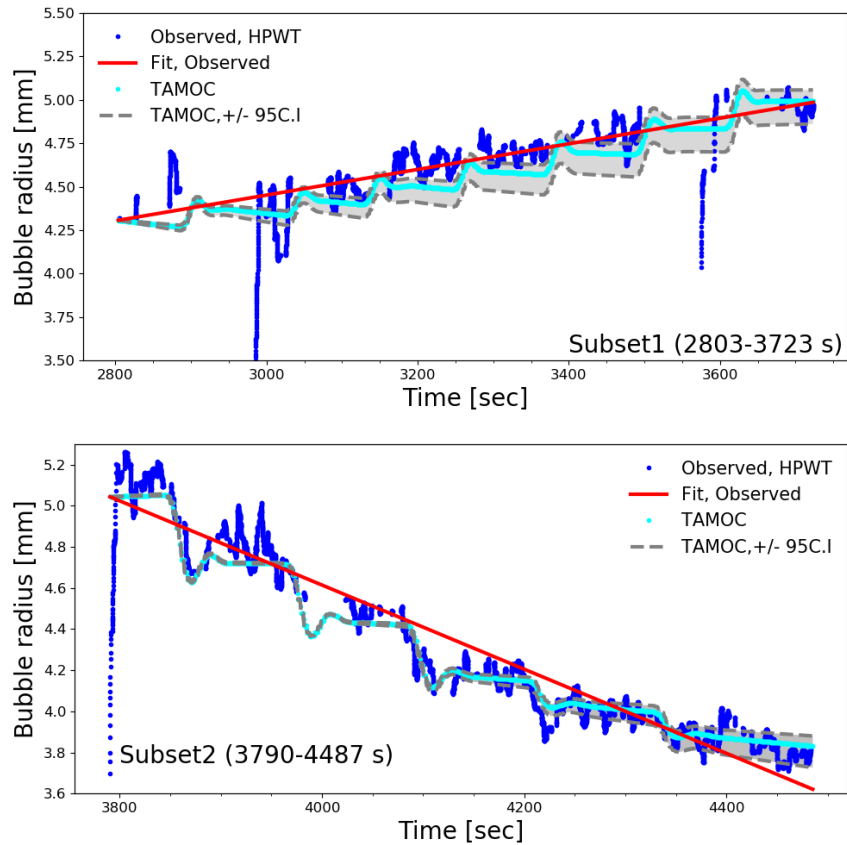


Figure 19: TAMOC simulation for a C1C2C3 bubble in Seawater while the system pressure is varying (June 21, 2013, 1st bubble; see system information and bubble morphology in Figures 17 and 18).

in response to the pressure quite well. Moreover, the mass transfer rates appear to also follow the observations quite well.

TAMOC accounts for the hydrates only by using dirty-bubble mass transfer coefficients as the base  $\beta$ -value; these simulations are based on  $C_s$  taken as the gas-liquid equilibrium concentration due to the sub-cooling being below  $11^\circ\text{C}$  in these experiments. Hence, for these experiments it does not appear that the presence of the hydrate shell significantly changes the dissolution. This conclusion matches the conclusions in Section 2 for hydrate experiments with sub-cooling less than  $11^\circ\text{C}$ , where the mass transfer line using  $\alpha = 1.9$  (see Figure 9) agreed modestly with the data, though the data has considerable scatter and error bars.

This is an encouraging result for simulating real gas bubbles within the hydrate stability zone as it would be difficult from these data to obtain correlations for modified mass transfer coefficients. Our hypothesized explanation is that the cracks and fissures present in the hydrate shell (see camera images in Figure 18) allow free gas to escape sufficiently that the hydrate armoring does not impede mass transfer. The pressure reduction rate used in the experiments was 0.14 MPa every 60 s, which closely matches the pressure reduction rates for bubbles of this size rising in the oceans. Hence, these experiments give good confidence to both the mass transfer model proposed here and the TAMOC single bubble model simulation to predict the dynamics of gas bubbles in the oceans at modest sub-cooling (less than  $11^\circ\text{C}$ ).

In other experiments with hydrates, the pressure was maintained constant for longer periods, and the mass transfer rate at constant pressure could be observed. We found two types of behavior. For sub-cooling less than  $11^\circ\text{C}$ , mass transfer still follows the results above, with dirty-bubble mass transfer coefficients and gas-water equilibrium for  $C_s$  in Equation (14). Above  $11^\circ\text{C}$ , the dominant dissolving phase becomes hydrate, and we must use the hydrate-water equilibrium for  $C_s$  in Equation(14) to predict the observed bubble sizes.

As another example of an experiment at lower sub-cooling, with  $\Delta T_{hyd} < 8^\circ\text{C}$ , consider a methane bubble in RO water on June 11, 2012 (2nd bubble), as depicted in Figure 20. Here, we identify four time periods (subsets 1 to 4, indicated as the blue shaded regions in the figure) with constant system pressure and  $\Delta T_{hyd}$  ranging from about  $7^\circ\text{C}$  to  $8^\circ\text{C}$ . Images of the methane bubble during representative times (times ‘a’ though ‘i’ in Figure 20) are shown in Figure 21. From the camera images, hydrate begins to form at the end of subset 2 and is fully formed near the beginning of subset 3.

A TAMOC single bubble model simulation for the experiments in Figures 20 and 21 is presented in Figure 22. The model is re-initialized at the start of each subset (blue shaded regions in the figure). While not really necessary between subsets 1 and 2, when hydrates are not present, it

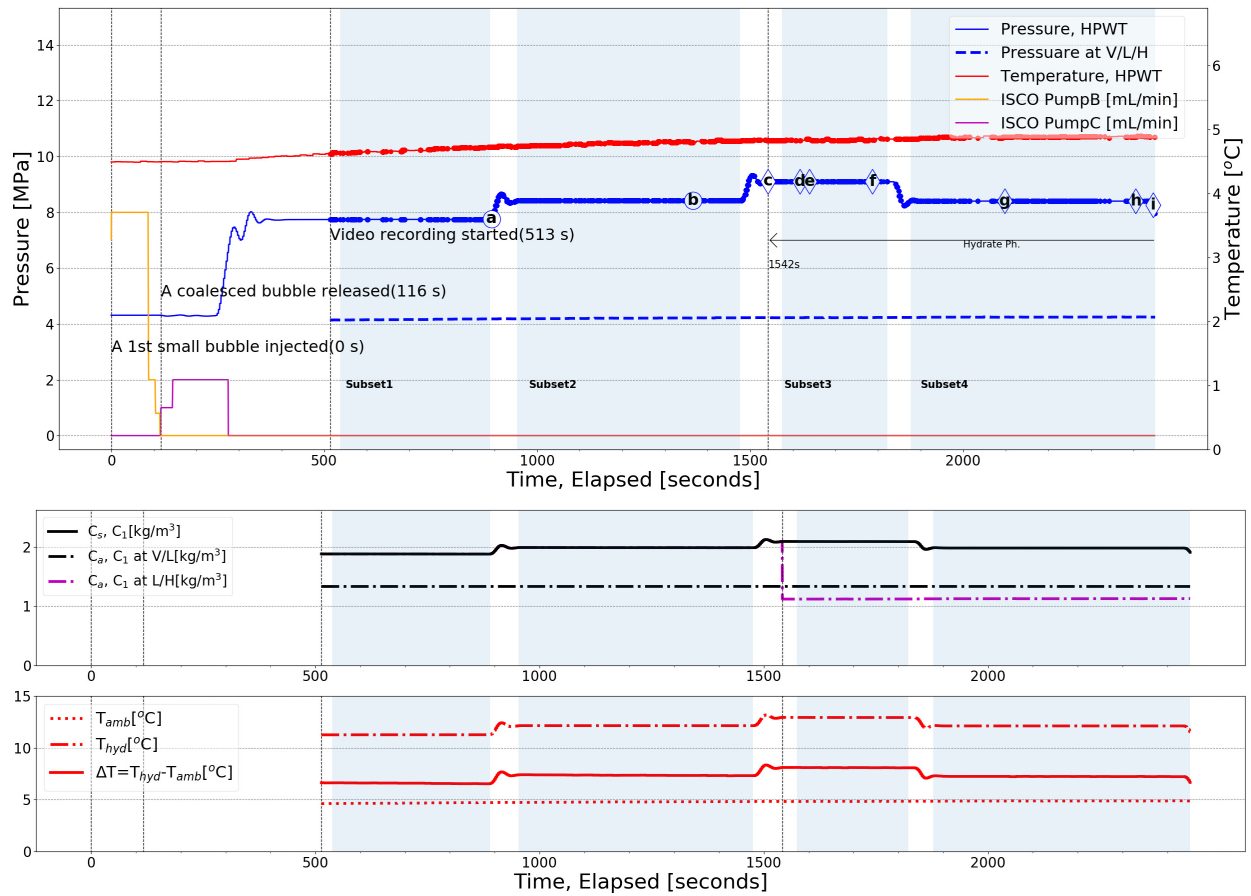


Figure 20: System information of NETL HPWT facility during the experiment for a CH<sub>4</sub> in RO water on June 11, 2012, 2nd bubble. The bubble is fully covered with hydrate skin at 1542 sec (time 'd', refer to camera images in Figure 21). Pressure is shown in the upper panel, concentration in the middle panel, and temperature in the lower panel.

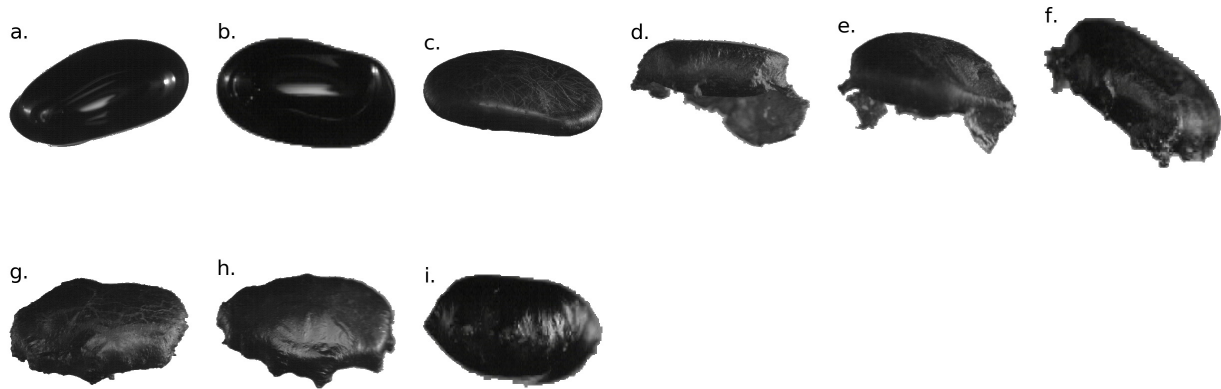


Figure 21: Bubble morphology evolution during the experiment for a CH<sub>4</sub> bubble in RO water on June 11, 2012. Letters ‘a’ through ‘i’ correspond to the denoted experimental times ‘a’ through ‘i’ in Figure 20.

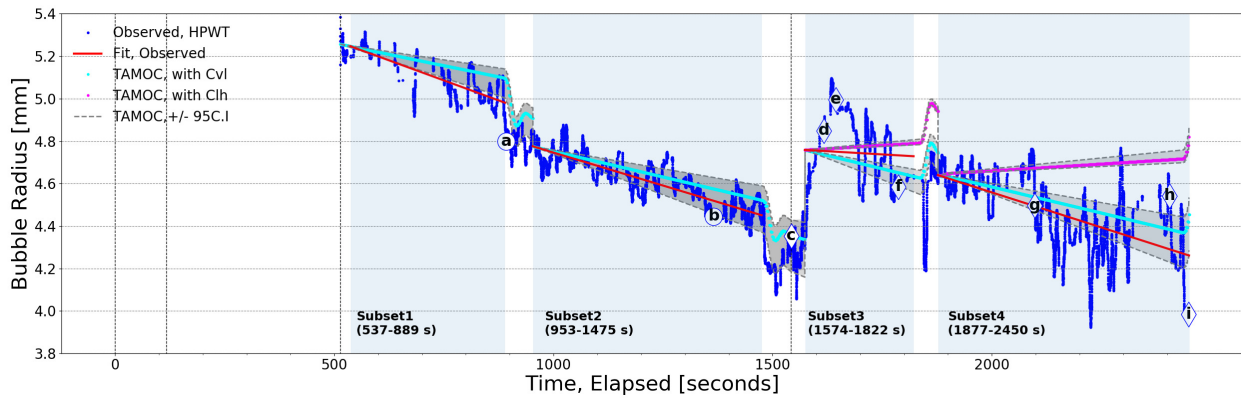


Figure 22: TAMOC simulation for a CH<sub>4</sub> bubble in RO water during periods of extended constant pressure (June 11, 2012, 2nd bubble; see system information and bubble morphology in Figures 20 and 21).

was important for subsets 3 and 4 as the hydrate flakes attached to the bottom of the bubble artificially increase the bubble sizes through the errors they cause in the image analysis. Hence, to best understand the model-data comparison, a representative bubble size at the start of each subset is used in the model.

During subsets 1 and 2, no hydrate skins were observed in the camera images, and the model predicts the mass transfer using dirty bubble mass transfer coefficients with  $\alpha = 1.9$  and using the vapor-liquid (gas-water) equilibrium concentration for the solubility  $C_s$  in the mass transfer Equation (14). During subsets 3 and 4, hydrates were observed to fully coat the bubble-water interface. We show two different simulations for these periods. In both simulations, the mass transfer coefficients are taken as the dirty-bubble empirical values with  $\alpha = 1.9$ . For the cyan curve,  $C_s$  remains the vapor-liquid equilibrium concentration, and the model assumes that free gas is still the dominant phase undergoing dissolution. For the magenta curve,  $C_s$  is taken as the liquid-hydrate equilibrium concentration. Because the water tunnel was super-saturated with respect to the liquid-hydrate system, the model predicts that the bubble should have been growing under for this model. Though the experimental times are short for each of these subsets and the observed bubble sizes vary considerably as the bubble wanders within the observations window, it is clear that the observed bubble sizes track better with the simulations using  $C_s$  for the vapor-liquid system than for hydrate-liquid. Hence, these results further affirm our conclusions for the experiments with variable pressure: at modest sub-cooling ( $\Delta T_{hyd} < 11^\circ\text{C}$ ), mass transfer rates are unaffected by the hydrate skins, and free gas remains the dominant dissolving phase, subject to dirty bubble mass transfer coefficients in the dissolution model.

As an example of an experiment at higher sub-cooling, consider the results in Figures 23 and 24. Four subset times are selected as the blue shaded region in Figure 23, where the pressure was maintained constant, and the sub-cooling ranged from  $17.5^\circ\text{C}$  to  $14.5^\circ\text{C}$ . Again, the model is re-initialized at the start of each subset, and two TAMOC single bubble model simulation results are shown in the comparison figures (Figure 23). For each TAMOC simulation, dirty bubble mass transfer coefficients are used with  $\alpha = 1.9$ . For the cyan curve, the solubility  $C_s$  is taken as the hydrate-liquid equilibrium concentration; for the magenta curve  $C_s$  is the vapor-liquid equilibrium concentration. For each subset, the cyan curve follows the observed bubble sizes closely, but the magenta curve deviates significantly. Hence, for constant-pressure conditions at these high sub-cooling temperatures, hydrate is the dominant phase dissolving, and gas is protected inside by the hydrate shell.

In each of these experiments at high sub-cooling, the background dissolved gas concentration is near the hydrate-liquid saturation concentration, and the bubbles are not observed to dissolve.

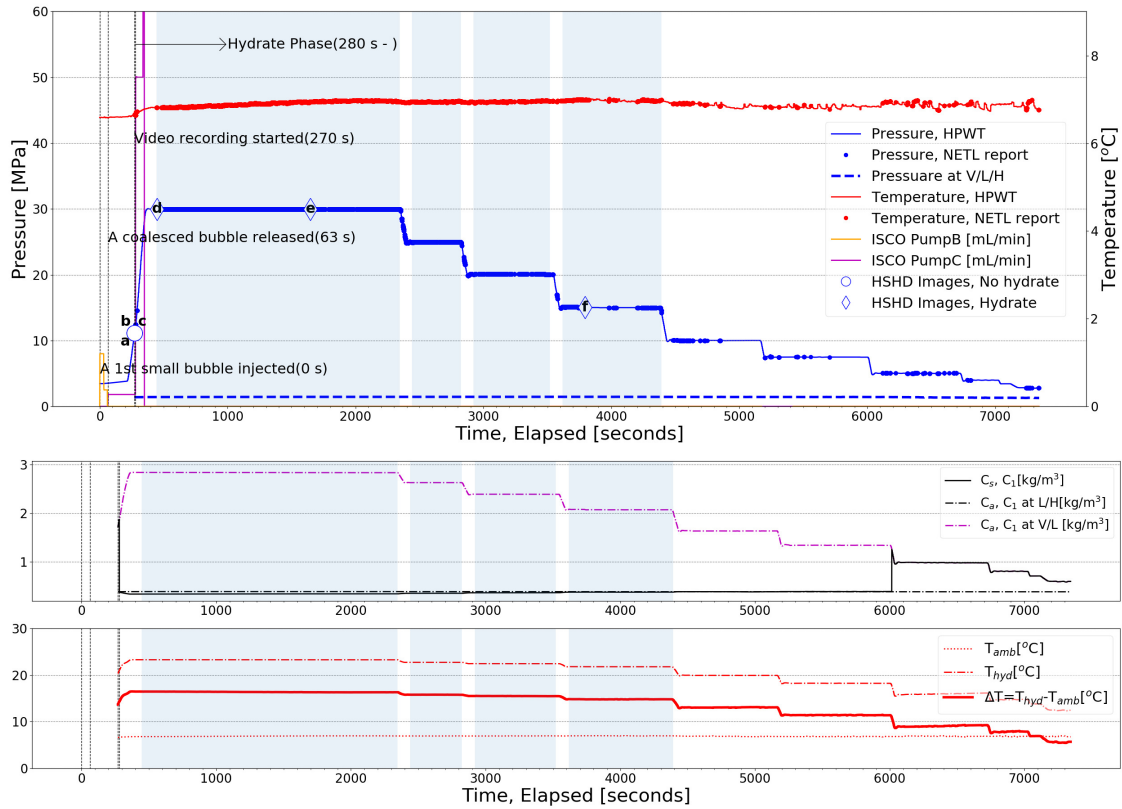


Figure 23: System information of NETL HPWT facility during the experiment for a C1C2C3 bubble in Seawater, March 13, 2014, 1st bubble. The bubble is fully covered with hydrate skin at 280 s. Pressure is shown in the upper panel, concentration in the middle panel, and temperature in the lower panel.

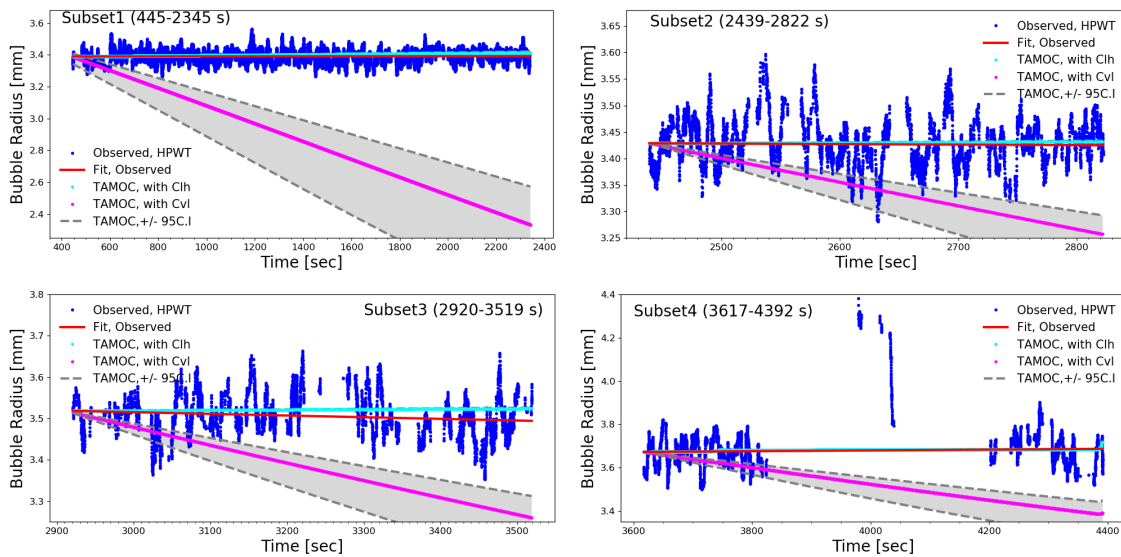


Figure 24: TAMOC simulations for a C1C2C3 bubble in Seawater during periods of extended constant pressure (March 13, 2014, 1st bubble; see system information in Figure 23).

While the model also predicts this condition well, these experiments do not allow us to fully test the mass transfer coefficients for this case. However, because all other experimental conditions are predicted well by dirty bubble mass transfer coefficients with  $\alpha = 1.9$ , there is no reason to believe these hydrate-coated bubbles would not behave as typical dirty bubbles. Thus, we conclude that our model choices in these cases are likely correct even when the background dissolved gas concentration reduces, as it would in the oceans above a seep.

In summary, we have evaluated TAMOC single bubble model simulations a wide range of experimental conditions. This section has demonstrated typical examples. These include gas bubbles with and without hydrate at pressures well above the hydrate stability pressure. In all simulations, we use dirty-bubble mass transfer coefficients with a mass transfer amplification factor of  $\alpha = 1.9$ , which accounts for the background turbulence of the pipe flow in the HPWT test section. For all experiments without a hydrate shell and for experiments with hydrates but at sub-cooling less than  $11^\circ\text{C}$ , the saturation concentration  $C_s$  in the mass transfer Equation (14) should be taken as the vapor-liquid (gas-water) equilibrium concentration. When the hydrate sub-cooling exceeds  $11^\circ\text{C}$  and the pressure is maintained constant, hydrate becomes the dominant dissolving phase, and  $C_s$  should be taken as the hydrate-liquid (hydrate-water) equilibrium concentration. These experiments span most conditions in the deep ocean for natural seeps or potential accidental subsea blowouts; hence, we conclude that our single bubble model is well-validated to realistic conditions for natural gas bubbles in the oceans within the hydrate stability zone.

#### 4.4.3 Quantification of model performance using HPWT dataset

We performed a rigorous quantification of model errors using the same stratified dataset for training and validation as presented in Section 2. This includes 230 separate experiments over a wide range of pressures and representative range of bubbles sizes in the 2 mm to 10 mm range. Refer to Figure 6 for the statistics of the samples in each of these datasets. In this section, no further training was conducted, and the model was always run using dirty-bubble mass transfer coefficients, a mass transfer amplification factor of  $\alpha = 1.9$ , and setting the saturation concentration  $C_s$  in the mass transfer Equation (14) equal to the vapor-liquid equilibrium concentration.

Several different error statistics could be selected. When considering the plots of model predictions versus observed bubble size (e.g., Figure 14) it is clear that there is considerable scatter in the measured data resulting from parallax errors as the bubble moves about in the single-camera field of view. These types of errors should not be accounted as model error. As an alternative, we decided to compare the model prediction for bubble size at the end of an experiment with the observed value. This is an integrative statistic, as small model errors at each time step accumulate

into a final, larger error at the end of the simulation. The observed value is taken from the best-fit line through the measured data, which removes the variability of the instantaneous observations. This results in 230 pairs of predicted and observed data, one pair for each experiment.

Figure 25 shows the statistics of the percent relative error for various aggregations of the data. The percent relative error was computed as

$$\epsilon = \frac{|\hat{r} - r|}{r} \cdot 100\% \quad (16)$$

where  $\hat{r}$  is the predicted ESR from the TAMOC single bubble model at the end of an experiment and  $r$  is the observed ESR. The mean model error including all experiments is 10% with a standard deviation of 8%. This is an acceptably low error, especially considering the integrative nature of the comparison, using the bubble size predicted at the end of an experiment. Errors were the smallest for C1C2C3 bubbles in seawater plus dispersant (lower right subplot), where the mean error was 4.2%, yet the largest errors were for C1C2C3 bubbles in just seawater, with a mean error of 12%. These differences reflect the fact that they are subsets of the overall dataset. No model biases with respect to gas type or ambient fluid (RO water, seawater, or seawater plus dispersant) are observed. Hence, we conclude that the simulations as presented here are accurate given the available data to 10% error in the predicted bubble sizes, with a standard deviation of 8%.

In the remainder of this report, we further validate the single bubble model in TAMOC using field data collected during the GISR cruises and selected field data reported in the literature. For these validation studies, we apply the model using the calibration results obtained above. In particular, we recommend and make the following choices for field-scale simulations:

- In the laboratory, we always applied dirty-bubble mass transfer rates as these are normally expected except under very specialized, clean conditions. In the field, our analysis above shows that bubble may initially behave as clean bubbles, evolving to dirty-bubble behavior after a few minutes. At the field scale, we release bubbles in the simulations using clean-bubble mass transfer coefficients, and switch the model to dirty-bubble mass transfer coefficients after the transition time  $t_{hyd}$  given by Equation (11) in Section 3, above.
- In the laboratory, the background pipe flow turbulence in the test section gave rise to the mass transfer amplification factor  $\alpha$ , which we used as 1.9 in the HPWT experiments. The background turbulence in the oceans is orders of magnitude less energetic, and we select  $\alpha = 1$  for all field-scale simulations.
- Based on the experiments in the HPWT, it appears that free gas is the main contributor to dissolution from the bubbles except at high sub-cooling (greater than 11°C) and constant

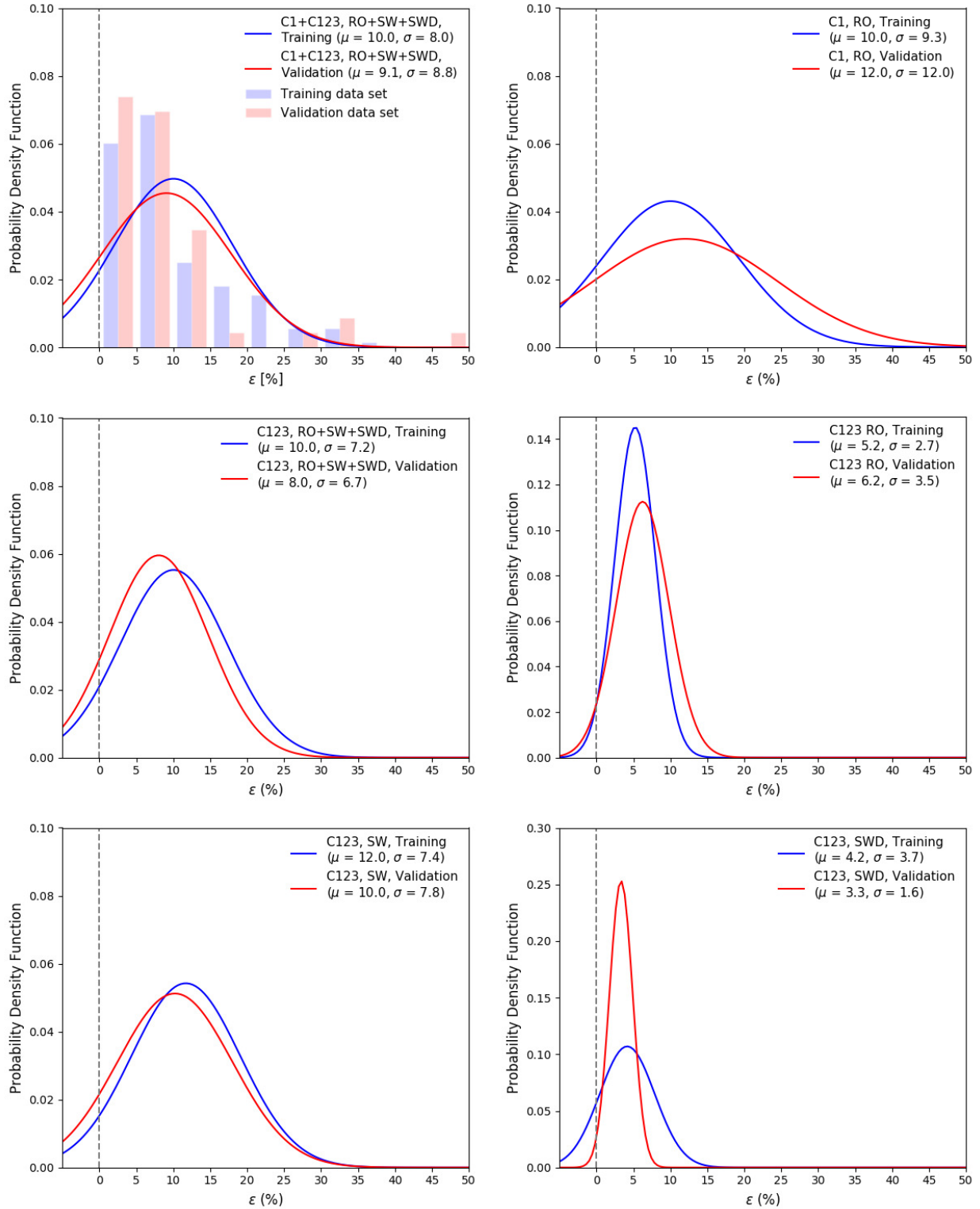


Figure 25: Model error quantification between TAMOC simulation results and HPWT observations for bubble size (ESR) at the end of each experiment. Subplots report results for various aggregations of the data; refer to the legend in each subplot for details of the included experiments.

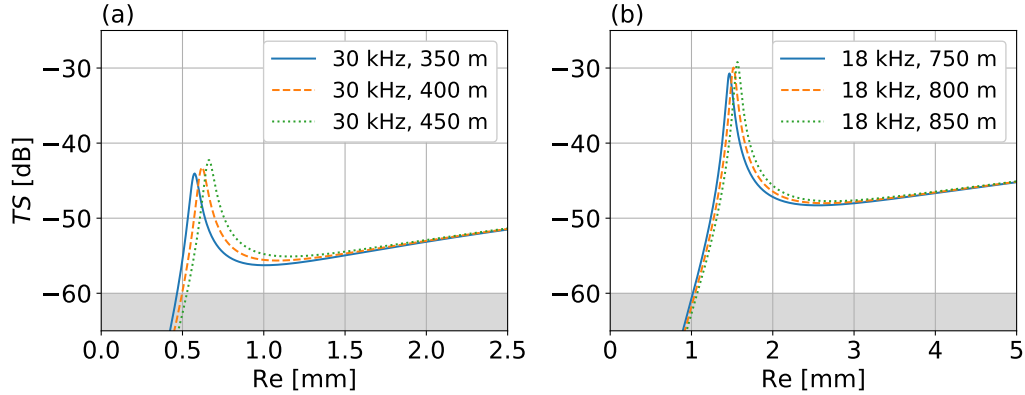


Figure 26: Computed acoustic target strength for a methane gas bubble of different radii at the top of the seep for the echosounder in the GISR experiments and those experiments reported in (Römer et al., 2012).

pressure. The field-scale examples in the following text mostly have sub-cooling less than  $11^{\circ}\text{C}$  and all have rising bubbles, experiencing pressure reduction over time. Hence, we always use the vapor-liquid equilibrium concentration as the saturation concentration  $C_s$  in the mass transfer Equation (14).

With each of these model uncertainties constrained and selected based on the model calibration and validation above, the remaining sections of this report validate the seep model (the single bubble model in TAMOC) to additional field observations from the GISR cruises and from selected seeps reported in the literature.

#### 4.5 Application of seep model to GISR and other field data

The most common measure for the performance of a seep model to predict natural seep dynamics in the oceans is to compare the model prediction for bubble rise heights with the rise height observed in haul-mounted acoustic multibeam data. Typical multibeam echosounders for deepwater utilize 30 kHz or 18 kHz acoustic beams. At these wavelengths, bubbles are smaller than an object that would normally reflect the beam back toward the sensor, but because of their small density relative to water, they do experience resonance of their bubble-water interface in the excitation of the acoustic beam. This resonance results in a large noise that is received by the multibeam receiver and allows gas bubbles to show up as bright targets in the water column anomalies of acoustic multibeam data (Römer et al., 2012).

Figure 26 shows the acoustic response of natural gas bubbles of different equivalent spherical radii (Re in the figure) as a function of water depth, which affects the density of the bubbles. Bubbles

in the millimeter size range have a fairly uniform acoustic backscatter, with a peak occurring at the resonance point. Bubbles smaller than the resonant size have rapidly diminishing acoustic backscatter, and become acoustically transparent. In the figure, we have shaded the region at -60 dB as the sound pressure level below which the bubble would be indistinguishable from background noise in most acoustic multibeam surveys. Based on the figure, 30 kHz systems can observe bubbles about 0.6 mm in radius and above; 18 kHz systems can observe bubbles about 1.6 mm and above. This information is critical when comparing model predictions for bubble rise height with acoustic observations of natural seep bubble flares.

Here, we selected measurements for model validation reported for natural gas seeps in the Gulf of Mexico from Wang et al. (2016) (the GISR G07 and G08 cruises) and from offshore Pakistan from Römer et al. (2012). We selected these two studies because they include both hydro-acoustic measurements of the seep flares using haul-mounted multibeam and *in situ* observations of the gas flow rates and bubble size distributions at the seafloor using imaging from an ROV. The *in situ* CTD and ROV data is important to provide accurate initial conditions for the model simulations, and these data are generally lacking for studies that report only the hydro-acoustic observations of seep flares.

#### 4.5.1 Gulf of Mexico

We use data from the Gulf of Mexico from the GISR G07 and G08 cruises. See Table 6 in Appendix A for all data sources. Wang et al. (2016) observed two natural gas seep sites, one in MC 118 and another in GC 600, during two different cruises, the G07 cruise in July 2014 and the G08 cruise in April 2015. These two natural seep sites are in water depths of about 1,000 m, well within the hydrate stability zone (HSZ) for methane and for the gases emitted at these sites. The GISR cruises collected field measurements around natural seeps to characterize the bubble flares and their fate in the water column. They measured the ambient water column conditions, bubble size distribution at the seafloor, the gas composition and gas flux at the emission point, and the maximum height of rise of the seep flares in the water column for each natural seep site.

The temperature and salinity data were obtained by a Conductivity-Temperature-Depth (CTD) sensor mounted on the frame of the ROV during the cruises. The ambient dissolved gas profiles (oxygen, nitrogen, and argon) are estimated due to a lack of field measurements. To compute these, we estimate the aqueous solubility of air at the air-water interface, then correct for seawater compressibility and temperature at all water depths. The computed argon and nitrogen profiles are similar to the observed profiles in McGinnis et al. (2006). Biological processes may alter the oxygen profile, and the estimate computed here is used for the lack of any observational data.

The bubble size distribution and gas flow rate at the source point were measured using a high-speed stereoscopic camera system mounted on the ROV. These are reported here in Appendix B. For the model simulations, we use the fitted log-normal distributions of bubble size for the initial conditions of the model. For the observations at MC 118 during G07, the ROV could not reach the emission point (it was in a depression), and the measured initial bubble size distribution was observed after hydrate formation. For this experiment, we set the hydrate formation time  $t_{trans}$  to zero. For all other experiments at GC 600 during G07 and at MC 118 during G08, we could observe the seafloor bubble size distribution, and we use the transition time given by Equation (11).

For the gas flow rate of each seep on each dive, the high-speed camera system was used to measure the bubble size and bubble rise speed simultaneously. By measuring and counting bubbles as they passed a virtual horizontal line, the flow rate could be estimated. In addition, gas bubbles were collected from the seeps during the ROV dives, and the gas composition of these bubbles was measured by gas chromatography. The bubbles contain 68.7 - 87.6 % of methane and some longer-chain hydrocarbons, including ethane and propane. We use these measured gas flow rates and gas compositions to initialize and run the model.

For the GISR cruises, acoustic images of the entire flare trajectory were obtained from the acoustic anomaly in the water column by a haul-mounted Kongsberg EM 302 multibeam echosounder. See Appendix D for images of the observed flares. The sonar frequency was 30 kHz with an angular coverage sector of up to  $140^\circ$  with 864 soundings per ping. The achievable swath width on a flat bottom will normally be up to six times the water depth. The data from the EM 302 were post-processed using the Watercolumn module of the Fledermaus software package.

#### 4.5.2 Pakistan offshore in the Arabian Sea

Römer et al. (2012) observed submarine hydrocarbon seep sites on the Makran continental margin (offshore Pakistan) in the Arabian Sea and reported field measurements about the ambient conditions and bubble characteristics. They obtained the CTD profile with the dissolved oxygen data, and the other dissolved gas profiles (nitrogen and argon) were computed using the procedure described for the GISR cruise data, above. Römer et al. (2012) analyzed the initial bubble size distribution for each flare site by analyzing the high-definition camera images from the ROV and reported the average molecular composition of hydrocarbons in the bubbles based on analysis of collected gas samples. The bubbles at these sites consisted primarily of methane (over 99.944 %) with a small percentage of ethane, propane, and butane present.

In addition, Römer et al. (2012) investigated the water column signature of the seep flares using the ship-mounted parametric sediment echosounder system (PARASOUND). The primary sonar

frequency of PARASOUND is 18 kHz, and the nominal transducer spreading angle is  $4^\circ$ , resulting in a footprint size up to 7% of the water depth. The primary frequency of 18 kHz allowed the recording of hydro-acoustic anomalies in the deep water column.

### 4.5.3 Data comparison method

As explained above, we initialize the seep model with measured bubble size distributions, gas flow rates, and gas composition. We seek to compare the model predictions for bubble trajectory with observations from the ship-mounted acoustic instruments. As bubbles become smaller than the resonant frequency, they are expected to quickly become acoustically transparent. Yet, in the model simulations, their sizes are not yet negligible (order 2 mm in diameter), and they are predicted to continue to rise. This is further complicated by the fact that a relatively wide size spectrum of bubbles is released from the seafloor so that bubbles of different sizes will shrink to acoustically transparent sizes at different heights in the water column. To handle these factors and make a meaningful model-data comparison, we postulated three possible mechanics to explain where a natural seep bubble flare will disappear in the acoustic data. These three hypotheses are:

1. The water column backscatter is the sum of the acoustic target strength within the sample volume of the multibeam, and the bubbles will disappear when the integrated target strength falls below the ambient noise or measurement resolution of the multibeam. In this hypothesis, all bubbles exiting the seafloor combine at each measurement height to predict the flare rise height.
2. The bubbles spread out enough that the multibeam will sense the bubble plume as long as one bubble has a target strength large enough to be above the noise level of the instrument. In this case, the largest bubbles exiting the seafloor can be used alone to predict the flare rise height.
3. The flares will remain observable as long as a certain percentage of the initial gas flow rate is still present in the bubble flare. Like hypothesis 1, all bubbles exiting the seafloor combine to predict the rise height, but it is the bubble mass and not their acoustic backscatter that sets the criterion for being observable.

Each of these hypotheses assumes that some bubbles continue to rise above the observed flare height and that the flare height observed in multibeam data corresponds to some criteria for which the bubbles become acoustically transparent or at least indistinguishable from background.

To use these three criteria, we must convert the model predicted bubble evolution to an evolving target strength of acoustic backscatter. We follow the approach in Weber et al. (2014). Each bubble has its own target strength ( $TS$ ), the acoustic backscatter produced by that bubble due to the insolification by the sonar having a specific frequency level. The  $TS$  can be expressed as

$$TS = 10 \log_{10} \frac{r^2}{(f_R/f - 1)^2 + \delta^2}. \quad (17)$$

Here, we use the formulation for  $f_R$  and  $\delta$  in Medwin and Clay (1998), which depend on the interfacial tension between the bubble and water and the densities of the bubble and seawater. Each of these properties is contained within the equations of state in TAMOC.

#### 4.5.4 Results

We calculate the flare height using the three different approaches outlined above and compare the results with the observed maximum flare heights in the acoustic observations. The model is run as described above for all cases except for flare 5 reported in Römer et al. (2012). For that flare, the source point (2,870 m) is much deeper than the model calibration range (500 - 1,500 m) for the hydrate transition time. Through previous analysis, we found that the hydrate formation time could be zero if the degree of hydrate sub-cooling is large enough. In order to match these data, we set the hydrate transition time to zero; simulations using the predicted transition time do not rise high enough in the ocean water column.

As an example, consider a result using our second hypothesis. We run the seep model to predict the maximum rise height using characteristic bubble sizes from the measured bubble size distribution and compare the target strength of individual bubbles with the noise level criteria we assumed for these sonar data (refer to Figure 26). We simulate three representative large bubble sizes ( $d97$ ,  $d98$ , and  $d99$ ), which are the intercepts for 97%, 98%, and 99% of the cumulative bubble size distribution.

Figure 27 plots the evolution of each of these bubble sizes with height together with the measured flare heights from the acoustic data. The grey area on the left-hand-side of each subplot represents the assumed noise level of the acoustic data (-60 dB), which corresponds to a 0.5 mm radius bubble for the GISR cruise data and a 1.0 mm radius bubble for Römer et al. (2012) (refer also to Figure 26). Using this method, we find that initial bubble sizes between  $d97$  and  $d99$  reach the top of the flare at sizes that are visible to acoustic measurements.

To test whether bubbles with this probability are expected to pass within the acoustic sample volume while the ship transits over a seep, we use the measured flow rate to predict the emission frequency of these bubble sizes. In the seeps simulated here, the emission frequency of large

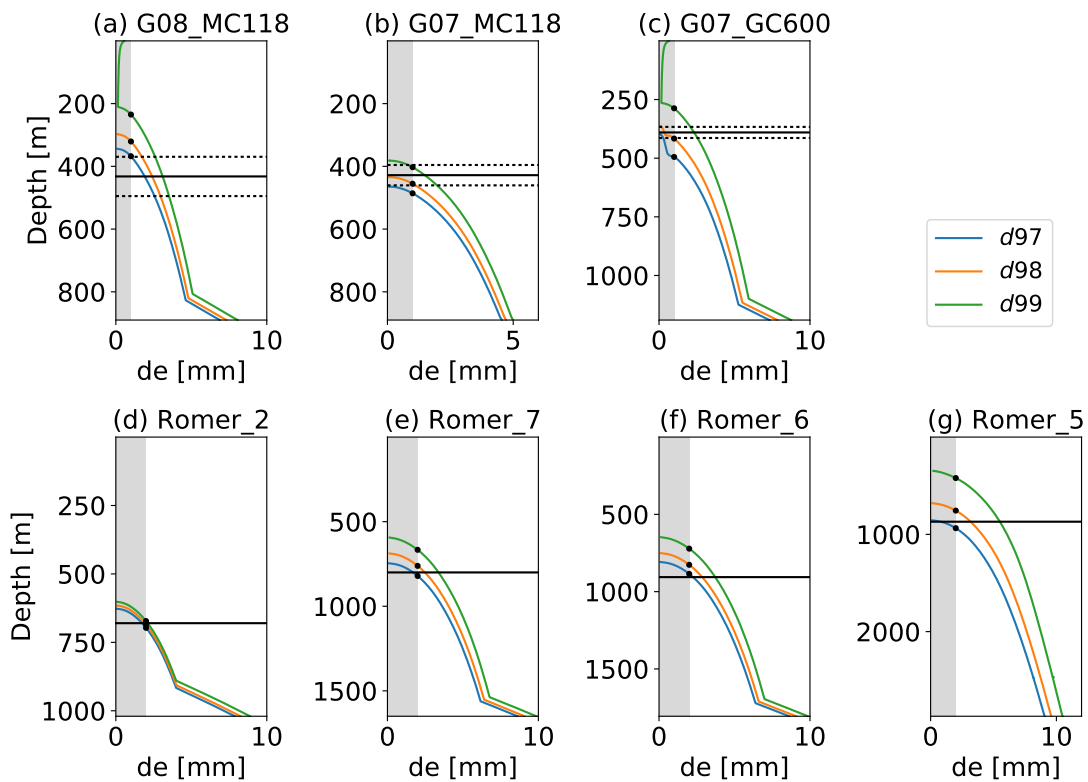


Figure 27: Prediction of natural seep flare height using the target strength of the representative large bubbles ( $d_{97} - d_{99}$ ) through the water depth with noise level of acoustic data (gray shaded region).

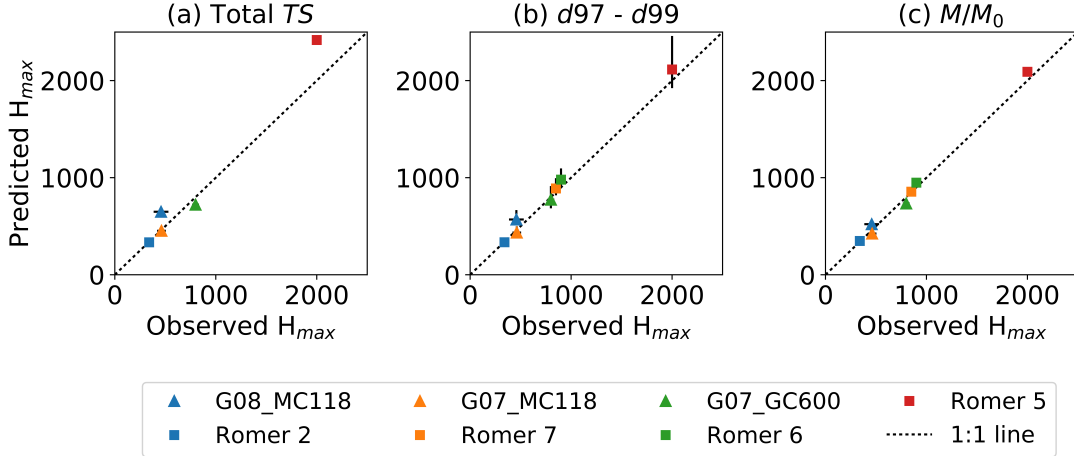


Figure 28: Comparison of model performance for the three different approaches to predict the top of a natural seep flare using acoustic data: (a) The total  $TS$  of all bubbles, (b) the target strength of the representative single bubble, and (c) the ratio of the remaining mass in the flare to the initial release mass.

bubbles is between 2.2 and 13.3 bubbles per second, depending on the case. These data support our modeling hypothesis, which is that the large bubble sizes remaining at the top of the flare may be the primary bubbles responsible for the acoustic observation, and the top of the flare should correspond to the depths where these bubbles become acoustically transparent. An advantage of this hypothesis over the other two is that it is not necessary to know the seep flow rate. It is also not important to know the full bubble size distribution, though it is necessary to estimate the diameters of the largest bubbles occurring at the seep source.

To evaluate all three hypotheses, Figure 28 shows a comparison between predicted and observed flare height for each of the three different approaches. Based on our full model-data analysis, the criteria for the model-predicted top of the flare under each postulated mechanism are:

1. The height at which the predicted  $TS$  for all bubbles remaining in the flare drops below -50 dB.
2. The range of heights for which the acoustic target strength of the  $d_{97}$  to  $d_{99}$  bubble sizes at the source reduce to -60 dB.
3. The height at which 0.1% of the released mass remains in the bubble flare.

The error bars in the figure show the uncertainty for the predictions and observations. The horizontal error bars describe the standard derivation for the measured height-of-rise data, while the vertical error bars indicate the prediction results for the different bubble sizes (i.e., only Hypothe-

Table 4: Summary of the simulation results for the prediction of flare rising height

Case	Observed $H_{max}$	Predicted $H_{max}$		
		Hypothesis 1	Hypothesis 2	Hypothesis 3
G08_MC118	457.83	649	569	521
G07_MC118	461.88	453	435	425
G07_GC600	799.72	722	774	735
Romer 2	340	334	335	348
Romer 7	850	-	889	856
Romer 6	900	-	980	948
Romer 5	2000	2418	2114	2091
$R^2$		0.93	0.98	0.99
bias		103 m	41 m	16 m
PE		9.85 %	4.68 %	1.49 %

sis 2 yields a predicted height range for bubbles in the range  $d97 - d99$ ; the other methods predict a single rise height).

We summarize the fit statistics of the data in Figure 28 in Table 4; the result for Hypothesis 2 is shown in the table for  $d98$ , only. The  $R^2$  values between the prediction and observation are over 0.9, and the averaged values of relative percentage error ( $\epsilon$ , see Equation (16)) are less than 10% for all three methods. The total  $TS$  method (Hypothesis 1) gives the least accurate result of the three methods for the maximum flare height, although this method is the most intuitive prediction because the comparison between total  $TS$  and the measured flare height using sonar data is more direct than the other two methods. The disadvantage of this method is that it is only applicable when the flow-rate and bubble size distribution are known since we must evaluate a statistical realization of the total  $TS$  for all bubbles in the flare. The method is also the most complicated as one must estimate which bubbles lie within the acoustic beam of the instrument. The single bubble  $TS$  method (Hypothesis 2) gives a better prediction compared to Hypothesis 1 with the shortest computing time. Also, this method can be used without knowing the flow-rate information—only an estimate of the bubble size distribution or the diameter of the largest bubbles is required. The method using the mass remaining (Hypothesis 3) gives the best prediction accuracy among the three approaches. Like Hypothesis 1, to compute the mass remaining one requires an estimate of the complete bubble size distribution, but a unit flux can be applied; hence, this method is intermediate among these three methods in terms of the required understanding of the initial conditions.

From the model evaluations, we conclude that all three methods have merit and skill to predict the maximum flare height. For the application when the gas flow rate is unknown, we recommend using the single bubble  $TS$  method (corresponds to Hypothesis 2). The single bubble  $TS$  method

assumes that the acoustic measurement can detect bubbles when the resonance of the largest single bubble is larger than the ocean ambient noise level, taken here as -60 dB. This assumption relies on the assumption that only one large bubble is needed at the top of the flare to be observable and that the flare spreading is enough so that the sonar may only sense a single bubble in each ping and interrogation window. The main advantage of this method is the good prediction accuracy, with the acceptable error for the seeps analyzed here of 4.68% or 41 m, respectively for *d98*.

This analysis also validates the calibration and adjustments of the single bubble model in TAMOC presented above using the HPWT and Rehder et al. (2009) data to understand the dynamics of single bubbles in conditions relevant to the ocean water column. Here, no further adjustments to the model have been made. Instead, we use the model to compare different approaches to understand observations of natural seep flares in acoustic data. Our analysis indicates that our model and interpretation methods are accurate for predicting observed seep rise heights to within 5% to 10% error, error levels nearly identical to those comparing model predicted bubble sizes to the HPWT data. Based on these laboratory and field validations, we accept the single bubble model as reasonably accurate for predicting natural seep dynamics in the oceans.

## 5 Apply Seep Model to Interpret GISR Multibeam Data

Once the seep model was calibrated and validated using both the HPWT and GISR field data, the final task of this project was to use the validated model to extract more quantitative information about the natural seeps contained in the acoustic data collected during the GISR cruises. These data were collected from two sources: a forward-looking Kongsberg M3 sonar mounted on the ROV and a haul-mounted Kongsberg EM 302. These instruments operate at very different frequencies and collect different levels of information about these seeps from different perspectives. The original goal of the project was to determine whether these data could be used to verify the presence of hydrate shells in the field and whether the acoustic data could validate additional aspects of the seep model predictions, beyond that of the seep rise height. While this exercise uses acoustic theories, it is not an exclusively acoustics-related research task, but rather an attempt to maximize the usage of the acoustic data in validating the numerical seep model. Hence, we use acoustic algorithms available in the literature.

The plume cross-sectional data from the M3 represents acoustic data from an uncalibrated instrument. We performed new experiments in the Offshore Technology Research Center (OTRC) to calibrate the M3 and then validate a method to extract gas flow rate from the M3 images of simulated natural seep plumes. The instrument calibration allows us to convert measurement level

to target strength, and the flow rate calibration allows us to estimate gas flux in natural seeps from M3 cross-sectional data. This latter calculation requires knowledge of the bubble size distribution at any height, which we obtain for the field from the seep model developed here.

Full water-column trajectories of the natural seeps were observed using the EM 302. These data were already used above in Section 4.5 to validate the rise-height prediction of the natural seep model. Here, we utilize the target strength observed by the EM 302 and compare that to target strength estimated from solutions of the seep model. Unlike for the M3, Kongsberg provides a calibration algorithm to convert EM 302 measurement level to relative target strength. Comparing the measured and modeled results, we further validate the conclusions on rise height presented above (Section 4.5) and gain further insight into the structure of the acoustic signal of natural seeps as it evolves with height in the ocean water column. The following sections detail the outcomes of using these two field datasets with our natural seep and acoustic models.

## **5.1 Application of seep model to GISR M3 data**

The M3 multibeam sonar is an uncalibrated instrument. To use this sonar for quantitative acoustic analysis, calibration and validation experiments were required. These were conducted through Task 5 of this project in the Offshore Technology Research Center (OTRC) deepwater wave basin. We then applied the calibration curve obtained in the laboratory to the observations in the field. To ensure that this extension is possible, in addition to calibrating the M3 in the OTRC, we also created several artificial natural seep plumes and measured their acoustic response using the M3. This allowed us to reliably compute integrated target strength for plume cross sections measured by the M3 in the field. Because our laboratory calibration was limited to 10 m range, the field application should be used with caution outside of this range, where the calibration must be extrapolated. The following sections explain our analysis and present the main field results.

### **5.1.1 Calibration experiments in the OTRC wave basin**

The calibration experiment was conducted in a large wave basin located in the OTRC at Texas A&M University. The main wave basin is 5.5 m deep, with a pit having a water depth of 17 m in the center of the basin. To simulate natural seep bubble flares, air bubbles were released using two different diffusers from the bottom of the pit. These bubbles rose about 12 m before entering the field of view of the sonar. One diffuser was an aquarium air stone (AS) and the other was a single, straight orifice (SO) with a diameter of 0.8 mm drilled in a PVC pipe. These two diffusers could generate bubbles with different size distributions at the same flow rate (Li et al., 2020). The



Figure 29: Photographs of (a) The mounted M3 sonar on the underwater tower. (b) The Tungsten Carbide ball used for calibration.

purpose of using two diffusers was to test the sensitivity of our acoustic algorithms to estimate the gas flow rate for different bubble size distributions. Five different flow rates were used for each diffuser and were measured by two mass flow meters (GFM models, Aalborg Instruments & Controls, Inc.), see Table 5.

Table 5: Measured flow rate and median bubble diameter for each case.

Diffuser type	Case number	Gas flow rate at the source, $Q_{g,0}$ (L/min)	Median bubble diameter, $d_{50}$ (mm)
Air stone	ASQ1	0.24	2.53
	ASQ2	0.73	2.80
	ASQ3	1.15	3.20
	ASQ4	1.91	3.27
	ASQ5	3.06	3.31
Single orifice	SOQ1	0.24	4.60
	SOQ2	0.73	3.98
	SOQ3	1.15	3.19
	SOQ4	1.91	3.07
	SOQ5	3.06	3.31

A Kongsberg multibeam M3 sonar<sup>®</sup> was used to measure acoustic backscatter of air bubbles in the wave basin. The sonar was mounted on a rigid, underwater tower at 1-m above the main basin floor, using a forward-looking configuration, similar to that of the M3 mounted on the ROV during the GISR experiments. See Figure 29a. The sonar operates at a frequency of 500 kHz and has a range resolution of up to 1 cm. In this work, the ‘profiling’ mode was used to obtain a sampling rate of 40 Hz at 256 beams with a field of view of 120° (Kongsberg, 2020). The instrument range was set to 5 m for all cases to obtain standardized measurements. To test the sensitivity of the range selection used in the field experiment, we performed additional measurements using a 10 m range for large flow rates (i.e., ASQ4, ASQ5, and SOQ5). Due to the strong backscatter from the

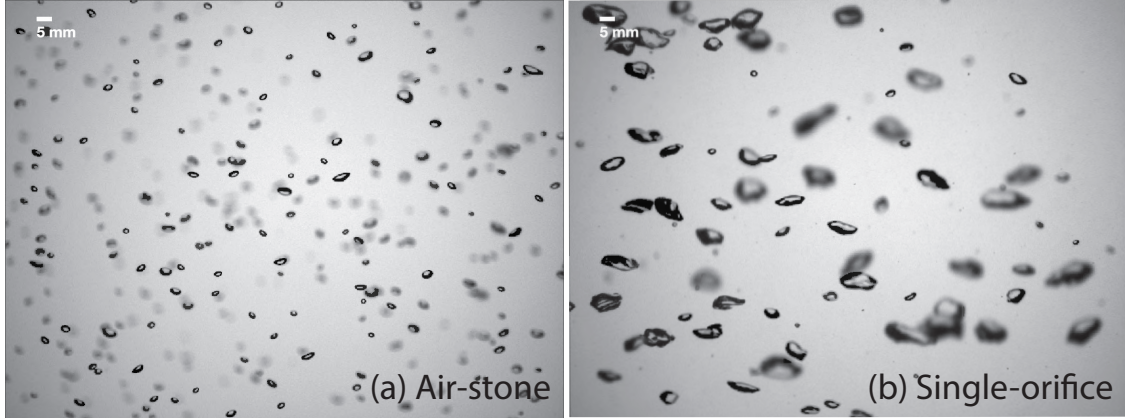


Figure 30: Sample images of bubbles generated from different diffusers: (a) air-stone; (b) single-orifice.

concrete walls of the wave basin and the center pit, we were not able to test instrument ranges beyond 10 m.

A shadow imaging underwater camera (Prosilica GC1380H) was used to measure the bubble size distribution prior to the acoustic measurements at the same height where the sonar images were taken. We collected 4,800 bubble images with a sampling rate of 8 Hz for each case of flow rate and diffuser combination, resulting in 10 minutes of total data. These sampling periods were selected to obtain converged bubble size distribution measurements. Examples of bubble images for the two diffusers are shown in Fig. 30. The air-stone diffuser generated smaller bubbles than the single-orifice at low flow rates, but the sizes from both diffusers became similar at large flow rates (see also Table 5). The bubble images were processed to compute bubble size using an in-house algorithm developed for quantifying hydrocarbon seep bubbles (Wang and Socolofsky, 2015a; Wang et al., 2016), similar to that presented in Section 2, here.

### 5.1.2 M3 sonar calibration results

Sonar calibration was performed prior to the plume measurements. A 14.3-mm diameter Tungsten Carbide ball (density of  $14,970 \text{ kg/m}^3$ , see Fig. 29b) was used for calibration. A spherical ball is a standard calibration target as it can be treated as a point target and its acoustic response is unidirectional (Dragonette et al., 1981; Foote and MacLennan, 1984). The target strength ( $TS$ ) of the calibration ball is calculated to be  $-48.02 \text{ dB}$  following the Standard Sphere Target Strength Calculator provided by NOAA’s Southwest Fisheries Science Center (<https://swfscdata.nmfs.noaa.gov/AST/SphereTS/>).

The calibration ball was suspended in the field of view of the sonar using a fishing line. The ball

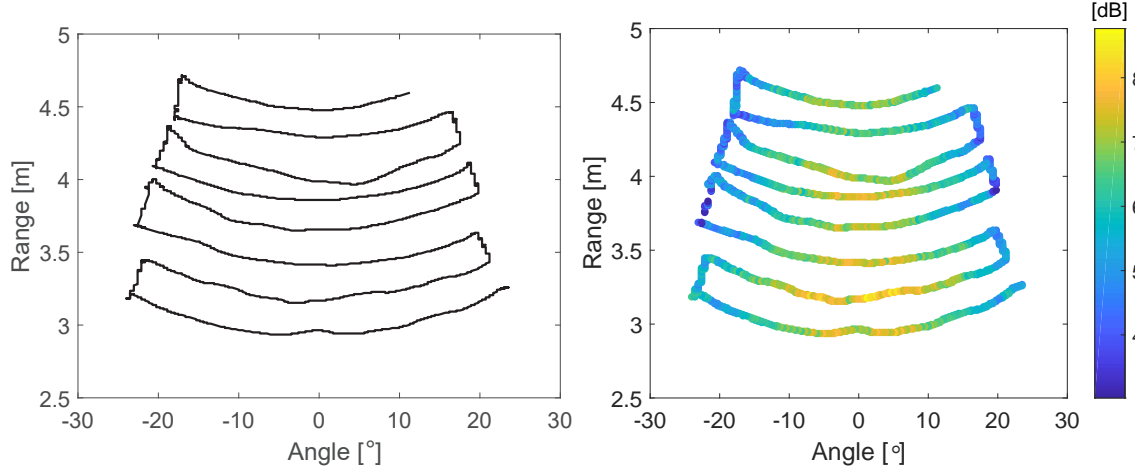


Figure 31: (a) Ball trajectory during the calibration in the field of view of the sonar at 5 m range; (b) uncalibrated measured level [dB] due to the back scatter from the calibration ball.

was carefully adjusted to the same height as the sonar head, giving the strongest acoustic return. We slowly moved the calibration ball in the horizontal direction, covering the main area of field of view where the bubble plumes would be measured. Figure 31 shows the ball trajectory and the uncalibrated M3 measurement level during the calibration experiment in the 5 m range. Because the experiments were carried out at two sonar ranges (5 m and 10 m), calibration was repeated for each range.

A sonar calibration model is developed to relate measured acoustic intensity to the theoretically calculated target strength. Figure 32 shows an example of a single sonar image of the calibration ball using the 5 m range. The calibration ball returns a strong acoustic intensity at its location, and there is a significant, corresponding side-lobe effect due to beam forming.

The calibration model is focused on backward conversion of the theoretical target strength  $TS$  of the calibration ball from the map of uncalibrated (or unspecified) measurement level ( $ML$ ), which is defined from the logarithm of the acoustic intensity measured by the M3 sonar (e.g., the values reported in Figure 31b). Here, we only used the maximum intensity measured at the ball location for development of the calibration model as we will later show the side lobe effect due to beam forming is secondary compared to the directivity caused by the acoustic transmitting and receiving.

Figure 33 shows the unspecified  $ML$  as a function of range and beam angle in the field of view (FOV) of the M3 sonar. The data shows the  $ML$  is inversely correlated to the range and the beam angle. The varying  $ML$  as a function of range and angle is due to different transmission loss ( $TL$ ) and instrument adjustment (functions of range) and different echo levels ( $EL$ ) as a result of transmitter/receiver directivity, which is a function of beam angle. The parameters constructing

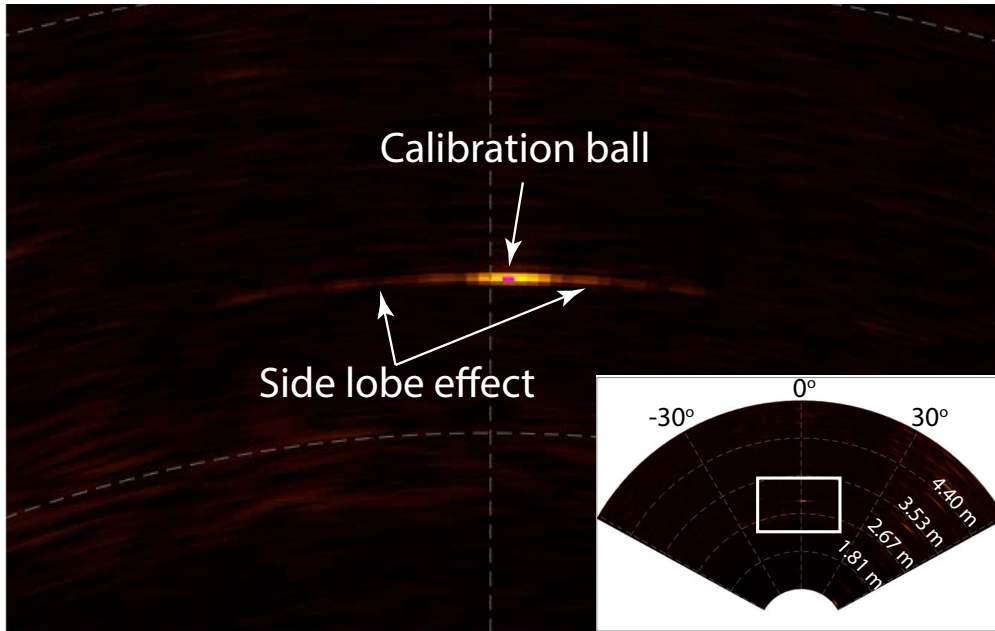


Figure 32: An example of zoom-in sonar image of the calibration ball. The data shows the strongest intensity at the location of the ball and the side lobe effect due to beam forming. The insert is the full field of view of the sonar image.

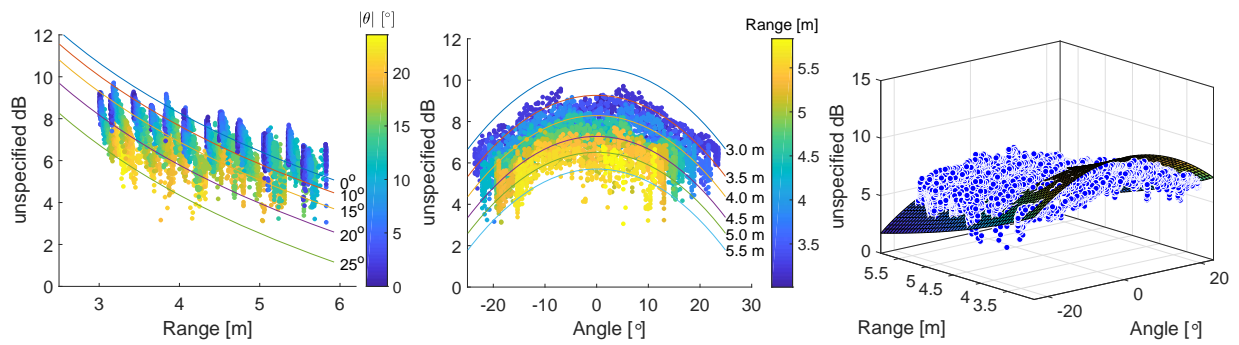


Figure 33: Comparison between the measured acoustic intensity in the format of unspecified dB and the best-fit of calibration model. (a) unspecified  $ML$  vs. range; (b) unspecified  $ML$  vs. angle; (c) 3D scatter plot of data vs. model.

these functions must be determined to derive a calibration model for the instrument.

At the instrumentation level, the measured level  $ML$  of the M3 sonar is related to the received echo level ( $EL$ ) of the backscatter and is adjusted by the instrument internal algorithms. Because the measured M3 acoustic intensity is unspecified, a calibration term must be added to connect unspecified  $ML$  to the actual  $EL$  from the target. The general acoustic equation is

$$ML = EL + Gain + TVG \quad (18)$$

where a constant  $Gain$  value must be calibrated for each sonar, and the time varying gain  $TVG$  for the M3 is defined as:

$$TVG = \min(A \log(R) + 2BR/1000 + C - 20TX_{power}, L) \quad (19)$$

where  $R$  is the range of the target and coefficients  $A = 20$ ,  $B = 100$ ,  $C = -16$ , and  $L = 100$  are predefined.  $TX_{power}$  takes the value of 0 or 1 depending on the range selection for  $<$  and  $>$  5 m, respectively.

From the sonar point of view,  $EL$  is related to the  $TS$  through a typical sonar equation, given by

$$EL = SL + DF + TS - 2TL \quad (20)$$

where  $SL$  is the source level,  $DF$  is the directivity function combined from the transmitter (Tx) and receiver (Rx), with  $DF = 0$  dB giving the maximum intensity of the transmitter and receiver, and  $TL$  is the one-way transmission loss, given by  $TL = 20 \log(R) + \tau R$ , with  $\tau$  being the absorption coefficient. We examined estimation of  $\tau$  using the Francois-Garrison and Thorp models (Lurton, 2002), which give similar estimation of  $TL$  in our experimental condition.

From Equations (18) and (20), we obtain the relationship between  $ML$  and  $TS$ , where the calibration terms are shown on the right-hand-side of the equation

$$ML = \underbrace{TS + SL + DF - 2TL + Gain + TVG}_{\text{calibration term}} \quad (21)$$

In Equation (21),  $DF$  is a function of angle. We use the model provided in Lurton (2016), namely

$$DF = 20 \log_{10} \left( \left| \frac{\sin E}{E} \right| \right) \quad (22)$$

where  $E = \pi \sin(\theta)/\Delta\theta_E$ . Lurton (2016) pointed out the exact directivity pattern should depend on the physical design of the sonar, but a single value of  $\Delta\theta_E$  provides a good approximation for the purpose of deriving directivity models.

Equation (21) is the calibration model we applied here, where  $SL + Gain$  and  $\Delta\theta_E$  are two model parameters to be fitted from the data. Using the curve fitting toolbox of Matlab, the two

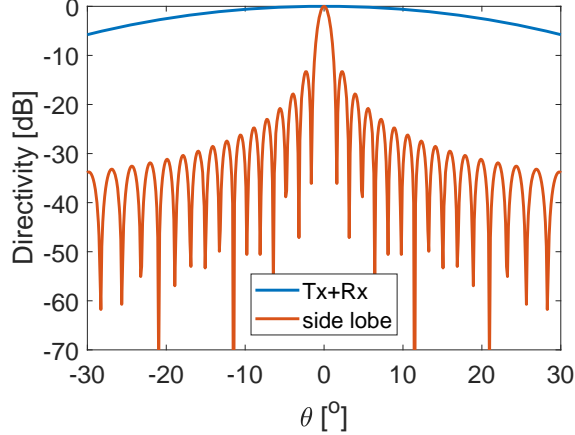


Figure 34: Comparison between transmission directivity due to the combined transmitter and receiver (Tx+Rx) and due to the side lobe effect of beam forming pattern.

model parameters are determined. Using the best-fit of  $ML$  in the model, we obtain the best-fit solid lines shown in Figure 33. The fitted model has an  $R^2$  value of 0.4 and root mean square error (RMSE) of 0.89 dB. The model seems to overestimate the data for short ranges and underestimate the data for long ranges.

As mentioned above, we neglect the side-lobe effect in our calibration; yet, the side lobe effect due to beam forming is present for any target. In bubble plumes, the side lobe effect is superimposed throughout the measured intensity due to the close proximity of each bubble to another; hence, we ought to evaluate the relative importance of the directivity of the beam forming (side lobe) to the Tx+Rx directivity determined from the calibration model. In the M3 sonar, the directivity due to beam forming can be calculated as (Lurton, 2016)

$$D_{\text{beam forming}} = 20 \log_{10} \left( \left| \frac{\sin E_A}{E_A} \right| \right) \quad (23)$$

where  $E_A = \pi \sin(\theta)/\Delta\theta$ , with the M3 horizontal beam width  $\Delta\theta$  ranging from  $1.6^\circ$  to  $3.2^\circ$  ( $\Delta\theta = 102.1/N/\cos(\theta)$ ,  $N = 64$ ) expressed in radians. Figure 34 shows the comparison of sonar directivity due to Tx + Rx (Equation (22)) and due to side lobe from the beam forming (Equation (23)). The result shows  $DF$  is much higher than the intensity due to beam forming for most angles other than zero; therefore, we can generally neglect the side lobe effect in converting  $ML$  to  $TS$ .

There are some limitations to our calibration procedure and model. First, the elevation at which the calibration ball was placed may not be a constant as the ball was moved through the FOV of the sonar during the calibration, which could introduce uncertainties in the measured acoustic intensities. An improvement could be done by rotating the sonar head while maintaining the ball location at a fixed point. Second, the predefined values in the  $TVG$  equation may not accurately represent the actual instrument, which could introduce uncertainties in fitting the calibration model.

Lastly, more sophisticated calibration models may also be considered to improve the calibration. Given that the range of data was from 3.05 dB to 9.70 dB and that the RMSE model errors are only about 1 dB, the model reasonably represents the variation of the  $ML$  as a function of range and angle despite the low  $R^2$ -value. Hence, we use this model in the following analyses to convert unspecified  $ML$  to a quantified  $TS$  for any target in the sonar FOV, such as observations of bubble plumes in this study.

### 5.1.3 Model to predict gas flow rate from M3 observations

To compare the  $TS$  observed by the M3 to the properties of a bubble plume, we require the  $TS$  of a single bubble. For this, we use the acoustic model introduced above in Equation (17). Target strength is related to the acoustic back-scattering cross section  $\sigma$ , which is given by

$$\sigma = \frac{a^2}{(f_R^2/f^2 - 1)^2 + \delta^2} \quad (24)$$

where  $a$  is the bubble radius,  $f$  is the sonar frequency ( $= 500$  kHz for the M3 sonar),  $f_R$  is the resonance frequency of the bubble, and  $\delta$  is the damping coefficient due to energy loss. As above, calculation of  $f_R$  and  $\delta$  follows the empirical equations in Medwin and Clay (1998). At our experimental condition, we found the bubble diameters at resonant frequency for the M3 sonar is 0.009 mm. In this experiment (500 kHz), bubbles greater than 0.07 mm have larger target strength than that at the resonant condition. Hence, we expect the acoustic signal in our M3 measurements to be monotonically related to the bubble size and population because almost all bubbles are greater than 0.07 mm in this study.

The total target strength  $TS$  observed by the M3 over the whole cross section of the plume is the summation of the backscatter of each bubble. This can be calculated by integrating the backscatter cross section of each pixel in the sonar images after removing the noise through a thresholding method and adjusting the measurement level using the sonar calibration above. To relate this to the gas flow rate, though, requires knowledge of the bubble size distribution and population at every height, which is related to the gas flow rate, making the problem circular. To solve this problem, we use the standard unit plume approach, which has been used in water column target strength calculation for lower frequency sonars in hydrocarbon seep studies (Weber et al., 2014; Weidner et al., 2019; Wang et al., 2020). Either through observation in the laboratory (as was done in the OTRC) or by running the single bubble model with a known initial bubble size distribution (as was done for the GISR field experiments), we obtain the bubble population assuming a unit gas flow rate. We then calculate the total backscatter cross section from this unit population of bubbles in the plume by integrating the backscatter cross section of individual bubble

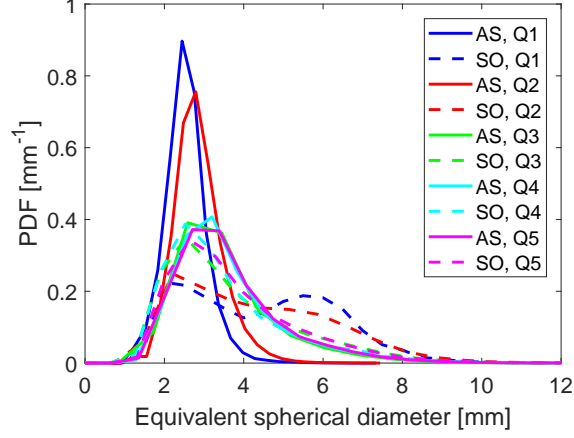


Figure 35: Measured bubble size distribution. AS: air-stone diffuser; SO: single-orifice diffuser.

sizes weighted by their probability in the droplet size probability density function (PDF). This unit integrated target strength is compared to the observed one in such a way that the gas flow rate is obtained. This procedure is derived for the M3 as follows.

The total backscatter cross section of a known PDF of bubble size  $a$  is obtained as

$$\sigma_{plume} = \int_0^{a_{max}} \sigma(a) \text{PDF}(a) da \quad (25)$$

where  $\text{PDF}(a)$  takes a dimension of  $[\text{L}^{-1}]$ , and  $\sigma(a)$  is calculated from Equation 24.  $\sigma_{plume}$  is proportionally related to the measured  $TS$  from the Sonar data, with a scale of  $N$  that can be estimated from  $N = 10^{TS/10} / \sigma_{plume}$ . Hence, the gas flux can be calculated as

$$Q = N \int_0^{a_{max}} \frac{4\pi a^3}{3} \frac{U_s(a)}{H_{M3}} \text{PDF}(a) da \quad (26)$$

where  $U_s(a)$  is the slip velocity of a given bubble size  $a$ , and  $H_{M3}$  is the vertical resolution of the Sonar FOV at the plume, which is a function of the vertical beam angle and the distance between the plume and the transducer.

To test this approach, we used the data measured in the OTRC without needing to run the single bubble model of TAMOC. Figure 35 reports the measured gas bubble size distributions for each diffuser and flow rate. Using these measured size distributions, we compute unit plume backscatter cross section according to Equation 25. Figure 36 shows the results assuming two different sonar ranges and computing  $TS$  for each diffuser and flow rate observed in the laboratory. The left-hand subplot shows the total plume target strength versus initial gas flow rate on a linear scale; the right-hand plot shows the same data on a semi-log scale. In the right-hand subplot, the data follow closely the best-fit lines. These lines report a relation between the plume gas flow rate  $Q_{g,0}$  and the computed total plume target strength  $TS$ . For the air-stone diffuser, the relationship is

$$TS = 6.69 \log_{10} Q_{g,0} - 20.70 \quad (27)$$

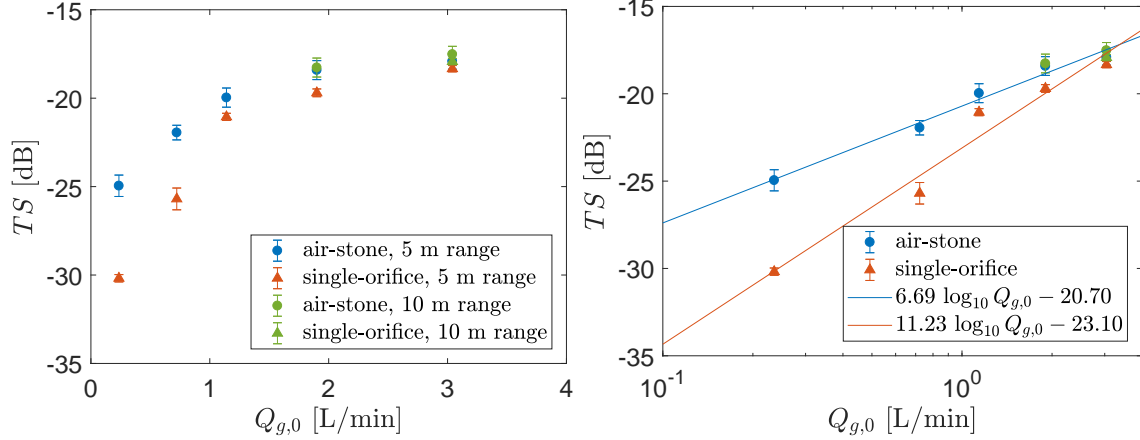


Figure 36: Calculated target strength of the bubble plume as a function of initial gas flow rate,  $Q_{g,0}$ : (a) linear plot; (b) log-log plot with the best-fit lines.

and for the single orifice, the result is

$$TS = 11.23 \log_{10} Q_{g,0} - 23.10 \quad (28)$$

where  $Q_{0,g}$  is in L/min.

We tested our ability to use these correlations to compute flow rate from  $TS$  and our sonar calibration using the OTRC data. To do this, we converted the measurement level at each pixel of an M3 image of a bubble plume to  $TS$  using the calibration procedure above. Then, we solve Equations (27) and (28) for  $Q_{g,0}$ . Finally, we compare this predicted flow rate with that measured in the laboratory using the gas flow meters. Figure 37 shows the result, where the black, 45°-line gives perfect agreement. As reported in the figure, the results have an  $R^2$  value with this perfect-agreement line of 0.84 and a relative percentage error of 23%. This level of error is very similar to the errors estimated using video cameras to compute gas fluxes from the sea floor. Hence, this performance is quite promising for using M3 sonar data on ROVs to estimate gas fluxes in natural seeps.

#### 5.1.4 Further insights gained from the M3 field data

We used the M3 field data collected during the GISR cruises to MC 118 and GC 600 to understand the rate of bubble spreading with height and to validate the calibration obtained in the OTRC experiments.

The acoustic images of the unspecified measurement level themselves already contain important information about the rate of bubble spreading in natural seep flares as bubbles rise through the ocean water column. Figure 38 shows four example images from the M3 collected at MC 118

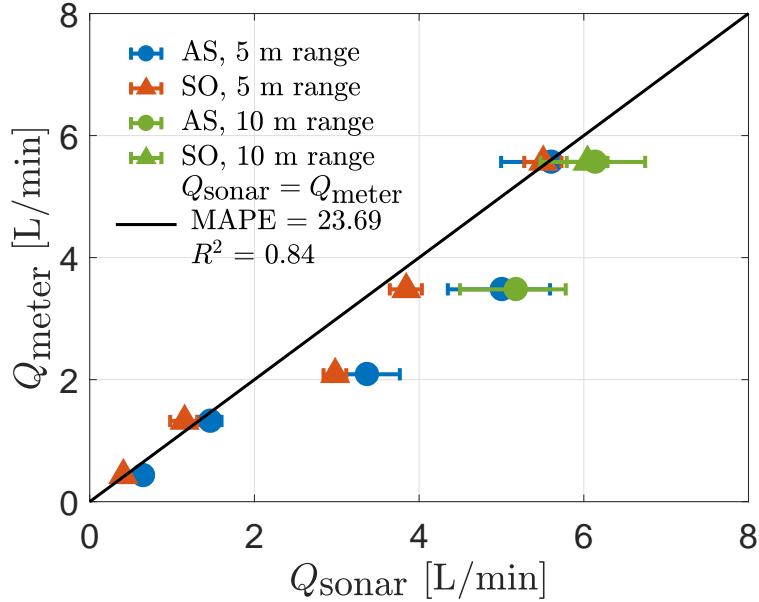


Figure 37: Comparison of gas flow rate calculated from the sonar data and measured by the flow meter. The gas flow rate measured by the flow meter was adjusted to the in situ value at the measurement location.

during the G08 (April 2015) GISR cruise. Each row of images was collected at progressively higher altitudes above the seafloor. As is clearly seen in the second row of figures, the bubble flares elongate in the along-current direction, as seen by the long tail of lower acoustic signal drifting away from the high signals in the bulk of the plume. This is a process known as fractionation, in which small bubbles with a low rise velocity are transported further downstream than larger bubbles that rise faster (Socolofsky and Adams, 2002). At the same time, the bubbles spread out laterally, normal to the mean currents. This lateral spread results from random motions that could be caused by ambient turbulence, plume entrainment, or bubble wobbling.

We computed the lateral spread of these bubble flares versus height and compared the results to various models for spreading by turbulence, plume entrainment, or bubble wobbling. Figure 39 shows the data from the M3 observations (symbols) together with various models for the bubble spread (dashed and solid lines). The dashed black line in subplot (a) gives the theoretical spreading assuming it is caused by plume entrainment. This does not track the data; hence, these bubble flares do not behave as plumes and, thus, do not have a significant upwelling velocity that would be associated with the plume effect (Wang et al., 2020). We call such a plume a weak bubble plume (Wang et al., 2019).

Because different bubbles rise at different speeds and because the ocean currents are not uniform with height, to compare this observed spreading rate with a lateral diffusion model, we must apply

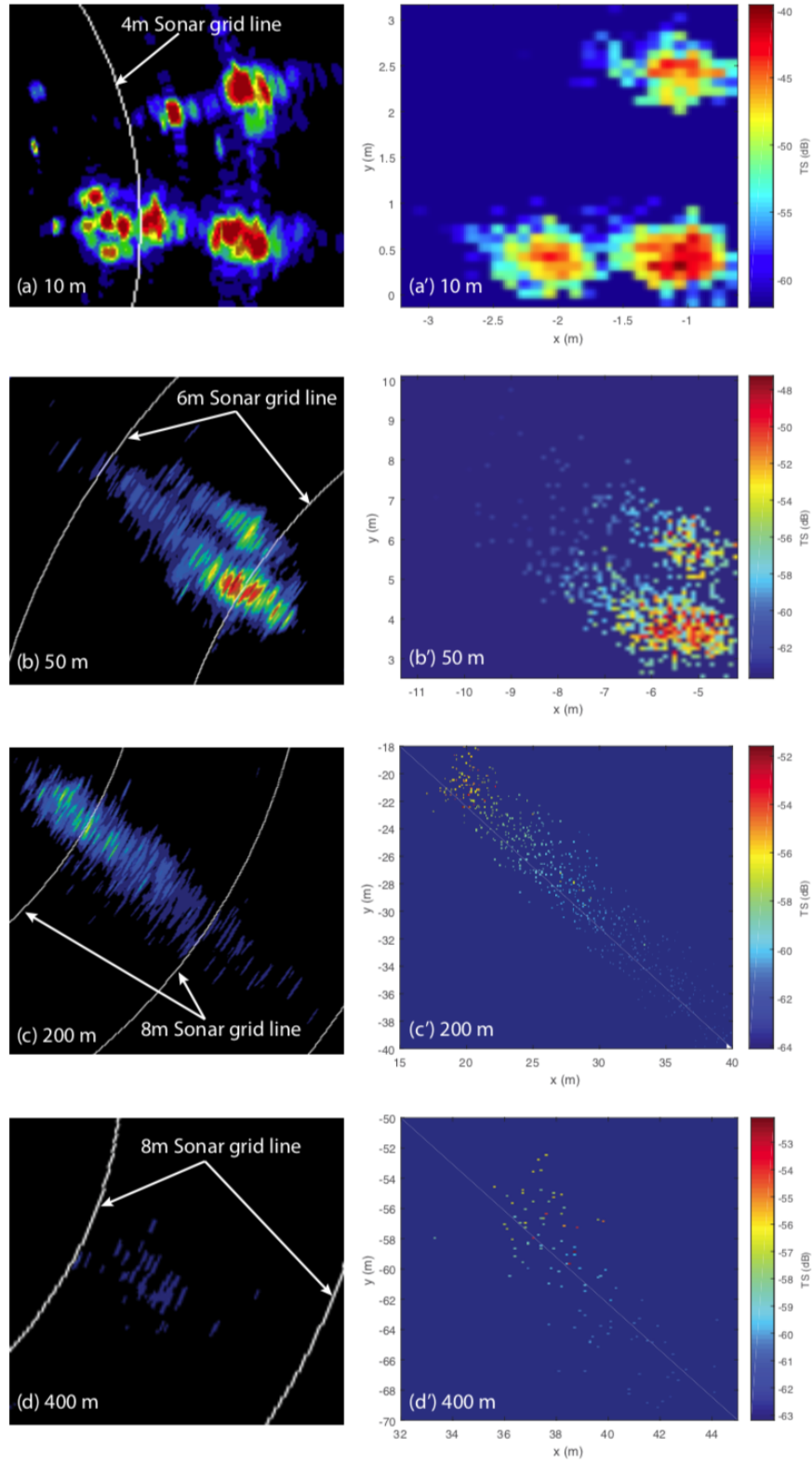


Figure 38: Comparison of instantaneous M3 acoustic images with simulated bubble position and target strength using the seep model.

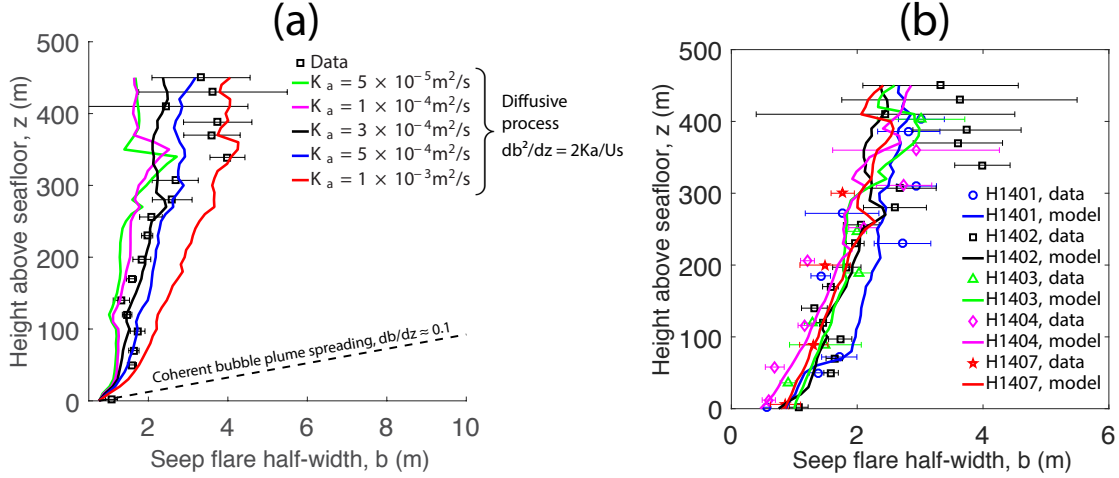


Figure 39: Lateral diffusivity of bubble flare spreading rate: (a) comparison between the measured bubble flare half-width during Dive H1402 and model results with different lateral diffusion coefficients ( $K_a = 5 \cdot 10^{-5} \sim 1 \cdot 10^{-3} \text{ m}^2/\text{s}$ ; the linear spreading rate for a coherent bubble plume is also shown as the dashed black line); (b) comparison between measured and modeled results for all dives with  $K_a = 3 \cdot 10^{-4} \text{ m}^2/\text{s}$ .

the single bubble model in TAMOC to predict the bubble trajectories given different diffusion coefficient values. To do this, we implemented a random displacement model of turbulent diffusion and ran the seep model for a range of bubble sizes using the measured bubble size distributions at the sea floor. In Figure 38, we show in the right-hand column predicted acoustic images using the seep model and an assumed lateral diffusivity. Running the model with a range of diffusivities yields different estimates for the bubble spread. These are shown as the colored lines in Figure 39(a). Based on the various results in Figures 39(a), we concluded that  $3 \cdot 10^{-4} \text{ m}^2/\text{s}$  effective diffusivity gives the best fit to the data for Dive H1402. Subplot (b) shows the model results for multiple dives using this result.

To determine the mechanisms responsible for bubble spreading, we estimated the turbulent diffusion resulting from ambient ocean turbulence and from bubble wobbling. We concluded that the observed plume spreading (i.e.,  $3 \cdot 10^{-4} \text{ m}^2/\text{s}$ ) is about 10 times greater than what would be predicted by ambient ocean turbulence, but similar in magnitude to that predicted using the excursion length scale of the bubble wobbling as the diffusion scale. Hence, three main conclusions derive from this use of the M3 data together with the seep model:

- Bubbles spread out following a diffusion process rather than by plume entrainment. Hence, natural seep flares are weak plumes with negligible entrainment or upwelling velocity.
- The dominant mechanism for lateral spreading of bubble flares in the deep ocean is the natural

wobbling motion of these ellipsoidal bubbles. For the flares observed during the G08 cruise, this effective diffusivity was  $3 \cdot 10^{-4} \text{ m}^2/\text{s}$ .

- Using a random displacement model for bubble advection in the single bubble model of TAMOC together with this observed diffusivity, model results for bubble trajectory match those observed in the M3 acoustic images

The fact that plume entrainment is negligible makes it much easier to predict the trajectories of natural seep flares as there is no need to estimate an upwelling velocity to determine the bubble rise rate. Bubbles rise in these weak natural seep flares following their empirical rates in stagnant waters.

Finally, we also used the M3 calibration procedure obtained from the OTRC experiments to compare the measured target strength  $TS$  from the M3 for the GISR field observations with predictions of target strength using our seep model.

During the GISR cruises, we used the forward-looking M3 sonar on the ROV to track the bubble flares through the water column, allowing us to make all other *in situ* observations. For much of the dive time, the M3 was recording, yielding a high-resolution vertical profile of the integrated plume cross-sectional target strength as a function of depth. An example from the G07 cruise is shown in Figure 40, where the gray dots report the instantaneous M3 measurements, and the blue symbols with error bars are the average results and measurement range at each depth. These data were collected during *Hercules* Dive H1355 in GC600 where we observed a bubble flare we named the Confetti plume. During this dive, we tracked the plume from the seafloor to about 400 m depth. Above this depth, the bubble flare could no longer be distinguished from background, and we considered this to be the point that bubbles become acoustically transparent. This height also agreed with the top of the plume as observed by the EM 302.

To validate the numerical model to these data, we simulated the Confetti plume using the bubble size distribution observed at the seafloor. Because the ROV could maneuver all the way to the seabed source, bubbles were emitted in the model clean-bubble mass transfer coefficients. After the transition time predicted by Equation (11), we switch the model to dirty-bubble mass transfer coefficients. This transition time agreed with observations at this seep sight in the field (see Figure 12, above). For this exercise, we also applied the random displacement model for random diffusion, using the diffusivity estimated above at  $3 \cdot 10^{-4} \text{ m}^2/\text{s}$ . Following the seep model simulation, the total plume target strength was computed from the model result using Equation (24) for each bubble and summing the results of all bubbles at each height.

The result of the numerical simulation is shown as the solid red line in Figure 40. The integrated

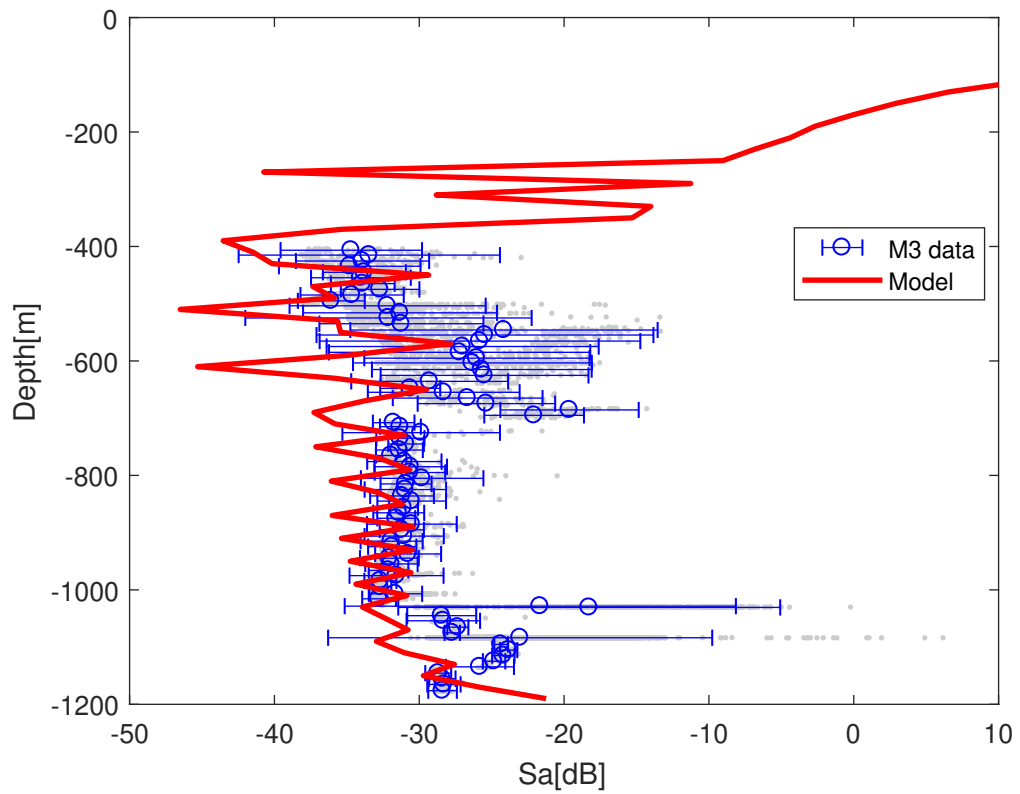


Figure 40: M3 sonar target strength and seep model prediction for GISR G07 Dive H1355 at GC600.

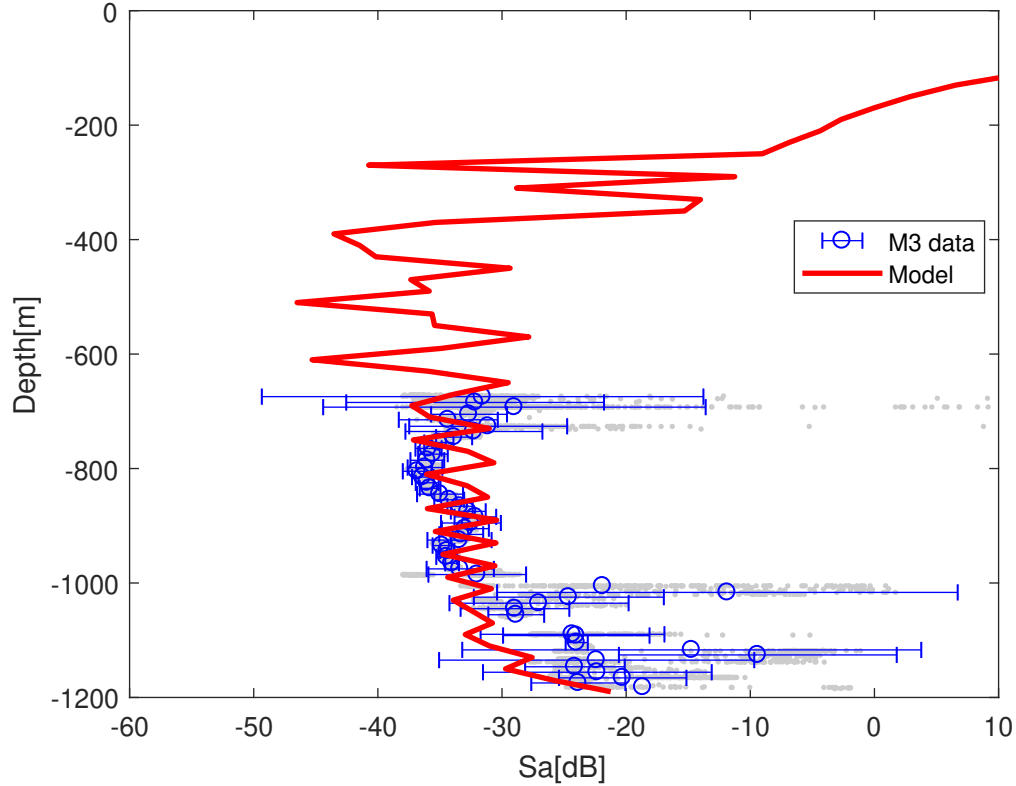


Figure 41: G07 Dive H1353 at GC600 Mega plume

target strength of the simulated plume decreases rapidly near the seafloor due to the rapid initial dissolution resulting from the clean-bubble mass transfer coefficients. The signal stabilizes within 100 m above the seafloor, and then oscillates as bubbles of various initial sizes gradually shrink through their resonant size (causing a momentary increase) and then disappear (Wang et al., 2020). The model-predicted target strength matches the observed data throughout the region where the plume was observed. Above 400 m depth, the model predicts the plume to continue to increase in target strength, but by this height the bubbles have spread out considerably and only a few bubbles remain. Although these bubbles add up to a high signal, they could no longer be contained in the M3 field of view, and the M3 ceases to see the plume. Over the range of reliable M3 data, the model appears to perform well.

Similar model-data performance is observed for other dives during G07 in the GC600 region. These are shown in Figures 41 and 42. The lack of data with height during some of these dives was caused by the different dive plans during each dive. We have shown all available data in these figures.

Results are somewhat different for the observations at Woolsey mound in MC118 during the G07 cruise. Figure 43 shows the measured and predicted data. These were some of the first observations

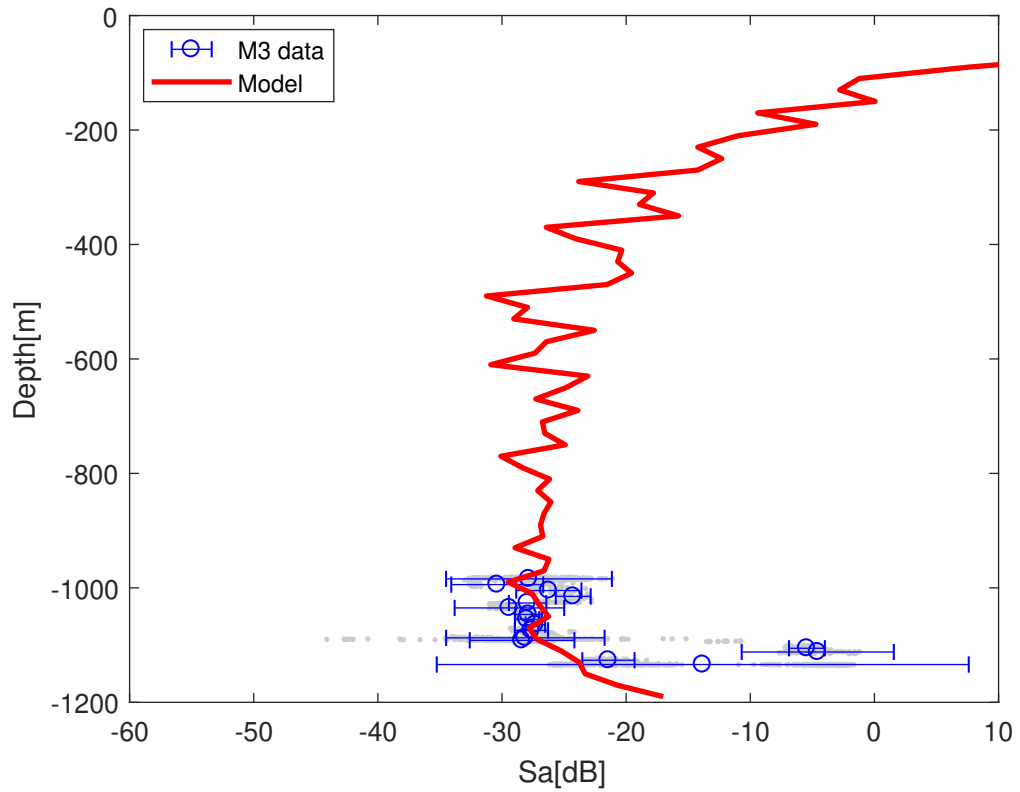


Figure 42: M3 sonar target strength and seep model prediction for GISR G07 Dive H1354 at GC600.

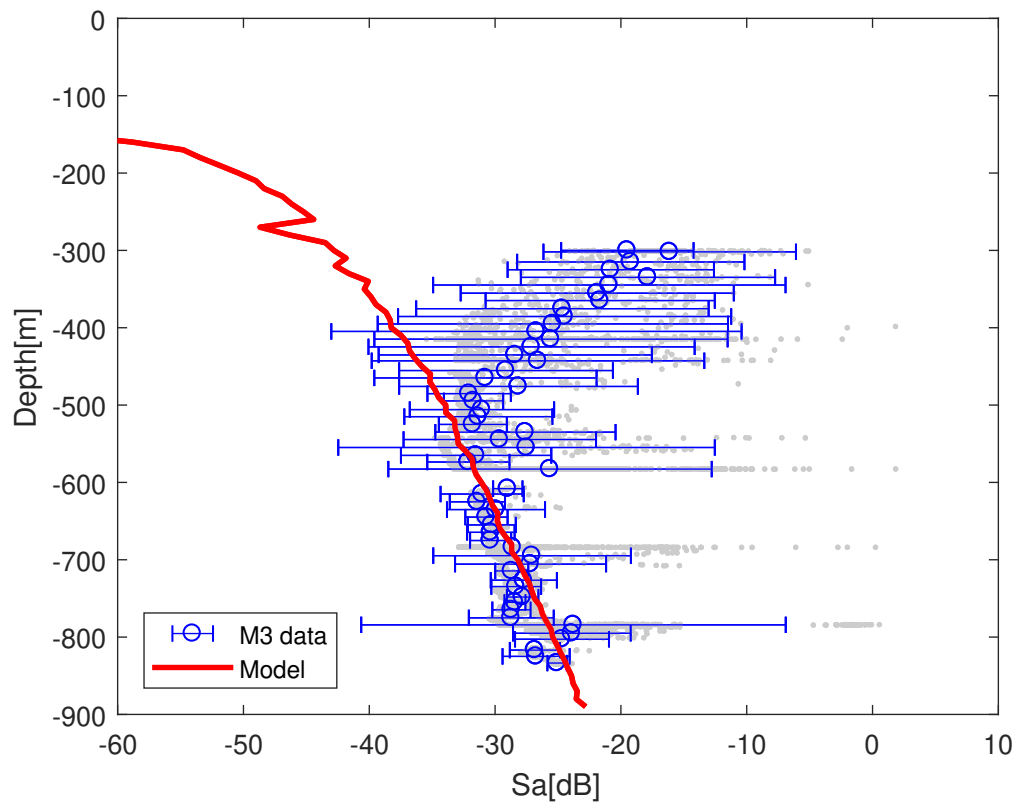


Figure 43: M3 sonar target strength and seep model prediction for GISR G07 Dive H1352 at MC118.

made during the GISR cruises, and were done as we were learning how to properly use the M3 for quantitative observation. Above a depth of about 500 m during this dive, the range from the M3 to the plume was greater than in the previous figures. The M3 was operated with a maximum range of 80 m over this span of the survey, and the plume was often well over 40 m from the ROV. This is well beyond the 10 m range used in the calibration experiments in the OTRC, and we conclude that extrapolating our calibration curve to ranges greater than 40 m appears to break down. Below 500 m water depth, the seep model tracks the observations very well.

One difference that stands out in the simulated target strength in Figure 43 compared to the previous figures is its smooth, monotonic decrease. This results from the much different initial size distribution observed at MC118 during G07 compared to that at GC600. Bubbles were smaller, closer to spherical in shape, and with a narrower size distribution. Also, the initial water depth and gas composition varied. Taken together, the acoustic pattern becomes quite distinct. Hence, not all seep flares will have acoustic signals that appear the same in shape or magnitude.

## 5.2 Application of seep model to GISR EM 302 data

The work for this aspect of the project was recently published in Wang et al. (2020), and the pre-publication version of the article is freely available through the DOE Office of Scientific and Technical Information (OSTI) at <http://www.osti.gov>. We briefly summarize the methods and key results here.

As already introduced in Section 4.5, haul-mounted acoustic multibeam can also be used to visualize vertical profiles of natural seep bubble flares. Images of all of the seeps surveyed during the GISR cruises are provided in Appendix E. In Section 4.5, above, we validated the seep model by comparing the predicted rise height of bubbles to the rise heights observed in the multibeam data. An important conclusion of that work was that bubbles become acoustically transparent at sizes of about 1 mm in the acoustic beams of long-range multibeam sonars (e.g., 18 kHz to 30 kHz instruments). As a result, accurate seep models should predict bubbles rising higher in the water column than observed in the multibeam data. Our analysis above showed that it is only the largest bubbles originating at the sea floor that rise beyond the observational range of these multibeam echosounders, and the single bubble model of TAMOC as adapted here validated well to both the GISR data and literature data for rise height.

In this section, we compare the acoustic properties of the bubble flare throughout its trajectory with those observed by the EM 302. As we report above, a calibration from the manufacturer gives specified target strength in each sample volume of the acoustic beam. Figure 44 shows the procedure we used to extract this quantitative data and to compare the seep model predictions

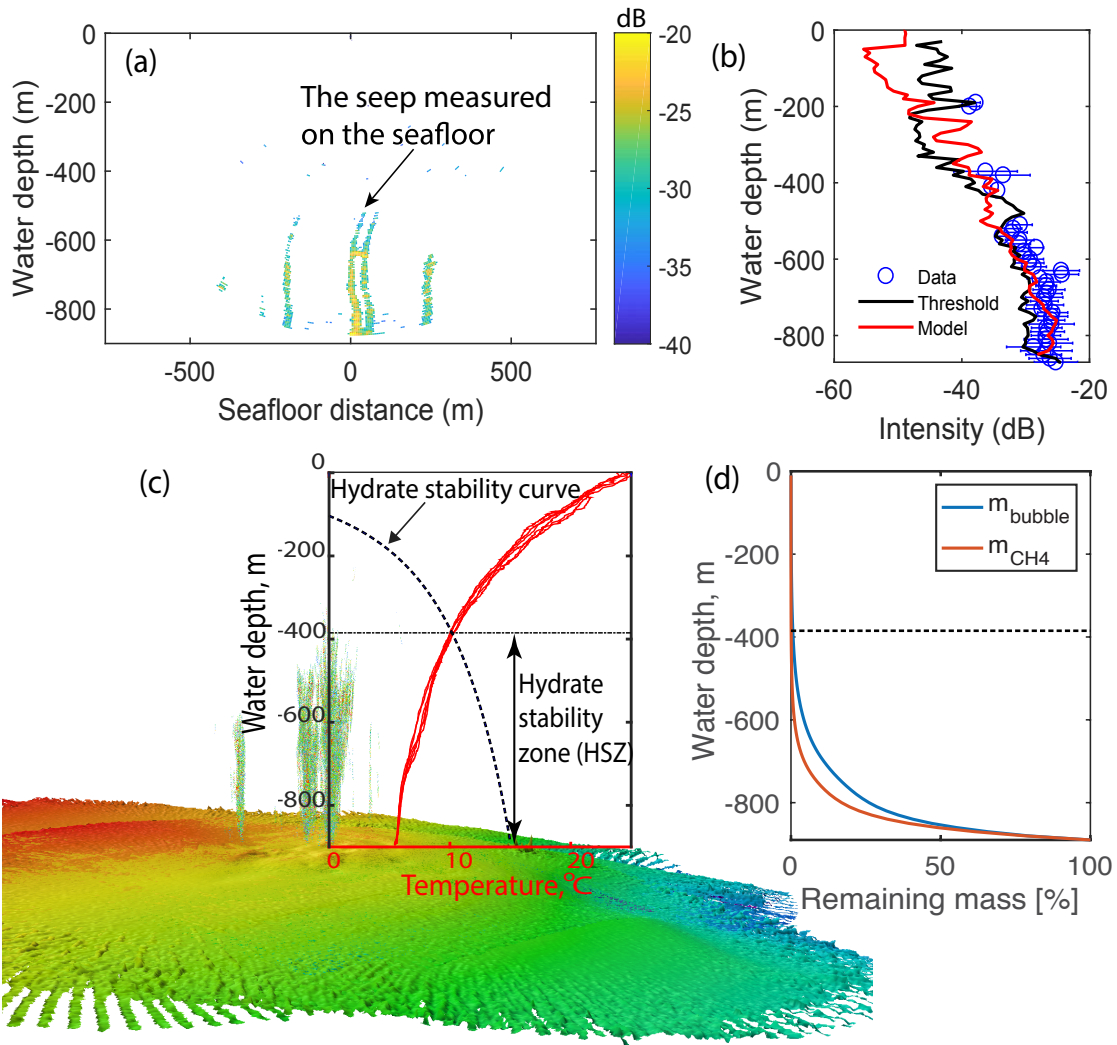


Figure 44: Comparison between the measured and modeled acoustic data from the EM 302 multi-beam sonar: (a) acoustic anomaly in the watercolumn measured by the EM 302 after dive H1403 (the color bar shows the backscatter intensity, dB); (b) comparison of the measured backscatter intensity from the EM 302 (blue circles) and the modeled target strength (red line, offset by  $-17$  dB); the solid black line reports the acoustic background used as a threshold to identify the EM 302 watercolumn anomalies of the bubble flare; (c) the measured acoustic anomalies in the watercolumn by the EM 302 in the context of the surrounding bathymetry; the measured temperature profiles and the calculated hydrate stability curve are superposed in subplot (c), showing the Hydrate Stability Zone (HSZ) from the seafloor to 385 m water depth. (d) the percentage of remaining mass of released natural gas and methane as a function of water depth computed by the model. The horizontal dashed line shows the the hydrate stability line, where the remaining mass of total gas is 0.6%, and the remaining mass of methane is 0.1%.

with the results. This example is for observations at MC118 during the G08 GISR cruise in 2015.

Figure 44(a) shows the backscatter intensity measured by the EM 302 in the water column during a transect over the seep flare at Woolsey mound. There were multiple seeps in the area. We have also removed some background noise to help clearly visualize the seep flares. We extracted the data only for the seep we surveyed (marked in the figure) and integrated the target strength across the plume for each vertical slice in the measured data. We also computed the average target strength at each depth, and considered this to be the upper-bound of the background noise.

In Figure 44(b), we show the laterally-averaged EM 302 data as the blue symbols. The solid black line shows the extracted background noise, and the error bars show the range of measured values for several pings. The flare is observed nearly continuously from the seafloor to a depth of about 500 m, where the signal drops out. The flare is picked back up at about 400 m depth and again at 200 m depth.

Figure 44(c) shows all of the acoustic transects together with the observed bathymetry. In this figure, we also show the observed temperature profile in the water column at the hydrate stability curve for the gas composition measured at the source. The hydrate stability zone (HSZ) lies below 400 m depth and encompasses most of the flare observations made by the EM 302. Because the flares tend to disappear near the top of the HSZ, it has often been assumed that the bubbles rapidly dissolve as hydrates dissociate. As we will explain in the following, this is not the case.

We also plot the predicted acoustic target strength of the plume using the seep model adapted here as the red line in Figure 44(b). During the G08 cruise, gas was seeping from the top of Woolsey Mound so that the ROV could observe gas bubbles at the seafloor. Hence, we initialize the model with fresh bubbles, and we use clean-bubble mass transfer coefficients with the measured gas bubble sizes at the seafloor in the model. The model transitions to dirty-bubble mass transfer coefficients after the transition time given by Equation (11). No other accommodations are made in the model to account for hydrates, and the random displacement model with the diffusivity reported above was used to predict the bubble spreading.

Although the EM 302 gives a quantitative target strength, it is a relative and not an absolute value. In Figure 44(b), we have shifted the model predictions by -17 dB to match the EM 302 data at the source. Overall, the model tracks closely with the measured data. In the regions where the measured data drop out (e.g., between 500 m and 400 m depth), the model also predicts that the plume integrated target strength is below the background noise (black line) over that interval. The few points observed higher in the water column (e.g., near 200 m depth) also appear to coincide with spikes in the plume acoustic signal resulting from bubbles passing through their resonant bubble size in the acoustic path of the EM 302. Hence, these data are a strong validation that the

processes captured in the single bubble model of TAMOC as adapted through the studies above predict well the dynamics of natural seep bubble flares in the oceans.

Figure 44(d) shows the predicted mass flux of bubbles and of methane as a function of height above the leak source. From this curve, we demonstrate that no excess dissolution occurs as the bubbles reach the top of the HSZ. Instead, over 99.9% of the methane released from this seep dissolves into the water within the HSZ. The top of the flare instead coincides with the location where the largest bubbles released from the source become small enough that they are acoustically transparent relative to the ocean background noise. These bubbles continue to rise toward the ocean surface, carrying mostly dissolved atmospheric gases stripped from the ocean water column. Occasionally, some of these bubbles pass through a resonant bubble size, leaving markers of the bubble flare in the acoustic data above 400 m depth. This is also corroborated by our model. Overall, our conclusion is that the seep model adapted here and validated to the HPWT data and diverse field measurements performs well and predicts the dissolution dynamics of natural seep bubbles. These results match acoustic measurements and predict the bulk of released methane to dissolve into the ocean water column within the HSZ for seep originating near 1000 m depth, as studied here.

## 6 Summary and Conclusions

In this project, we have used laboratory data from the NETL HPWT and field data from the GISR field experiments and from the literature to adapt the single bubble model of TAMOC to predict the dynamics of natural gas bubble flares in the oceans. The HPWT data provided observations of shrinkage rate for methane and natural gas bubbles in RO and seawater for a range of pressures. Most experiments were within the hydrate stability zone, and some had hydrate skins on the bubbles. We used these data to relate empirical mass transfer coefficients and a Ranz-Marshall type dissolution model to the observed bubble shrinkage rates. The high-speed images captured in some experiments made it possible to detect hydrate motion on the bubble-water interface, and the high-resolution images in all experiments shows the details of the bubble-water and hydrate-water structures. Using these calibrated mass transfer coefficients, we further validated a numerical seep model to the HPWT observations.

We utilized field observations to further adapt and validate our natural seep model. From the literature and limited observations during the GISR cruises, we extracted transition time data for bubbles to switch from clean-bubble mass transfer coefficients to those for dirty bubbles. We correlated these times with the initial bubble size and hydrate sub-cooling, creating a model that

could adapt to different field conditions. We validated our mass transfer coefficients gleaned from the HPWT data and hydrate transition time by comparing predicted bubble rise heights in natural seep plumes to observations from acoustic multibeam data.

From the model-data comparison of the validation exercises, we quantified the seep bubble performance. For predicting bubble shrinkage in the HPWT data, the model has a mean 10% relative percentage error for the bubble size at the end of an experiment, with a standard deviation of 8%. This accuracy holds over experiments in RO water and seawater, for methane and natural gas, and for cases with and without a hydrate shell. Similarly, when applied to the field, the natural seep model predicts the rise height of bubbles in the ocean water column to an accuracy of 5% to 10% when comparing to observations from haul-mounted acoustic multibeam data. These errors are low, and the wide range of conditions tested in the validation cases gives confidence for applying to model to diverse seep sites in the world oceans.

Using the validated seep model, we further investigated quantitative information in the GISR multibeam data. Using the forward-looking M3 sonar mounted on the ROV, we could measure the spreading rate of bubbles due to random motions as they rise through the ocean water column. We calibrated a random displacement model using our natural seep bubble model to determine an effective diffusivity that explains the observed bubble spreading. We also coupled the model output with an acoustic model to predict the cross-sectionally integrated plume target strength under different acoustic forcing. After calibrating our acoustic tools, we compared predictions of this target strength from the seep model with measurements from the M3 and from the haul-mounted EM 302 multibeam. The model and observations tracked each other well, and predictions of the models helped to explain apparent anomalies in the acoustic data, such as temporary drop out of the bubble flare signal.

Through all of these activities, we have developed a reliable natural seep model and identified several important conclusions, itemized as follows:

- Bubble shrinkage rate in the NETL HPWT is slightly faster than mass transfer for bubbles in a quiescent ambient. This is a result of turbulence in the pipe flow entering the HPWT test section. We compared empirical mass transfer coefficients for dirty bubbles to observations of bubble shrinkage rate in the HPWT and determined that these can match when using is a mass transfer amplification factor of about  $\alpha = 1.9$ . There is modest variability of  $\alpha$ , with the 95% confidence interval spanning 1.4 to 3.0.
- The mass transfer model for bubbles depends on a mass transfer coefficient and the chemical potential at the bubble-water interface, given by the difference between the interface con-

centration  $C_s$  and the ambient concentration of dissolved gas  $C_a$ . For experiments with no hydrate shell or with hydrates skins either at a subcooling of  $\Delta T_{hyd} < 11^\circ\text{C}$  or with pressure decreasing as a bubble rises through the water column, free gas inside the bubble appears to be the dominant phase involved in dissolution. Hence, for these cases, we use  $C_s$  equal to the saturation concentration of gas in water and dirty bubble mass transfer coefficients. For a few experiments at constant pressure and with  $\Delta T_{hyd} > 11^\circ\text{C}$ , hydrate becomes the dominant dissolving phase; we set  $C_s$  equal to the hydrate solubility in water and continue to apply dirty bubble mass transfer coefficients.

- When a bubble is released into an environment that is stable for hydrate formation, hydrate does not always form, and when it does form, hydrate growth takes time. We studied hydrate transition times from data in the literature and developed a correlation that depends on the initial bubble surface area and the hydrate sub-cooling. Clean-bubble mass transfer coefficients prevail before this transition time, after which dirty-bubble mass transfer coefficients should be used. The hydrate transition time is given by Equation (11).
- To validate the natural seep model to the height of rise of seep flares observed in the field by multibeam echosounders, we found that one must account for the acoustic transparency of bubbles as they approach the top of the observed flare. For bubble sizes larger than their resonant size in an acoustic beam, they continue to vibrate and emit modest, measurable noise levels. For smaller sizes, their noise backscatter reduces quickly, and they rapidly become indistinguishable from background noise. For typical long-range echosounds, the resonant size is on the order of 1 mm diameter. Natural seep models predict these bubbles to continue to rise significantly in the ocean water column. We found that good agreement between the model and acoustic observation can be achieved when the model tracks the largest bubbles emitted at the seafloor and reports the flare rise height as the height that these bubbles would disappear from the acoustic image.
- Using the M3 data mounted in a forward-looking configuration on the ROV, we achieved two new results. First, we applied methods similar to Weber et al. (2014) and showed that the cross-sectional multibeam data can be related to gas flow rate if the bubble size distribution at any height can be predicted by the natural seep model. Second, we used the instantaneous acoustic images to quantify the spreading rate of gas bubbles as they rise in natural seeps from the seafloor. Using the numerical model and a random displacement algorithm we could relate these observed spreading rates to an effective diffusivity for a diffusion process. This diffusivity agrees well with an empirical value related to the bubble wobbling motion and is

about 10 times greater than that of the ambient ocean turbulence. Because bubble spread follows a diffusion process, plume entrainment is negligible, and plume-induced upwelling can be ignored. Therefore, bubble trajectories from natural seeps can be modeled using empirical relationships for rise velocity in a quiescent ambient and standard random displacement models using diffusivities extracted from the bubble wobble excursion.

- Using our validated natural seep model coupled to a random displacement algorithm, we could predict the cross-sectionally averaged target strength of the plume within the beams of the M3 and EM 302. After calibrating the M3 and EM 302, we find good agreement between the observed and predicted target strengths. This further validates the single bubble model approach in TAMOC. Comparing the predicted and observed target strength also highlights the fact that the acoustic target strength varies significantly with height, periodically becoming loud as bubbles shrink through their resonant size. Occasionally, the seep flare is also quiet, passing below the ambient noise, causing the flare to temporarily disappear from the acoustic image of the multibeam. Together, this model-data comparison gives good confidence to our developed seep model.
- To achieve this good model performance, we implement dirty-bubble mass transfer coefficients in the presence of hydrate and assume that free gas inside the bubbles is the dominant dissolving phase. As a result, nothing changes in the model as bubble pass through the top of the hydrate stability zone. As hydrates dissociate, the bubbles have been in the ocean water column for a significant time, and mass transfer coefficients would not relax back to clean bubble rates. The fact that bubble flares tend to disappear near the top of the HSZ is more a coincidence of the bubble sizes that become transparent in the acoustic multibeam and not a mechanistic observation. Moreover, our model predicts for these seeps originating at about 1000 m depth in the Gulf of Mexico that over 99% of the released methane dissolves into the ocean water column within the HSZ. The bubbles that continue to rise to shallower depth are primarily comprised of atmospheric gases stripped from the ocean water column. Hence, as shown rigorously by Ruppel and Kessler (2017), natural seeps within the HSZ contribute methane to the deep ocean, and do not pose a major source of methane to the atmosphere.

## 7 Impact Statement

In this project, we have synthesized laboratory observations of individual hydrocarbon bubbles in the NETL HPWT experiments and field observations from the GISR cruises to adapt the Texas A&M Oilspill Calculator (TAMOC) to simulate bubbles rising from natural seeps on the continental

margins in the oceans. From the NETL HPWT data, we showed that mass transfer rates agree well with theoretical models when using dirty-bubble mass transfer coefficients and assuming that free gas is the dominant dissolving phase. This holds true for bubbles with and without a hydrate shell as long as the sub-cooling is less than 11°C or the pressure is reducing as bubbles rise. From the GISR field data, we validated acoustic models of natural gas bubbles in the ocean water column and the mass transfer rates inferred from the NETL experiments. In both the laboratory and field datasets, model errors for bubble size and flare rise height predictions are in the range of 10% absolute relative percentage error. This adapted seep model now predicts well the gas dissolution at a wide range of seep sites – this was not possible using other available models before this project. A synthesis of this work was recently published in the paper by (Wang et al., 2020) and more broadly in this Final Scientific/Technical Report.

Our validated seep model within TAMOC has also been used by others. Römer et al. (2019) presents an application in the field that successfully simulates natural seep bubble flares in acoustic multibeam data using the seep model developed here. The TAMOC bubble models are also being used by the Lawrence Berkeley National Laboratory, Curtis Oldenburg, to simulate leakage of carbon dioxide from subsea sequestration reservoirs (Oldenburg and Pan, 2020). These and an on-going number of studies substantiate the advances made for this model through this project.

## Acknowledgement

This work was supported by a grant from the U.S. Department of Energy, National Energy Technology Laboratory, Methane Hydrates Program through award number DE-FE0028895. The views and opinions of authors expressed herein do not necessarily state or reflect those of the United States Government or any agency thereof.

## References

- Bryant, L. D., Gantzer, P. A. and Little, J. C. (2011), ‘Increased sediment oxygen uptake caused by oxygenation-induced hypolimnetic mixing’, *Water Research* **45**, 3692–3703.
- Clift, R., Grace, J. R. and Weber, M. E. (1978), *Bubbles, Drops, and Particles*, Academic Press, New York, NY.
- Danesh, A. (1998), *PVT and Phase Behavior of Petroleum Reservoir Fluids*, Elsevier, Amsterdam, the Netherlands.

- Dissanayake, A. L., Gros, J. and Socolofsky, S. A. (2018), ‘Integral models for bubble, droplet, and multiphase plume dynamics in stratification and crossflow’, *Environmental Fluid Mechanics* **18**(5), 1167–1202.
- Dragonette, L. R., Numrich, S. K. and Frank, L. J. (1981), ‘Calibration technique for acoustic scattering measurements’, *The Journal of the Acoustical Society of America* **69**.
- Foote, K. G. and MacLennan, D. N. (1984), ‘Comparison of copper and tungsten carbide calibration spheres’, *The Journal of the Acoustical Society of America* **75**, 612–616.
- Gill, A. (1982), *Ocean-Atmosphere Dynamics*, Academic Press, New York, NY.
- Gros, J., Reddy, C. M., Nelson, R. K., Socolofsky, S. A. and Arey, J. S. (2016), ‘Simulating gasliquidwater partitioning and fluid properties of petroleum under pressure: Implications for deep-sea blowouts’, *Environmental Science Technology* **50**(14), 7397–7408.
- Gros, J., Socolofsky, S. A., Dissanayake, A. L., Jun, I., Zhao, L., Boufadel, M. C., Reddy, C. M. and Arey, J. S. (2017), ‘Petroleum dynamics in the sea and influence of subsea dispersant injection during deepwater horizon’, *Proceedings of the National Academy of Sciences* .
- Hayduk, W. and Laudie, H. (1974), ‘Prediction of diffusion coefficients for nonelectrolytes in dilute aqueous solutions’, *American Institute of Chemical Engineers Journal* **20**(3), 611–615.
- Jerram, K., Weber, T. C. and Beaudoin, J. (2015), ‘Split-beam echo sounder observations of natural methane seep variability in the northern gulf of mexico’, *Geochemistry Geophysics Geosystems* **16**(3), 736–750.
- Johnson, A. I., Besik, F. and Hamielec, A. E. (1969), ‘Mass transfer from a single rising bubble’, *Canadian Journal of Chemical Engineering* **47**(6), 559–564.
- Jun, I. (2018), A numerical model for hydrocarbon bubbles from natural seeps within hydrate stability zone, PhD thesis, Texas A&M University.
- King, M. B. (1969), *Phase Equilibrium in Mixtures*, International Series of Monographs in Chemical Engineering, Oxford, New York, Pergamon Press.
- Kongsberg (2020), ‘M3 sonar reference manual’.
- Levine, J., Haljasmaa, I., Lynn, R., Shaffer, F. and Warzinski, R. P. (2015), Detection of hydrates on gas bubbles during a subsea oil/gas leak, Report, NETL-TRS-6-2015; EPA Technical Report Series; U.S. Department of Energy, National Energy Technology Laboratory: Pittsburgh, PA.

- Li, G., Wang, B., Wu, H. and DiMarco, S. F. (2020), ‘Impact of bubble size on the integral characteristics of bubble plumes in quiescent and unstratified water’, *International Journal of Multiphase Flow* **125**, 103230.
- Little, J. C. and McGinnis, D. F. (2001), ‘Hypolimnetic oxygenation: Predicting performance using a discrete-bubble model’, *Water Science and Technology : Water Supply* **1**(4), 185–191.
- Lurton, X. (2002), *An Introduction to Underwater Acoustics: Principles and Applications*, Springer-Verlag Berlin Heidelberg.
- Lurton, X. (2016), ‘Modelling of the sound field radiated by multibeam echosounders for acoustical impact assessment’, *Applied Acoustics* **101**, 201 – 221.
- McCain, W. D. (1990), *The Properties of Petroleum Fluids*, PennWell Books, Tulsa, OK.
- McGinnis, D. F., Lorke, A., Wüest, A., Stöckli, A. and Little, J. C. (2004), ‘Interaction between a bubble plume and the near field in a stratified lake’, *Water Resources Research* **40**(10), W102061–W1020611.
- McGinnis, D. F., Wüest, D. F., Greinert, D. F., Artemov, D. F. and Beaubien, D. F. (2006), ‘Fate of rising methane bubbles in stratified waters: How much methane reaches the atmosphere?’, *Journal of Geophysical Research: Oceans* **111**(9), C09007–C09017.
- Medwin, H. and Clay, C. S. (1998), *Fundamentals of Acoustical Oceanography*, Academic Press, Boston, MA.
- Michelsen, M. L. and Mollerup, J. (1986), ‘Partial derivatives of thermodynamic properties’, *AIChE Journal* **32**(8), 1389–1392.
- Oldenburg, C. M. and Pan, L. (2020), ‘Major co2 blowouts from offshore wells are strongly attenuated in water deeper than 50m’, *Greenhouse Gases: Science and Technology* **10**(1), 15–31.
- Pedersen, K. S., Christensen, P. L. and Shaikh, J. A. (2015), *Phase Behavior of Petroleum Reservoir Fluids*, 2nd edition edn, CRC Press, Taylor & Francis Group, New York.
- Peng, D.-Y. and Robinson, D. B. (1976), ‘A new two-constant equation of state’, *Industrial & Engineering Chemistry Fundamentals* **15**(1), 59–64.
- Poling, B. E., Prausnitz, J. M. and O’Connell, J. P. (2001), *The Properties of Gases and Liquids*, McGraw-Hill, New York, NY.

- Rehder, G., Leifer, I., Brewer, P. G., Friederich, G. and Peltzer, E. T. (2009), ‘Controls on methane bubble dissolution inside and outside the hydrate stability field from open ocean field experiments and numerical modeling’, *Marine Chemistry* **114**(1-2), 19–30.
- Robinson, D. B. and Peng, D. Y. (1978), *The Characterization of the Heptanes and Heavier Fractions for the GPA Peng-Robinson Programs*, Research report (Gas Processors Association), Gas Processors Association.
- Römer, M., Hsu, C.-W., Loher, M., MacDonald, I. R., dos Santos Ferreira, C., Pape, T., Mau, S., Bohrmann, G. and Sahling, H. (2019), ‘Amount and fate of gas and oil discharged at 3400 m water depth from a natural seep site in the southern gulf of mexico’, *Frontiers in Marine Science* **6**(700).
- Römer, M., Sahling, H., Pape, T., Bohrmann, G. and Spieß, V. (2012), ‘Quantification of gas bubble emissions from submarine hydrocarbon seeps at the Makran continental margin (offshore Pakistan)’, *Journal of Geophysical Research: Oceans* **117**(C10), C10015.
- Ruppel, C. D. and Kessler, J. D. (2017), ‘The interaction of climate change and methane hydrates’, *Reviews of Geophysics* **55**(1), 126–168.  
**URL:** [iGo to ISI://WOS:000399361000004](https://doi.org/10.1029/2017RG000564)
- Schwarzenbach, R., Gschwend, P. M. and Imboden, D. M. (2003), *Environmental Organic Chemistry*, Hoboken, NJ: Wiley.
- Sharqawy, M. H., V., J. H. L. and Zubair, S. M. (2010), ‘Thermophysical properties of seawater: a review of existing correlations and data’, *Desalination and Water Treatment* **16**, 354–380.
- Singleton, V. L. and Little, J. C. (2006), ‘Designing hypolimnetic aeration and oxygenation systems - a review’, *Environmental Science & Technology* **40**(24), 7512–7520.
- Socolofsky, S. A. and Adams, E. E. (2002), ‘Multi-phase plumes in uniform and stratified crossflow’, *J. Hydr. Res.* **40**(6), 661–672.
- Wang, B., Jun, I., Socolofsky, S. A., DiMarco, S. F. and Kessler, J. D. (2020), ‘Dynamics of gas bubbles from a submarine hydrocarbon seep within the hydrate stability zone’, *Geophysical Research Letters* **47**(18), e2020GL089256.
- Wang, B., Lai, C. C. K. and Socolofsky, S. A. (2019), ‘Mean velocity, spreading and entrainment characteristics of weak bubble plumes in unstratified and stationary water’, *Journal of Fluid Mechanics* **874**, 102–130.

- Wang, B. and Socolofsky, S. A. (2015a), ‘A deep-sea, high-speed, stereoscopic imaging system for in situ measurement of natural seep bubble and droplet characteristics’, *Deep Sea Research Part I: Oceanographic Research Papers* **104**, 134–148.
- Wang, B. and Socolofsky, S. A. (2015b), ‘On the bubble rise velocity of a continually released bubble chain in still water and with crossflow’, *Physics of Fluids* **27**, 103301.
- Wang, B., Socolofsky, S. A., Breier, J. A. and Seewald, J. S. (2016), ‘Observations of bubbles in natural seep flares at mc 118 and gc 600 using in situ quantitative imaging’, *Journal of Geophysical Research: Oceans* **121**(4), 2203–2230.
- Warzinski, R. P., Lynn, R., Haljasmaa, I., Leifer, I., Shaffer, F., Anderson, B. J. and Levine, J. S. (2014), ‘Dynamic morphology of gas hydrate on a methane bubble in water: Observations and new insights for hydrate film models’, *Geophysical Research Letters* **41**(19), 2014GL061665.  
**URL:** <http://dx.doi.org/10.1002/2014GL061665>
- Warzinski, R. P., Shaffer, F., Lynn, R., Haljasmaa, I., Schellhaas, M., Anderson, B. J., Velaga, S., Leifer, I. and Levine, J. (2014), The role of gas hydrates during the release and transport of well fluids in the deep ocean, Report, DOI/BSEE Contract E12PG00051/M11PPG00053, Final Report, U.S. Department of Energy, National Energy Technology Laboratory: Pittsburgh, PA.
- Weber, T. C., De Robertis, A., Greenaway, S. F., Smith, S., Mayer, L. and Rice, G. (2012), ‘Estimating oil concentration and flow rate with calibrated vessel-mounted acoustic echo sounders’, *Proceedings of the National Academy of Sciences of the United States of America* **109**(50), 20240–20245.
- Weber, T. C., Mayer, L., Jerram, K., Beaudoin, J., Rzhanov, Y. and Lovalvo, D. (2014), ‘Acoustic estimates of methane gas flux from the seabed in a 6000 km<sup>2</sup> region in the northern gulf of mexico’, *Geochemistry Geophysics Geosystems* **15**(5), 1911–1925.
- Weidner, E., Weber, T., Mayer, L., Jakobsson, M., Chernykh, D. and Semiletov, I. (2019), ‘A wideband acoustic method for direct assessment of bubble-mediated methane flux’, *Continental Shelf Research* **173**, 104 – 115.  
**URL:** <http://www.sciencedirect.com/science/article/pii/S0278434318303649>
- Wüest, A., Brooks, N. H. and Imboden, D. M. (1992), ‘Bubble plume modeling for lake restoration’, *Water Resour. Res.* **28**(12), 3235–3250.

## **A Summary of Project Outcomes by Task and Subtask**

The main body of this technical report is organized by project Task, and reports the main scientific and technical results within each task following a logical progression of knowledge discovery.

This appendix includes a high-level summary of the important project outcomes organized by Task and Sub-task. This summary was included in the final quarterly Research Performance Progress Report. It is repeated here for completeness. Please refer to Figure 1 for the project timeline and a graphical depiction of each Task, Subtask, Deliverable and Milestone.

### **A.1 Task 1.0: Project Management Planning**

The Project Management Plan was completed during the first quarter of Phase 1 and accepted in final form as of October 28, 2016.

### **A.2 Task 2.0: Analyze NETL Water Tunnel Data**

In this project, we have analyzed the comprehensive data set of High Pressure Water Tunnel (HPWT) data collected by the National Energy Technology Laboratory (NETL). To do this, we have transferred a complete copy of all raw data (primarily image files and time history data of pressure and temperature in the HPWT during each experiment) to Texas A&M University and have installed this data on a secure internal server. Data transfer was completed on March 24, 2017, and achieved Milestone 1 for the project (Obtain NETL HPWT Data). Task 2 was completed as of June 30, 2018. The sections below summarize the key results obtained for each of the Subtasks of this Task.

#### **Subtask 2.1 - Evaluate Hydrate Formation Time**

This subtask was completed as of September 30, 2017, and all of the post-processed data was submitted with the Technical Report for Decision Point 1 (see Appendix B). In this task, we identified the moment that hydrate skin coverage was completed for each bubble in the experiments as well as for key moments when the hydrate dynamics changed. For a complete description of the data analysis for this subtask and the post-processed results, see Appendix B and the Digital Appendix B.

#### **Subtask 2.2 - Track Hydrate Crystals on Bubble Interface**

This subtask was completed as of December 31, 2017, and a complete analysis of the results with conclusions was submitted with the first-quarter progress report of FY2018 (see Appendix C). For this task, we analyzed all of the high-speed camera data for gas bubbles with hydrate shells to

track the motion of hydrate plates when the hydrate coverage was not 100%. We found two main types of behavior. First, when hydrate plates are large and their spacing is non-uniform, the plates are observed to translate across the leading edge of the bubbles. The mean speeds of this hydrate shell movement was 10 cm/s, with peak speeds close to the rise velocity of bubbles (20 cm/s). Second, during hydrate dissociation, when many, small hydrate crystals cover the bubble surface in a quasi-uniform distribution, the hydrate particles are not observed to translate over the surface of the bubble. Instead, they remain knitted together, and the boundary condition at the bubble/water interface appears to be no-slip.

Based on these observations, we anticipate that mass transfer rates for the large hydrate shells that move across the leading edge of the bubble will be higher than for dirty bubbles; whereas, we expect the mass transfer rates for hydrate-coated bubbles and cases with small hydrate particles uniformly distributed over the bubble surface to be similar to dirty bubbles or slower. Because the system pressure inside the HPWT was not constant during these events, we evaluate these mass transfer rates in the context of Task 4 as we compare the model results to these data.

### **Subtask 2.3 - Validate Bubble Shrinkage Rates**

This subtask was completed as of April 30, 2018, and is summarized in detail in Section 2 of this report. We adapted our Matlab image analysis program for bubble size evaluation to the NETL HPWT dataset and compared our results for bubble size to those reported by NETL in their report by Levine et al. (2015). Although there were small differences in our computed sizes, these are attributable to different choices in the cut-off and cut-on criteria for identifying the bubble edge and were negligible in comparison to the inherent variability in the data due to bubble motion. This variability is primarily caused by two factors: 1.) rotation of the bubbles when they have non-spherical shape and 2.) changes in the image magnification as the bubbles move toward and away from the camera. Both factors lead to experimental error in the computed bubble sizes. We evaluated this error by analyzing long data sets in sequentially shorter sample periods. Our analysis concluded that bubble shrinkage rates are converged after a minimum of 500 s of sampling, as this is adequate time for the bubble to wander about the whole measurement volume and experience several rotations. These data are used extensively in Task 4 to validate the shrinkage rate predictions of the model to those measured in the HPWT.

### **Progress Toward Milestones**

Milestone 1 (Obtain NETL HPWT Data) was completed on March 24, 2017, and Milestone 2 (Adapt Matlab Code to NETL Data) was completed on September 26, 2017. These Milestones conclude the Milestones associated with Task 2.

### **A.3 Task 3.0: Synthesize GISR Field Data**

The project PIs conducted two research cruises to natural seeps in the Gulf of Mexico under funding to the GISR consortium. These were the G07 cruise in July 2014 to Mississippi Canyon (MC) block 118 and to Green Canyon (GC) block 600 and the G08 cruise in April 2015 to MC 118. Both cruises were on the *E/V Nautilus* and utilized the remotely operated vehicle (ROV) *Hercules*. This project utilizes two main datasets from these cruises: data from our stereoscopic high-speed camera system mounted on the ROV (Wang et al. 2015) and acoustic data collected by an M3 sonar mounted on the ROV and an EM-302 multibeam sonar mounted on the haul of the ship. The image data from the G07 cruise was analyzed previously and reported in (Wang et al., 2016). This project analyzes all of the acoustic data and performs a complete analysis of the image data for the G08 cruise. This task was completed as of December 2017, and the outcomes of each subtask are reported below.

#### **Subtask 3.1 - Bubble Characteristics from High-Speed Camera.**

This subtask was completed as of September 30, 2017, and all of the post-processed data were submitted with the report for Decision Point 1 (see Appendix B). In this task, we have analyzed images from our high-speed, stereoscopic image system to compute bubble size distributions and the rise velocities of individual bubbles. For a complete description of the data analysis for this subtask and the post-processed results, see Appendix B.

#### **Subtask 3.2 - Synchronize Acoustic and Camera Datasets.**

This subtask was completed as of March 31, 2018. Data from the cameras and acoustic measurements have been reported separately. The image data include bubble size distributions and rise velocity, and are reported in the report for Decision Point 1 (see Appendix B). The acoustic data have been analyzed to predict the *in situ* target strength, which is a measure of the acoustic backscatter from the bubbles within each sample volume. This work was reported in the report for Milestone 3 (see Appendix D). The final output of this subtask was a calibration curve relating the observed bubble characteristics to the target strength measured by the M3 and EM 302 multibeam sonars. The calibration curve for the EM 302 and for the M3 is included in Appendix D. These data, along with results of Task 5 (OTRC experiment) were used in Task 6 to evaluate the seep model at the field scale (see Section 5 of this report, above).

#### **Progress Toward Milestone**

Milestone 3 (Develop Matlab Code for EM 302 and M3 Data) was completed on September 29, 2017. This Milestone concludes the Milestones associated with Task 3.

## **Decision Point 1**

The report for Decision Point 1 was completed and submitted as of October 31, 2017. Based on successful completion of the go/no go success criteria for Decision Point 1 outlined in the PMP, we were granted permission to continue into project Phase 2 and begin work on Task 4.

### **A.4 Task 4.0: Refine and Validate Seep Model**

Since the Deepwater Horizon accident, the project PIs have been developing a numerical model to predict the fate of petroleum bubbles and droplets in the ocean water column. This model is called the Texas A&M Oil spill Calculator (TAMOC), and is freely available through <https://github.com/socolofs/tamoc>. This model can compute the dissolution of a natural gas bubble in the ocean water column, and prior to this project, had been applied to study the fate of methane released from natural gas seeps along the continental slope of the Gulf of Mexico. In this project, we applied this numerical model to simulate the experiments in the NETL High-Pressure Water Tunnel (HPWT; see Task 2) and the field observations from the GISR expeditions (see Task 3). These simulations are used to validate our model for the formation time of hydrate skins of natural gas bubbles within the hydrate stability zone of the oceans and our equations for mass transfer from bubbles with and without a hydrate skin. This model is important to predict the distribution of methane in the ocean water column from natural seeps, accidental oil well blowouts, hydrate production, or from gas release caused by anthropogenic or changing climate forcing.

#### **Subtask 4.1 - Validate to NETL Water Tunnel Data.**

This subtask was initially completed as of January 31, 2019, and was revised as of April 30, 2020.

In the NETL HPWT experiments, cameras observed the bubbles over time as they dissolved into the surrounding flow, and these experiments were conducted at different pressure and temperature conditions. Because the pressure and temperature in the HPWT is prescribed by the operator and independent of bubble position (the pressure is controlled by a set of piston pumps and the bubble is held at a constant depth in the water tunnel), we adapted the TAMOC model to allow pressure and temperature to be prescribed functions of time so that we model the exact conditions experienced by a bubble during an experiment. For the model validation, we used the mass transfer coefficients  $\beta$  derived through our work on Task 2 and compared them to empirical mass transfer coefficients using a calibration and verification procedure (see Section 2 of this report), resulting in

the relationship

$$\beta = 1.9\beta_{emp} \tag{29}$$

where  $\beta_{emp}$  are the empirical mass transfer coefficients reported in the literature Clift et al. (1978). Using these values in the TAMOC model, we evaluated the model performance for predictions of bubble size against the equivalent spherical bubble diameters reported by NETL. The model integrated relative percentage error at the end of each validation experiment is 30% or less, with an average of 8% error. This is very low error considering small errors add together over the duration of each validation experiment. See the broader discussion in Section 4 of this report for more details.

#### **Subtask 4.2 - Validate to GISR Field Data.**

This subtask was completed as of January 31, 2019. In the GISR field experiments, three observation platforms were used: *in situ* imaging from the stereoscopic imaging system at discrete points from the sea floor to about 250 m altitude and acoustic backscatter measurements from the EM 302 haul-mounted multibeam sonar and from the M3 multibeam sonar mounted on the ROV. In this Subtask, we validated the TAMOC model predictions at the seeps surveyed during the G07 and G08 GISR expeditions to these measured data. We post-processed the raw camera images and acoustic backscatter to yield three derived datasets for model calibration and validation. These were the bubble size distribution and flow rate (see Appendix B), which served as initial conditions to the model, the lateral spreading of bubbles in the M3 acoustic images (see (Wang et al., 2020)), which provided the lateral turbulent diffusivity used in the model, and the observed height of maximum bubble rise in the EM-302 data (see Appendix E), which is the predicted variable used in model validation. In our validation exercise, we showed that the model could predict the rise heights of all seeps surveyed and those we extracted from the literature with an  $r^2$  value of 0.98, a bias of 41 m absolute height (out of rise heights between 400 m and 1800 m), and an average mean percentage error of the rise height prediction of 4.7 Jun (2018). This performance is quite good and exceeds that of other models that are used in the literature to predict natural seep flares.

#### **Subtask 4.3 - Finalize and Distribute Seep Model.**

This subtask was completed as of January 31, 2019. We provided the source code of the model with the archive of NETL HPWT simulation results. The model is also maintained as publicly available through the Github code sharing website at <https://github.com/socolofs/tamoc>. This concludes the major activity under Task 4.

### **Progress Toward Milestones**

Milestone 4 (Adapt TAMOC model to NETL data) was completed on June 19, 2018. Milestone 5 (Quantify seep model performance) was completed with the quarterly report, submitted in January 31, 2019. Model fit statistics are reported in the main report, Section 4, above. These Milestones conclude those associated with Task 4.

## **Decision Point 2**

The report for Decision Point 2 was completed and submitted as of May 31, 2018. Based on successful completion of the go/no go success criteria for Decision Point 2 outlined in the PMP, we were granted permission to continue into Task 5 (OTRC Experiment).

### **A.5 Task 5.0: Conduct No-Hydrate M3 Calibration Experiment in OTRC**

The OTRC experiment was completed as of March 21, 2019. In this experiment, we simulated two different natural seep vents at five different flow rates in the 16.8 m deep, central pit of the OTRC's directional wave basin. We measured the bubble size distribution from an *in situ* CCD camera, water velocity in the plume using a Vectrino II acoustic Doppler velocimeter (ADV), and observed the plumes using an M3 multibeam sonar. Using a tungsten carbide ball bearing, we calibrated the M3 acoustic response, and from the measurements of these simulated natural seeps, we further validated our acoustic models for bubble dynamics in the M3 images. The results of these analyses are reported in more detail in Section 5 of this report, above.

### **Progress Toward Milestone**

Full details of the OTRC experiment set up and results were provided in the report for Milestone 6 (OTRC experiment report, submitted March 21, 2019; see Appendix F attached to this report). The validation of the acoustic models, which relies in part on the data collected in this experiment, were also reported in the report for Milestone 7 (Quantify, performance of acoustic models; associated with Task 6, below. See Section 5 of this report). These Milestones conclude those associated with Task 5.

### **A.6 Task 6.0: Apply Seep Model to GISR Multibeam Echosounder Data**

In this Task, we use the seep model validated in Task 4 together with the acoustic data analyzed in Task 2 and refined in Task 5 to evaluate the characteristics of the natural seeps at MC 118 and GC 600. This includes an evaluation of the acoustic signature of hydrate shells that may be present in the M3 acoustic cross-sectional data obtained by the ROV and the water column trajectory and flow rate that may be extractable from the haul-mounted EM 302. Together, these activities

explore the role of hydrate shells on the fate of methane from natural seeps and predict the vertical distribution of methane in the water column originating from these seep sources.

### **Subtask 6.1 - Analyze M3 Data to Characterize Hydrate Shells.**

This subtask was completed as of September 30, 2020. This subtask involved two main efforts. First, we used the acoustic data collected during Task 5 in the OTRC experiments (see Appendix F to calibrate the M3 acoustic multibeam for seep-like bubble flares and evaluated our ability to use the M3 data to estimate gas flow rate. Second, we applied a similar method to the M3 data from the GISR cruises. In the field, we likewise have camera images reporting gas bubble sizes and volume flow rate together with M3 acoustic multibeam data (see Appendix D). One difficulty in the field is that the seep bubbles spread out with height, especially in the downstream direction, so that it is not possible to include all of the gas bubbles within the field-of-view of the camera. We solved this problem by recording camera data during the GISR cruises in the locations where the acoustic return in the M3 data was the highest.

We have used these field data to create a similar calibration for the M3 acoustic response as obtained in the OTRC experiments. Our original purpose in this subtask was to compare the calibration curves for the laboratory and the field and to determine whether differences can be attributed to the effects of hydrate shells. Unfortunately, the measured data and calibration curves are noisy enough that no statistically-significant differences can be seen between the field and laboratory calibrations (see Section 5 of this report for more details). Also, using a single acoustic wavelength limits the quantitative information that can be collected on bubble size from the M3. Instead, we utilize the field-scale results to estimate gas flow rate at each measurement height and compare this to the seep model predictions. The main results of these analyses are published in the recent paper by (Wang et al., 2020).

### **Subtask 6.2 - Analyze EM 302 Data for Bubble Concentration.**

This subtask was completed as of September 30, 2020, and focused on combining results from the EM 302 multibeam with predictions from the seep model to understand the dynamics of natural seep bubble columns. The main results of this subtask were recently published in (Wang et al., 2020).

The shipboard, hull-mounted EM 302 collected vertical profiles of watercolumn acoustic anomalies for survey transects that crossed the seep sites visited during the GISR cruises. This data was post-processed to remove background noise and to isolate the target strength of bubbles occurring in the insonified fan of the multibeam. At the same time, ROV surveys measured the initial gas

bubble size distribution and flow rate at the seafloor. These initial conditions were used in the seep model to predict the evolution of the gas bubbles through the water column. Acoustic models of the gas bubbles developed in Task 2 were then applied to the model results to predict the flare target strength as a function of height above the seafloor. By comparing the EM 302 observed target strength with that predicted by the seep model, we could validate the seep model predictions and better understand some of the anomalies in the EM 302 data. Figure 45 shows a typical comparison between the seep bubble model and the EM 302 observations.

We ran the seep model using mass transfer rates validated through our work on Task 4. There, we confirmed that dirty bubble mass transfer rates are appropriate for gas bubbles with a hydrate shell when they rise through the ocean water column and the pressure reduces steadily with height above the bottom. We also applied the hydrate formation time estimate that we derived previously using data reported in (Rehder et al., 2009). Because the model predictions for bubble acoustic target strength generally agree well with observations from the EM 302, this work helped to validate our seep model to a wide range of observations in the GISR dataset.

The seep model acoustic predictions also help to understand some of the traits in the EM 302 observations. It is apparent in the EM 302 data that the gas bubble flares do not always appear continuous in the water column from the seafloor to a maximum height of rise. Instead, there can be bright spots in the acoustic images and regions where the bubble column appears to vanish relative to background and then to appear again at a shallower depth (see isolated blue circles in subplot b of Figure 45). We observed the same intermittency of the target strength in the seep model results (see variability of red prediction line with height in subplot b of Figure 45). This occurs due to the fact that bubbles of a certain small size (about 1.5 mm) resonate at the acoustic wave length of the EM 302. Larger bubbles are visible, but less loud; smaller bubbles rapidly become acoustically transparent. A wide bubble size distribution, with mean close to 5 mm, was emitted from the seafloor. Bubbles of different initial sizes reach the resonant 1.5 mm diameter at different heights in the water column. Especially higher in the water column, it is possible for the few, larger bubbles remaining in the bubble flare to become quieter than background (the flare disappears), only to suddenly become loud again as these bubbles shrink through the resonant size. The agreement between these observations and model predictions gives us greater confidence in the EM 302 observations and a better understanding of the real dynamics of natural seep bubble columns.

### **Progress Toward Milestone**

Milestone 7 (Quantify performance of acoustic models) was completed as of April 30, 2019. That

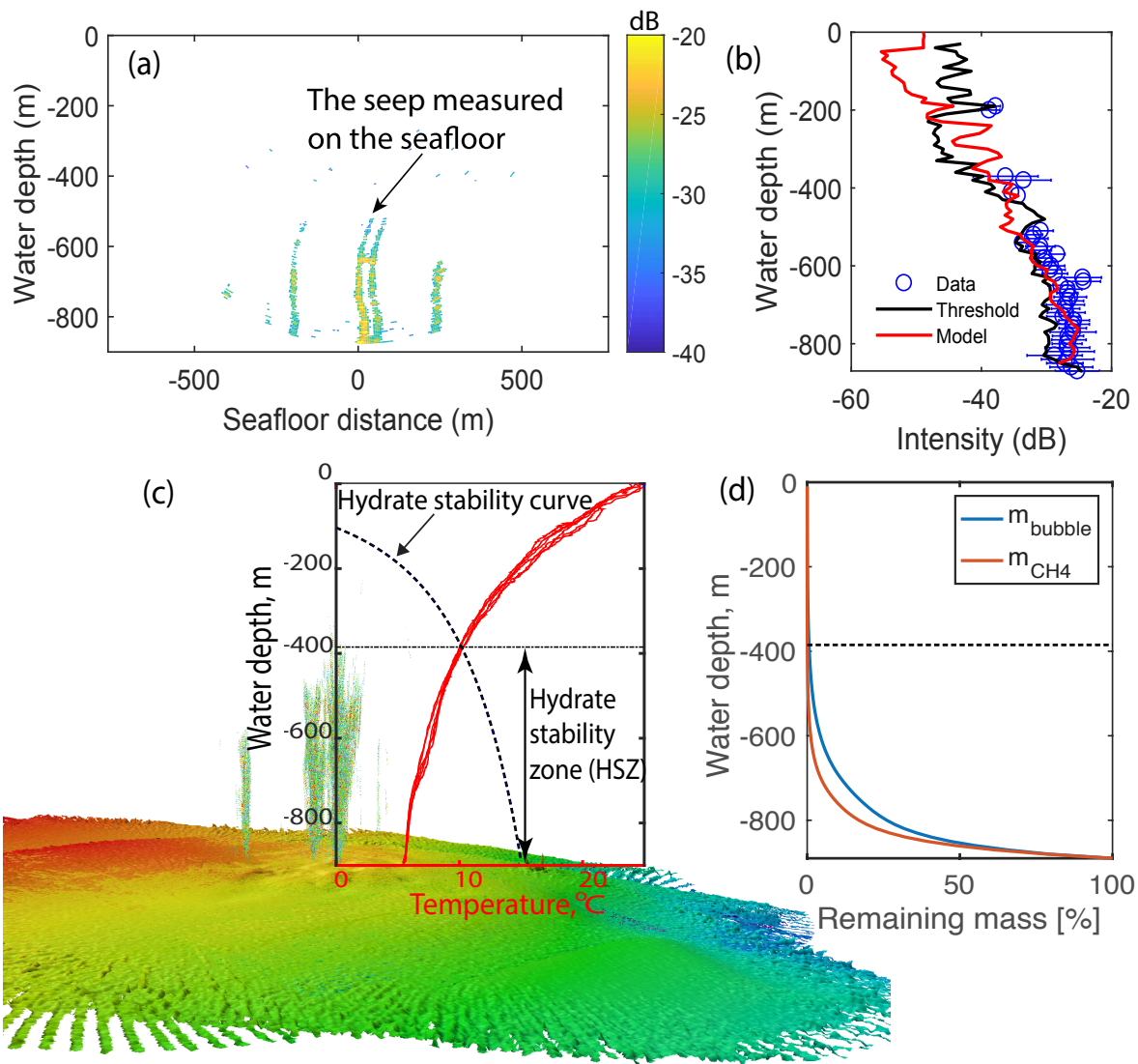


Figure 45: Comparison between the measured and modeled acoustic data from the EM 302 multi-beam sonar: (a) acoustic anomaly in the watercolumn measured by the EM 302 after dive H1403 (the color bar shows the backscatter intensity, dB); (b) comparison of the measured backscatter intensity from the EM 302 (blue circles) and the modeled target strength (red line, offset by  $-17$  dB); the solid black line reports the acoustic background used as a threshold to identify the EM 302 watercolumn anomalies of the bubble flare; (c) the measured acoustic anomalies in the watercolumn by the EM 302 in the context of the surrounding bathymetry; the measured temperature profiles and the calculated hydrate stability curve are superposed in subplot (c), showing the Hydrate Stability Zone (HSZ) from the seafloor to 385 m water depth. (d) the percentage of remaining mass of released natural gas and methane as a function of water depth computed by the model. The horizontal dashed line shows the the hydrate stability line, where the remaining mass of total gas is 0.6%, and the remaining mass of methane is 0.1%.

Milestone concluded all Milestones for Task 6.

### **A.7 Task 7.0: Document Model Validation**

In this Task, we document the model validation through reporting to NETL, distribution of the model over Github, and reporting of our findings in journal articles in the peer-reviewed literature. As of the writing of this report, publicly available model documentation and validation include:

- Opensource model code. The seep model used here is distributed over the code-sharing site, GitHub, at <https://github.com/socolofs/tamoc>. This distribution includes a detailed user manual and several example scripts.
- The present Final Scientific/Technical Report.
- The synthesis publication in *Geophysical Research Letters* by (Wang et al., 2020)

Several other manuscripts remain in preparation and/or review. As any of these manuscripts become published, they will be submitted to the OSTI database with a link to the award number for this project.

### **Progress Toward Milestone**

Milestone 8 (Complete model validation) was completed on April 30, 2019 and verified by the quarterly report for that reporting period. This work is summarized above in Sections 4 and 5 of this report.

### **A.8 Task 8.0: Data Distribution / Archiving**

In this project, we have generated three types of data:

1. Post-processed results from the NETL HPWT. During this project, we utilized a comprehensive dataset of camera images and system state data collected by NETL in their HPWT. Post-processed results from these data were also reported by NETL in their reports by Levine et al. (2015) and Warzinski et al. (2014a). We validated the computed results from these reports as part of our Task 2 work and concluded that our image analysis agrees with the data already reported by NETL. Hence, we have not changed any of these data from its original form. As we are not permitted to disseminate this data further, the original data repository remains the property of NETL.
2. Post-processed data from the GISR G07 and G08 cruises. This project utilized the high-speed, stereoscopic camera data, M3 acoustic multibeam data, and EM302 multibeam data

collected during the GISR G07 and G08 cruises in the northern Gulf of Mexico. The baseline data was collected through funding from the Gulf of Mexico Research Initiative (GoMRI). This data is distributed from the Gulf of Mexico Research Initiative Information and Data Cooperative (GRIIDC). Each dataset and its archive location is summarized in Table 6.

3. Numerical model code associated with the TAMOC model. We have now thoroughly updated TAMOC with all of the results obtained through this project and have uploaded a new version of the code, now compatible with Python 3. The opensource code base is distributed from: <https://github.com/socolofs/tamoc>.

These data archives represent all of the raw data utilized and generated by this project. The post-processed results and analysis conclusions are all included in the Appendices and Digital Appendices of this report. Hence, the data distribution and archiving activities of this project are concluded.

Table 6: Summary of data repositories for GISR cruises G07 and G08.

Data DOI	Data Citation
<b>GISR Cruise G07</b>	
10.7266/N7VM4969	Socolofsky, Scott (2016) HD movie files of bubbles and droplets rising from natural seeps in the Gulf of Mexico taken in July 2014. Distributed by: Gulf of Mexico Research Initiative Information and Data Cooperative (GRIIDC), Harte Research Institute, Texas A&M University-Corpus Christi. doi:10.7266/N7VM4969
10.7266/N7J67F0G	Socolofsky, Scott A. (2016) Underway Data From the E/V Nautilus Cruise NA046 Conducted 16-26 July 2014 in the Northern Gulf of Mexico. Distributed by: Gulf of Mexico Research Initiative Information and Data Cooperative (GRIIDC), Harte Research Institute, Texas A&M University-Corpus Christi. doi:10.7266/N7J67F0G
10.7266/N7QV3JGK	Socolofsky, Scott (2016) High-speed, high-resolution, stereoscopic images of bubbles and droplets rising from natural seeps in the Gulf of Mexico taken in July 2014. Distributed by: Gulf of Mexico Research Initiative Information and Data Cooperative (GRIIDC), Harte Research Institute, Texas A&M University-Corpus Christi. doi:10.7266/N7QV3JGK.
10.7266/N7N014GM	Breier, Chip (2015) Methane Concentrations in Gas Plumes from Mississippi and Green Canyon Seeps, July 2014. Distributed by: Gulf of Mexico Research Initiative Information and Data Cooperative (GRIIDC), Harte Research Institute, Texas A&M University-Corpus Christi. doi:10.7266/N7N014GM
<b>GISR Cruise G08</b>	
10.7266/N79C6VB3	Socolofsky, Scott (2016) ROV Video of Natural Gas Seeps, Gulf of Mexico, April 2015. Distributed by: Gulf of Mexico Research Initiative Information and Data Cooperative (GRIIDC), Harte Research Institute, Texas A&M University-Corpus Christi. doi:10.7266/N79C6VB3
10.7266/N78P5XKG	Socolofsky, Scott A. (2016) Underway Data From the EV Nautilus Cruise NA056 Conducted 09-21 April 2015 in the Northern Gulf of Mexico. Distributed by: Gulf of Mexico Research Initiative Information and Data Cooperative (GRIIDC), Harte Research Institute, Texas A&M University-Corpus Christi. doi:10.7266/N78P5XKG
10.7266/N7GF0RF5	Socolofsky, Scott (2016) Stereoscopic high-speed high-resolution camera images of natural gas seeps observed at the seafloor and in the water column on GISR Cruise G08 to MC 118 in April 2015. Distributed by: Gulf of Mexico Research Initiative Information and Data Cooperative (GRIIDC), Harte Research Institute, Texas A&M University-Corpus Christi. doi:10.7266/N7GF0RF5
10.7266/N7610XXW	John Kessler, Mihai Leonte (2018) Concentrations of gas dissolved in seawater and in gas bubbles collected in the northern Gulf of Mexico, April 12-20, 2015. Distributed by: Gulf of Mexico Research Initiative Information and Data Cooperative (GRIIDC), Harte Research Institute, Texas A&M University-Corpus Christi. doi:10.7266/N7610XXW

## B Hydrate Formation Time and Bubble Size Distributions

Datasets derived for Subtasks 2.1 (Evaluate Hydrate Formation Time) and 3.1 (Bubble Characteristics from High-Speed Camera) were submitted to NETL previously in the Technical Report for Decision Point 1. In this appendix, we repeat the data description portion of this report and include the post-processed datasets.

### B.1 Introduction

In this project, we analyzed data for the dynamic behavior of natural gas bubbles in the ocean water column using laboratory and field data and applied this data to validate a numerical model for bubble rise and evolution in the deep ocean water column. Laboratory data were collected by the U.S. Department of Energy (DOE) National Energy Technology Laboratory (NETL) in their High Pressure Water Tunnel (HPWT). The field data were collected by the project PIs during two cruises in the Gulf of Mexico by the Gulf Integrated Spill Research (GISR) Consortium, funded by the Gulf of Mexico Research Initiative. The analysis of this data was the subject of project Tasks 2 and 3. Project Task 4 used this data to validate and adapt an existing numerical model for bubble flares in the deep ocean water column.

The purpose of this appendix is to summarize the data analysis outcomes for Subtasks 2.1 and 3.1. These outcomes were provided to NETL through the Technical Report for Decision Point 1, and included the following:

- ***Subtask 2.1 (Evaluate hydrate formation time)***. The recipient provided to DOE a table of data listing each HPWT experiment and the hydrate formation time evaluated for that experiment. For experiment where the hydrate formation time could not be evaluated, a comments column was included with the table explaining the reason.
- ***Subtask 3.1 (Bubble characteristics from high-speed camera)***. The recipient provided to DOE a second table of data listing each high-speed camera dataset for both the 2014 and 2015 GISR cruises and the post-processed values of the median bubble diameter, the standard deviation of a log-normal fit to the volume size distribution, and the mean rise velocity of the bubbles.

This appendix documents the metadata for these two datasets and presents the data tables.

Table 7: Summary of individual CH<sub>4</sub> and C<sub>1</sub>C<sub>2</sub>C<sub>3</sub> bubble observations

Gas	Water	# of Bubbles
CH <sub>4</sub>	RO Water	21
CH <sub>4</sub>	Artificial Seawater	7
C <sub>1</sub> C <sub>2</sub> C <sub>3</sub>	RO Water	5
C <sub>1</sub> C <sub>2</sub> C <sub>3</sub>	Artificial Seawater	19
C <sub>1</sub> C <sub>2</sub> C <sub>3</sub>	Artificial Seawater with Dispersant (Corexit)	13

## B.2 Hydrate Formation Time

The Digital Appendix B.4 presents our analysis of the hydrate formation time for all of the available data for pure methane (CH<sub>4</sub>) and for a natural gas mixture of methane, ethane, and propane (C<sub>1</sub>C<sub>2</sub>C<sub>3</sub>) in the NETL HPWT Dataset. In the appendix, we present the gas hydrate formation time (or video frame number) and selected images of the hydrate morphology for the different pressure and temperature combinations available in the HPWT dataset. In all, 65 individual bubbles were observed with hydrate formation (28 individual bubbles for CH<sub>4</sub> and 37 individual bubbles for C<sub>1</sub>C<sub>2</sub>C<sub>3</sub>). A summary of the experimental conditions is provided in Table 7. All results for each individual bubble are presented in the Digital Appendix B.4.

Two main data sources of the original HPWT dataset provide the raw data for each observation. First, continuous monitoring data for the system temperature, pressure, and operation of the syringe pumps are recorded in files with the extension `.tdms`. Figure 46 shows a sample recording of the pressure and temperature data for one of the CH<sub>4</sub> experiments from the corresponding `.tdms` file. The syringe pump data include the operation of the pumps that pressurize the water tunnel as well as the pumps that inject the gas bubble into the test section. Second, video files for each experiment show close-up images of each bubble in which it is possible to identify the degree of hydrate formation (none, partial, or complete). Figure 47 shows a sample of six images for one bubble during the experiment depicted in Figure 46. In this example, we consider the hydrate to have completely coated the bubble surface in Frame C of Figure 47. This determination is made based on the appearance of hydrate on the bubble surface and also by the apparent rigidity of the bubble-water interface in the dynamic video images. For each experiment, we identify all points in time for which either the hydrate conditions or experimental pressure change (e.g., diamonds in Figure 46) and we extract individual camera images documenting the bubble conditions at each of these times (as in Frames A-F in Figure 47). The results of this data analysis are presented for each experiment in the Digital Appendix B.4.

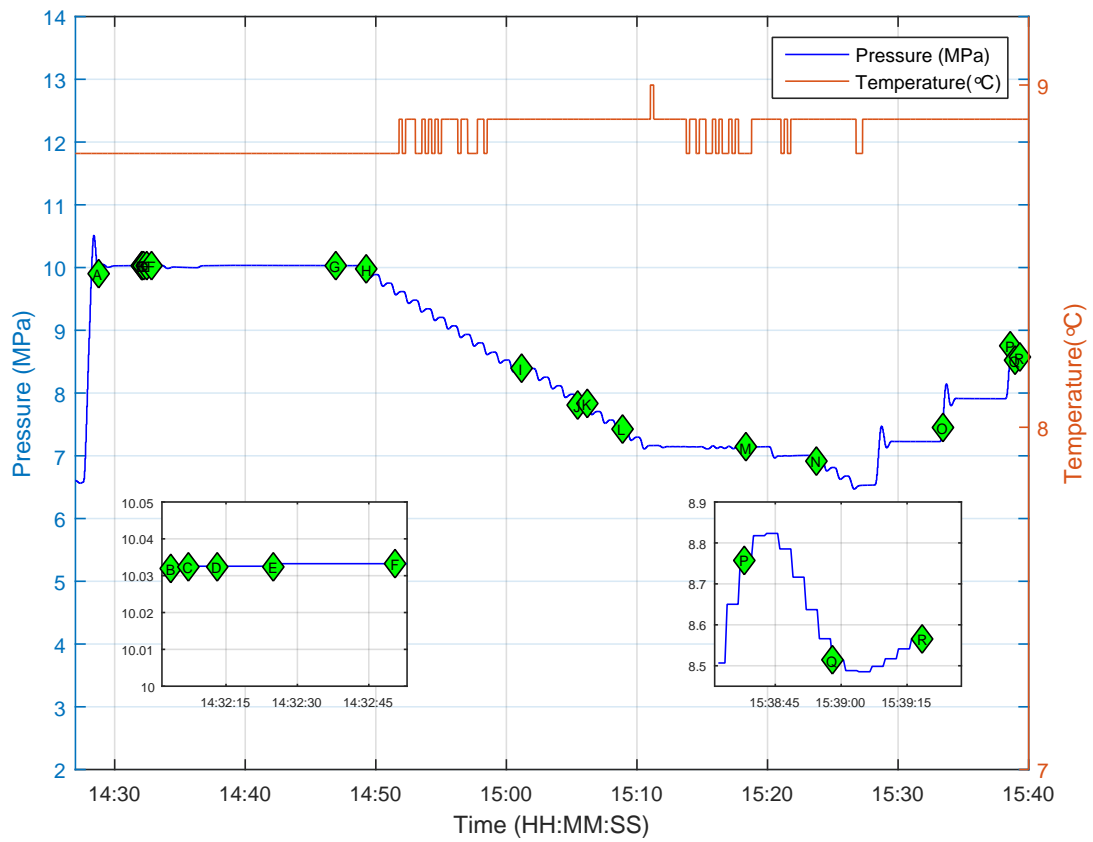


Figure 46: An example of time series of ambient conditions for a bubble before, during, and after hydrate formation.

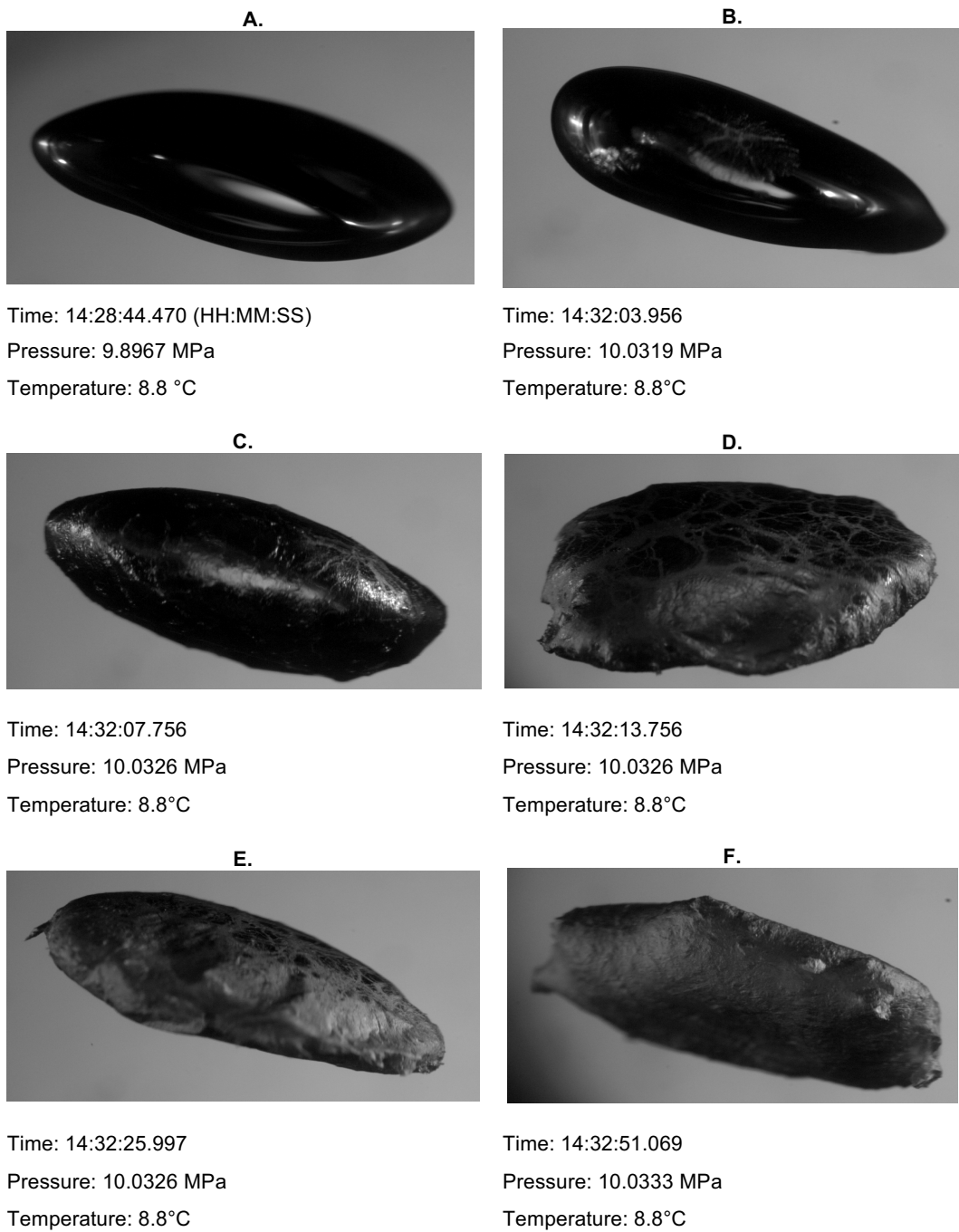


Figure 47: An example of morphological change of a bubble before, during, and after hydrate formation. The selection of A-F is shown in Figure 46.

To evaluate the hydrate formation time, we must determine when the bubble enters the test section and when the images show complete hydrate coverage. The time stamps for all `.tdms` data were recorded in GMT format. For the image data, different methods were used to record experiment time. During some experiments, the time clock is displayed in the images themselves by a watermark, and varied between local standard and daylight savings time. During other experiments, the time clock is not watermarked, and time can only be inferred by counting frames with a known or assumed image frame rate. In this latter situation, a complication also arises when there are apparent gaps in the continuous video recording (e.g., two videos are spliced together with an unknown gap duration). We used video analysis software to read the metadata header for all videos to determine whether detailed clock data were contained in the headers. Unfortunately, for the experiments without the digital watermark for time, we can only count frames, and times become unknown following the first gap in the image sequence. In any case, the frame number for each observation is recorded, and the majority of data have quantitative time stamps.

The hydrate formation time is reported as the elapsed time between bubble injection and the first occurrence of complete hydrate coverage of the bubble. While the complete hydrate coverage frame can be identified within an uncertainty on the time of order 1 s, the injection time is more ambiguous. The experimental procedure used by NETL was to run the water tunnel to a pressure and temperature condition just inside the hydrate stability zone (HSZ), inject gas bubbles into an inverted cup, and finally release a single bubble from the cup into the conical counterflow section. Bubble injection can take several seconds to several minutes, during which time the injected gas collects in the inverted cup. We consider the start of the hydrate formation time (onset time) to begin when the syringe pump begins injecting the gas into the cup. This time can be clearly identified from the times series data in the `.tdms` data and is an objective moment in the experiment. We could have also chosen the moment that the syringe pump completes the injection of gas. Both times are reported in our dataset.

In the Digital Appendix, we provide a description of the data structure for the post-processed experimental data, a sample analyzed dataset for one complete experiment, and a digital archive of all post-processed data.

### **B.3 *In situ* Bubble Characteristics**

During the GISR field cruises, bubbles in natural seep flares were observed at Mississippi Canyon lease block 118 (MC 118) and Green Canyon lease block 600 (GC 600) using both acoustic and camera-based systems. Here, we focus on the video data from a high-speed, stereoscopic imaging system that was mounted on the *ROV Hercules* and observed the gas bubbles *in situ*. This imaging

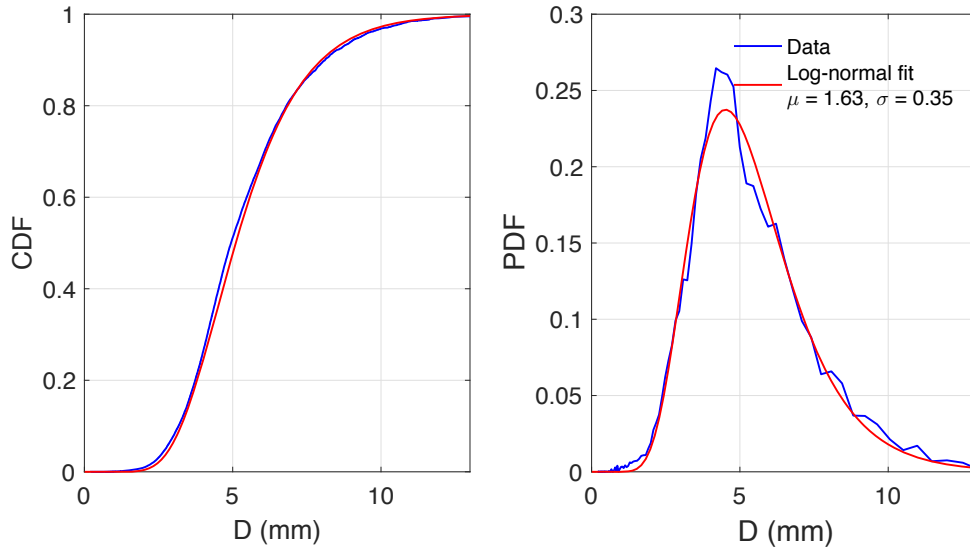


Figure 48: Volumetric bubble size distribution for the measured data and a fitted log-normal distribution. Left panel: cumulative distribution function; right panel: probability distribution function.

system is described in (Wang and Socolofsky, 2015a). Our image analysis methods are explained and validated in (Wang and Socolofsky, 2015b), and the results for the first of the two GISR cruises is published in (Wang et al., 2016). Results for the second GISR cruise is published in (Wang et al., 2020).

Figure 48 shows an example measurement during the second GISR cruise in April 2015 to MC 118. Both the cumulative distribution and probability density function of bubble sizes based on volume fit well to a log-normal probability distribution. Figure 49 shows a summary of the rise velocity data for the same cruise. The data are well within the range of observed bubble rise velocities for a wide range of data (colored lines). As outlined in the description of Decision Point 1, above, we report here the fitted values for the log-normal distribution and the measured mean bubble rise velocity for each *in situ* sample collected during both GISR cruises.

In the Digital Appendix B.4, we present an Excel spreadsheet containing all of the measured data and a separate text file describing the metadata for each measurement.

#### B.4 Digital Appendix

Digital Appendix B contains the post-processed data from Subtasks 2.1 and 3.1 of the project. The directory structure and contents of these data are described as follows.

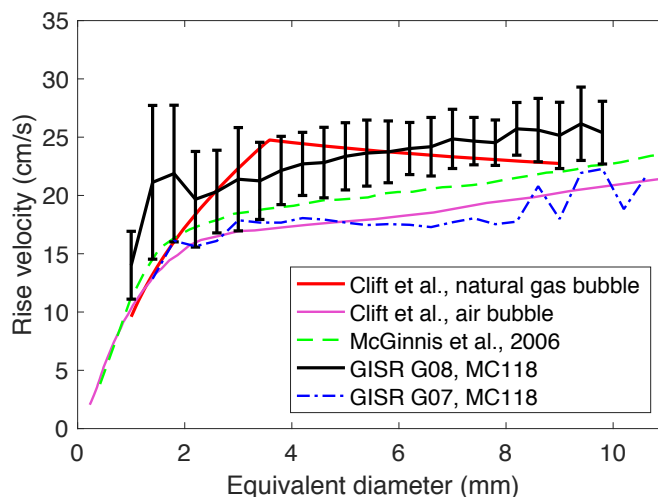


Figure 49: Measured rise velocity versus bubble size. Errorbars show the standard deviation of instantaneous rise velocity data.

#### B.4.1 Subtask 2.1 - Hydrate Formation Time

This section of the Digital Appendix contains three output files for each HPWT experiment. These are each named in the format `yyyymmdd_<nnn>Bubble_<type>.<ext>`, where

- `<nnn>` reports the bubble number
- `<type>` is `Images` (a catalog of video image frames documenting the bubble at each identified observation point), `observ` (an Excel spreadsheet that reports the time and conditions of each observation point), or `PTgraph` (a plot of the pressure and temperature versus time with each observation point marked)
- `<ext>` is either `.pdf`, `.xlsx`, or `.eps`

These data files are organized in two different ways. In the main directory `./ByDate`, each sub-directory is for a different date on which an experiment was conducted. Under each date in this directory branch, each of the three output files are collected together. Three other main directory branches are `./Images`, `./Observation`, and `./PTgraph`. The three main output types are collected in each branch, named by the date of the experiment. Each of these main directory trees are contained under the top directory branches `./C1C2C3_Deliverable` and `CH4_Deliverable`. This directory structure information is also summarized in the top-directory file `DirectoryManual.docx`. Finally, one Excel spreadsheet contains the hydrate formation time for the first hydrate event in each experiment; this file is `Summary of hydrate formation time.xlsx`.

The remaining pages in the text to this Appendix include the following samples for one experiment, the third bubble on June 11, 2012:

- **PTgraph.** A plot of temperature and pressure versus time with 38 green diamonds indicating when events of interest occurred. Each of these 38 events is documented in the following Excel file and the image clips.
- **observ.** An Excel spreadsheet that identifies each of the 38 events of interest and reports a description of the event, the clock time, elapsed time, system pressure, system temperature, the pressure of the boundary of the HSZ, the frame number from the video file, the extension of the video file format (.cine or .avi), and the file location where the raw video file is stored on the network hard drive that contains the complete HPWT dataset.
- **images.** A set of image clips that show the bubble at each of the events of interest identified above. In these images, only the bubble is shown, not the entire image frame in the video.

This common set of output is provided in the Digital Appendix for all experiments in Table 7.

#### **B.4.2 Subtask 3.1 - *In situ* Bubble Characteristics**

This section of the Digital Appendix contains two files:

- **GISR\_MetaData.txt** is a short file giving a text description for each column in the main Excel data file.
- **Subtask3.1\_bubble\_characteristics.xlsx** contains the measured data for each image sequence.

More information about these measurements is contained in the publicly available data sets for the GISR cruises. These are summarized in Table reftab:griidc of this report.

## C Tracking of Hydrate Crystals on Bubble Interfaces

The results of our analysis to track hydrate crystal on the interfaces of bubbles using the high-speed camera data collected by NETL were summarized in our quarterly Research Performance Progress Report for the first quarter of FY2018. The relevant section of that report is included here as follows.

The high-resolution video images of the bubbles in the NETL High-Pressure Water Tunnel (HPWT) clearly show the morphology of the hydrate shell on the bubbles. For some of the experiments, hydrate crystals are observed on the bubble-water interface that do not completely cover the bubble surface. In our proposal, we noted that these crystals had been observed to move, and we hypothesized that this movement may enhance the mass transfer coefficient, similarly to convective mixing for chemically clean bubbles with mobile bubble-water interfaces. For Subtask 2.2, we proposed to identify hydrate crystals on the bubble-water interface and to track their movement, confirming that the surface of these bubbles is indeed flowing.

### C.1 Methods

Hydrate crystals can only be tracked in video images from the high-speed cameras. These cameras collect data to an onboard RAM card that fills up within a few seconds and must be downloaded over several minutes to a connected computer before another sequence of high-speed images can be captured. For these reasons, high-speed video data is not available continuously for any of the experiments.

Figure 50 demonstrates the methods we used to confirm movement of hydrate crystals on the bubble-water interface and to compute the speeds of this movement. Because the bubble itself moves relative to the fixed camera, movement must be identified in a reference frame moving with the bubble. We established a reference point for each bubble that is an identifiable object in a part of the bubble shell that does not appear to move across the surface of the bubble. In Figure 50, this reference point is the dark black region on the far right-hand side of the bubble, near the equator of the oblate spheroid. To track the hydrate crystals, we also identify a prominent hydrate plate, identified in Figure 50 by the point A.

The locations of both the Reference point  $\vec{x}_R$  and the tracked crystal point A  $\vec{x}_A$  can be converted to real space using the calibration images that establish the camera image scale. We designate these points in Cartesian space for Frame 1 of the image sequence as

$$\vec{x}_R = (x_{R,1}, y_{R,1})$$

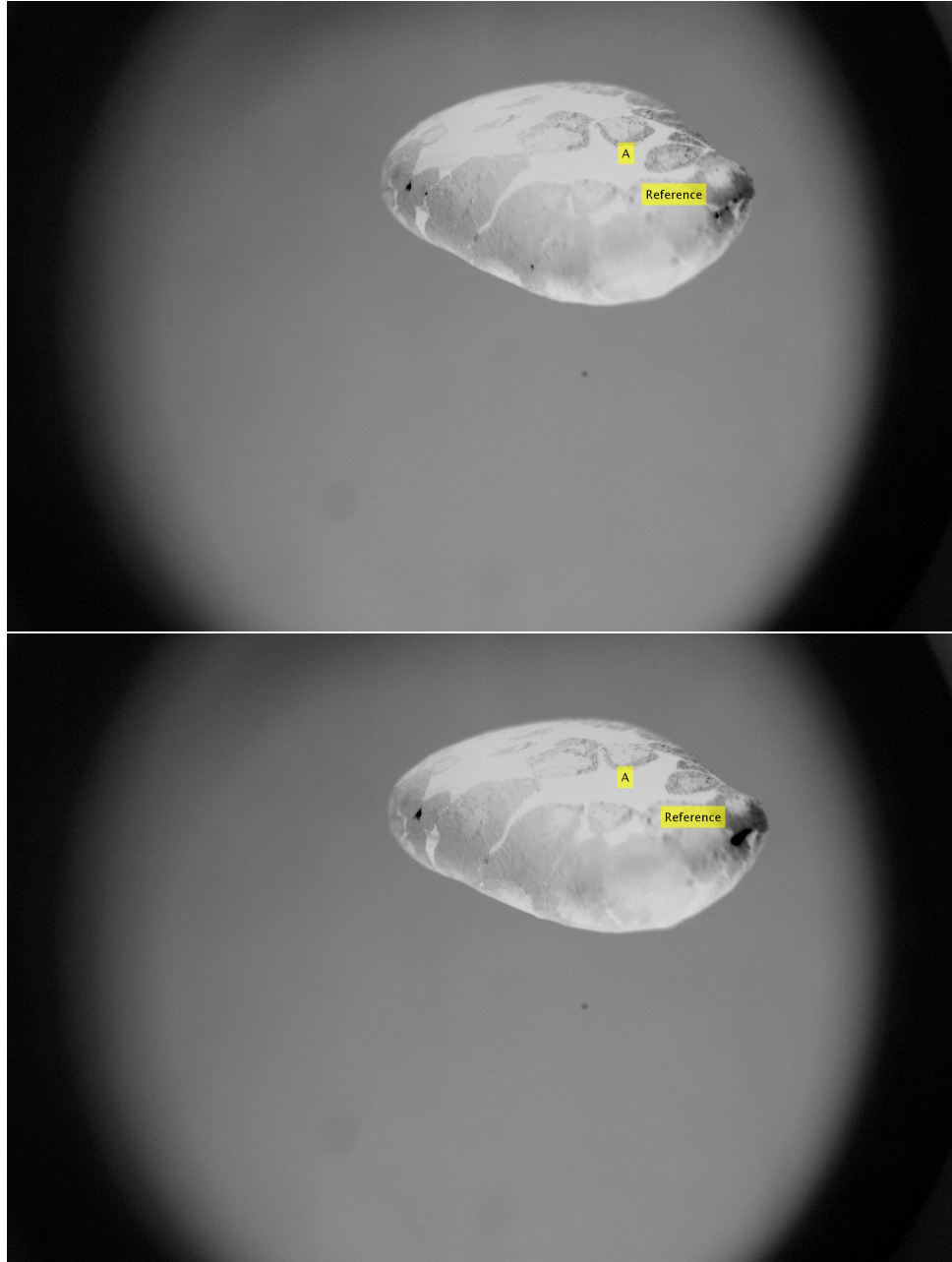


Figure 50: High-speed camera image for two adjacent frames of the video sequence. The reference point and the location of hydrate plate A is shown in each image.

$$\vec{x}_A = (x_{A,1}, y_{A,1}) \tag{30}$$

If the hydrate crystal is moving across the surface of the bubble, then the distance between the Reference point and point A will change between two successive image frames. The separation distance between these points for Frame 1 is given by

$$L_1 = \sqrt{(x_{R,1} - x_{A-1})^2 + (y_{R,1} - y_{R,2})^2}. \tag{31}$$

If  $L$  is changing over time, then the hydrate crystals are moving. Since we also know the frame rate of the camera, the time span  $\delta t$  between frames is known, and the apparent, absolute speed  $V$  of the movement of the hydrate crystal can be computed as

$$V = \left| \frac{L_2 - L_1}{\delta t} \right|. \tag{32}$$

For the two frames in Figure 50, point A is moving away from the reference point from Frame 1 (upper image) to Frame 2 (lower image).

One important complication for this calculation is that the bubble is a three-dimensional oblate spheroid and we are making these calculations on a two-dimensional projection to a Cartesian grid. As a hydrate plate moves from the side of the bubble nearest the camera toward the back side (as is occurring in Figure 50), the displacement distance becomes foreshortened with time, and the speed estimated by Equation 32 will underestimate the true speed due to an underestimation of the true separation distance. When a plate moves from left-to-right in the image, this projection error is minimized, and our computed speeds are close to the real speeds. For the analysis presented here, we should interpret the reported speeds as conservative estimates in the sense that the true speeds of some plates are faster than we compute. This error is acceptable since the main objective of Subtask 2.2 is to confirm that hydrate plates are moving and to estimate the order of magnitude of their translation speeds.

## C.2 Available Data

As discussed above, not all experiments have high-speed camera data, and none of the experiments have continuous data throughout the experiment. In our analysis for this subtask, we watched all of the available high-speed camera data and classified it into categories of with and without moving hydrate shells. Table 8 summarizes those experiments that have high-speed camera data with moving plates and the number of high-speed camera sequences that were taken during times where plates were observed to move on the bubble-water interface.

One thing that we noticed regarding moving hydrate plates is that they generally occur when the pressure in the HPWT is changing with time. Pressure changes often result either in formation of

Table 8: Table of experiments in the NETL High-pressure Water Tunnel having high-speed image data.

<b>Serial Number</b>	<b>Date</b> (MM/DD/YYYY)	<b>Bubble No.</b>	<b>Gas</b>	<b>Number of Video Files</b> <b>Having Moving Plates</b>
1	05/18/2012	1st	CH <sub>4</sub>	25*
2	06/11/2012	3rd	CH <sub>4</sub>	12*
3	06/12/2012	5th	CH <sub>4</sub>	3
4	06/28/2012	2nd	CH <sub>4</sub>	35
5	06/29/2012	3rd	CH <sub>4</sub>	17*
6	10/23/2012	3rd	CH <sub>4</sub>	14
7	07/23/2014	1st	CH <sub>4</sub>	4
8	07/23/2014	2nd	CH <sub>4</sub>	3
9	07/24/2014	2nd	CH <sub>4</sub>	1
10	07/29/2014	2nd	CH <sub>4</sub>	4
11	07/31/2014	1st	CH <sub>4</sub>	3
12	01/15/2013	2nd	C1C2C3	1
13	01/28/2013	1st	C1C2C3	1
14	01/31/2013	1st	C1C2C3	1
15	03/12/2013	2nd	C1C2C3	1
16	03/13/2013	1st	C1C2C3	4
17	03/18/2013	1st	C1C2C3	6
18	03/21/2013	1st	C1C2C3	2
19	06/21/2013	1st	C1C2C3	10
20	06/27/2013	1st	C1C2C3	3
21	06/27/2013	2nd	C1C2C3	1
22	06/28/2013	1st	C1C2C3	7
23	11/21/2013	1st	C1C2C3	4

\*Experiments marked by an asterisk indicate the experiments we have fully analyzed for Subtask 2.2.

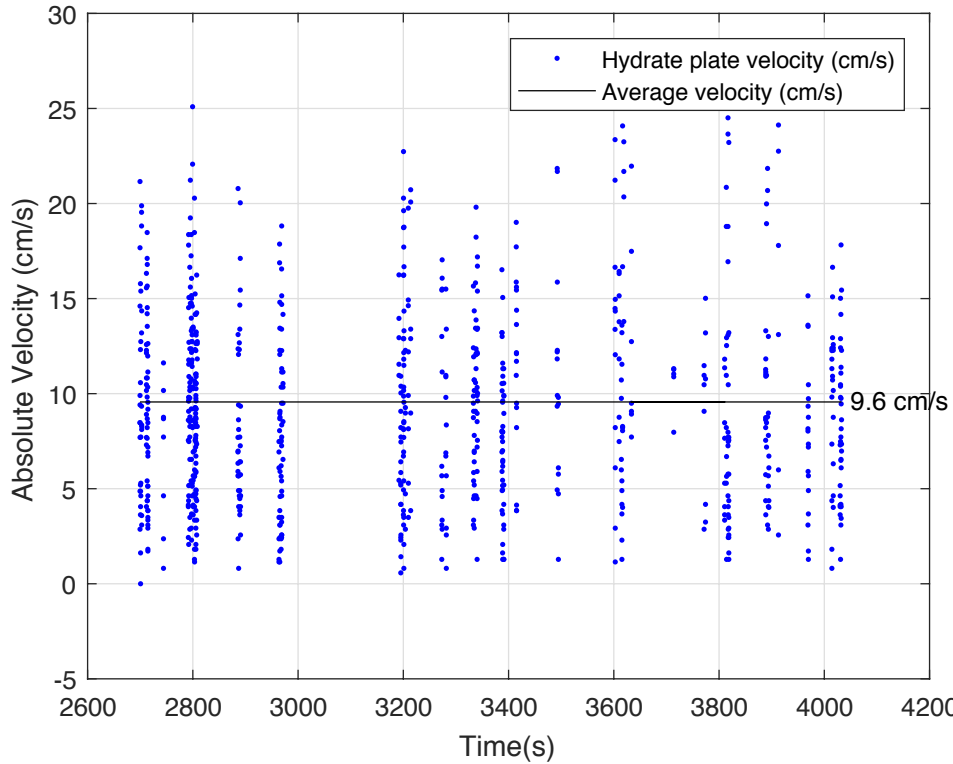


Figure 51: Speed of moving hydrate plates on a pure methane bubble recorded on May 18, 2012 for the first bubble.

hydrate (moving from pressures outside or near the hydrate stability zone to much higher pressures) or dissociation of hydrate (moving from pressures with stable and complete hydrate shells to lower pressures). We also observed that the hydrate plates that moved were always of a large, flat shape, similar to those in Figure 50. Bubbles that had many, small hydrate crystals with nearly uniform distribution on the bubble surface did not show relative motion of these hydrate crystals across the bubble-water interface (hence, none of these cases are reported in Table 8).

Our quantitative analysis of the high-speed camera data using the methods outlined above were conducted for the three experiments marked by an asterisk in Table 8, and the results are summarized below.

### C.3 Results

Figure 51 shows the computed speeds for all hydrate plates that we could track in the 25 high-speed camera sequences for the first bubble observed in the HPWT on May 18, 2012. Each cluster of data stems from a separate image sequence. Each blue dot is a speed  $V$  computed using Equation 32 by tracking a hydrate plate between two successive images. Identification of the Reference point and the tracking points (A, B, C, etc.) in the high-speed camera images was completed by hand.

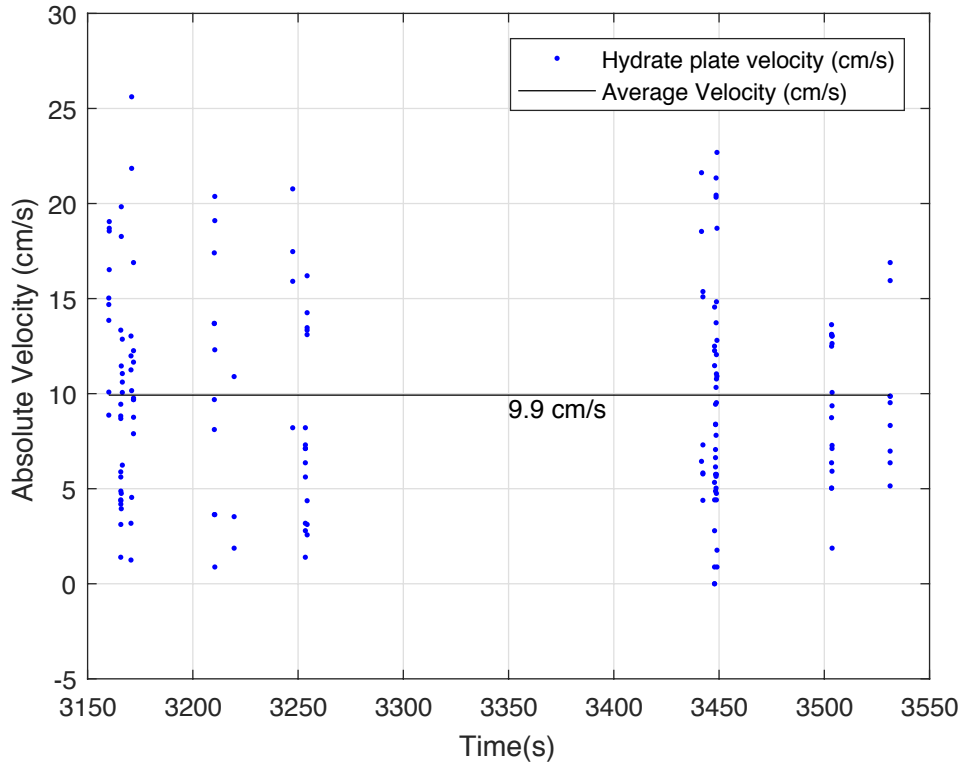


Figure 52: Speed of moving hydrate plates on a pure methane bubble recorded on June 11, 2012 for the third bubble.

Based on the measurements, hydrate shells move at speeds up to 20 cm/s, which is close to the rise velocity of the bubble through the flowing ambient water. For all of the measurements for this experiment, the mean speed of hydrate plate movement is 10 cm/s.

Figures 52 and 53 show similar results for experiments conducted on May 11 and May 29, 2012. Again, the maximum speeds of hydrate plate movement are up to about 20 cm/s, similar to the rise velocities of each individual bubble. Likewise, the mean speeds of hydrate plate movement are close to 10 cm/s (9.9 cm/s and 9.3 cm/s). Hence, when bubbles look similar to that shown in Figure 50, the movement of their hydrate plates appears to be within a consistent range.

#### C.4 Conclusions

Our quantitative analysis of three of the experiments for pure methane having a large number of high-speed video files confirms that when hydrate plates are flat and spread out, they do move, that their speeds of motion across the bubble surface peak near the rise velocity of the bubble (20 cm/s), and that they have an average speed of 10 cm/s; moving plates are always observed on the leading side (top) of the bubble. Individual, flat hydrate plates are most commonly observed during hydrate formation and dissociation, which occur in the HPWT data when the ambient

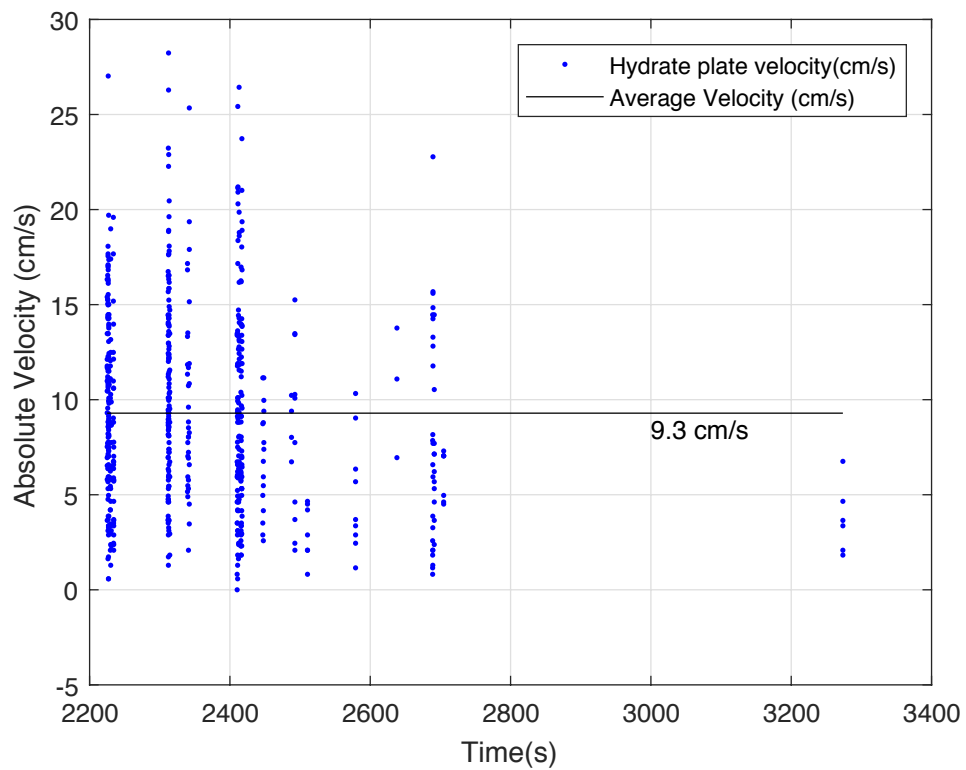


Figure 53: Speed of moving hydrate plates on a pure methane bubble recorded on June 29, 2012 for the third bubble.

pressure in the water tunnel is changing. During hydrate formation, large plates form, similar to Figure 50, and the plates are observed to move with average speeds of order 10 cm/s. During hydrate dissociation, many evenly-distributed hydrate crystals appear on the bubble-water interface, and these are not observed to move relative to each other. Hence, enhanced mass transfer due to the movement of the bubble water interface may be expected during hydrate formation and would not be expected during hydrate dissociation. Because these situations occur in the HPWT data during times with changing pressure, a numerical model is needed to evaluate the competing effects of compression/decompression and dissolution. Hence, we test this hypothesis on mass transfer rates through our model validation in Task 4 (see Section 4 of the main report, above).

## D Acoustic Measurements from the GISR Cruises

A major output of Task 2 of this project was to analyze the acoustic multibeam data collected during the G07 and G08 cruises of the Gulf Integrated Spill Research (GISR) consortium in 2014 and 2015. This results of this work is reported here, collecting data submitted in the Milestone 3 and quarterly Research Performance Progress Reports.

### D.1 Introduction

As part of the Gulf Integrated Spill Research (GISR) consortium, funded by the Gulf of Mexico Research Initiative (GoMRI), the recipient has collected *in situ* field data for natural seep bubble flares in the Gulf of Mexico using optical and acoustics-based platforms Wang et al. (2016, 2020). The observations were made during two field campaigns in July 2014 to Mississippi Canyon lease block 118 (MC 118) and Green Canyon lease block 600 (GC 600) and in April 2015 returning to MC 118. The acoustic data include a haul-mounted Kongsberg EM 302 multibeam echo sounder (30 kHz), which recorded along ship tracks from the *E/V Nautilus*, and a Kongsberg M3 multibeam echo sounder (500 kHz), which was deployed on the remotely operated vehicle (ROV) *Hercules* and mounted in a forward looking mode from the top rack of the ROV. In this project, we used this data to validate numerical models of natural gas bubbles emitted from natural seeps in the hydrate stability zone of the deep Gulf of Mexico. In particular, we compared model-predicted bubble acoustic characteristics with those characteristics observed during the GISR field cruises.

In the report for Milestone 3, we demonstrated that we had developed the analytical tools necessary to quantitatively analyze the EM 302 and M3 multibeam data. In particular, that report:

Prvided a short memorandum summarizing progress in quantitative analysis of the M3 and EM 302 multibeam echo sounder data using standard methods from the literature Jerram et al. (2015); Weber et al. (2012); ?. The report included the calibration curve for the acoustic response of the M3 and its performance compared to the field image data.

This Appendix includes this memorandum which provided a summary of the Matlab routines we developed to analyze this data, sample quantitative output from both acoustic instruments, and an outline for how this data was used with our numerical model for natural gas bubbles in the water column.

## D.2 Matlab Analysis Tools for *in situ* Acoustic Data

We developed two Matlab toolboxes and additional analysis scripts to analyze the multibeam sonar data from the EM 302 and M3 echo sounders deployed during the two GISR cruises (G07 in July 2014 and G08 in April 2015). These toolboxes and analysis scripts are provided along with sample data in the Digital Appendix D, the file structure of which is described in Section D.5. The calibration curve for target strength for the EM 302 dataset is presented in Section D.6.

### D.2.1 Kongsberg EM 302 Multibeam Echo Sounder

To develop analysis tools for the EM 302 data, we have adapted a Matlab toolbox originally provided to us by Dr. Tom Weber at the University of New Hampshire. The toolbox is designed to read the original data files recorded by the EM series of Kongsberg echo sounders in the Matlab environment. The details for the format of the data can be found in the “Instruction manual: EM Series Multibeam echo sounders—Datagram formats,” which can be downloaded from:

[https://www.kongsberg.com/globalassets/maritime/km-products/product-documents/160692\\_em\\_datagram\\_formats.pdf](https://www.kongsberg.com/globalassets/maritime/km-products/product-documents/160692_em_datagram_formats.pdf)

(last accessed November 18, 2020.)

Other documentation for the EM 302 can be found under the EM 302 support page on the Kongsberg website at:

<https://www.kongsberg.com/maritime/products/mapping-systems/mapping-systems/multibeam-echo-sounder-em-302-multibeam-echosounder/>

(last accessed November 18, 2020; note that the EM 302 was no longer being sold at the time of this writing.)

In addition to these resources, Kongsberg has created an algorithm to convert the amplitude level in the EM water column datagram to target strength. We repeat this effective calibration curve in Section D.6 and use this algorithm in our Matlab scripts documented here.

As an example of these analysis routines, we consider the data stored in the EM 302 data file 0001\_20140718\_222017\_Nautilus.wcd, provided in the Digital Appendix D and recorded along one ship track during the G07 cruise at MC 118. Figure 54 shows an example plot for one ping in the ship track data file. The upper panel in the figure shows the raw amplitude data recorded by the instrument, and the lower panel shows the data after converting to target strength using the algorithm in Section D.6. Both images are created using our Matlab scripts and plotted in the Matlab environment.

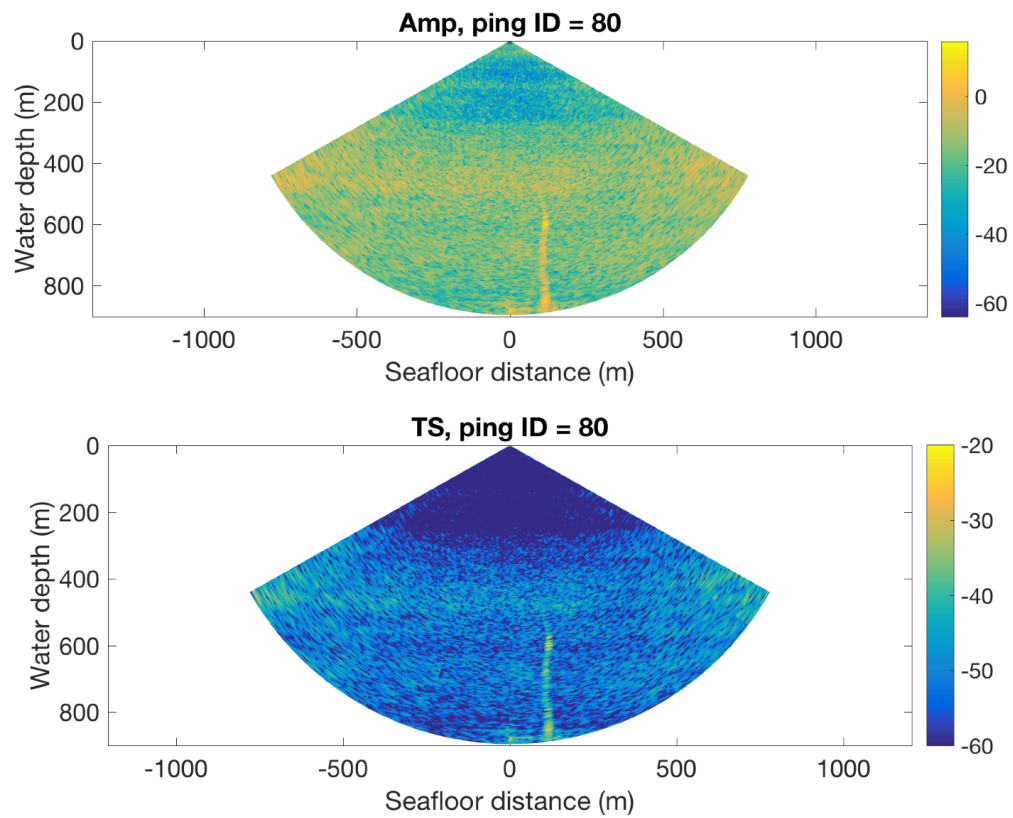


Figure 54: Sample plot of the EM 302 water column data during one ping. Upper panel: amplitude level; lower panel: target strength.

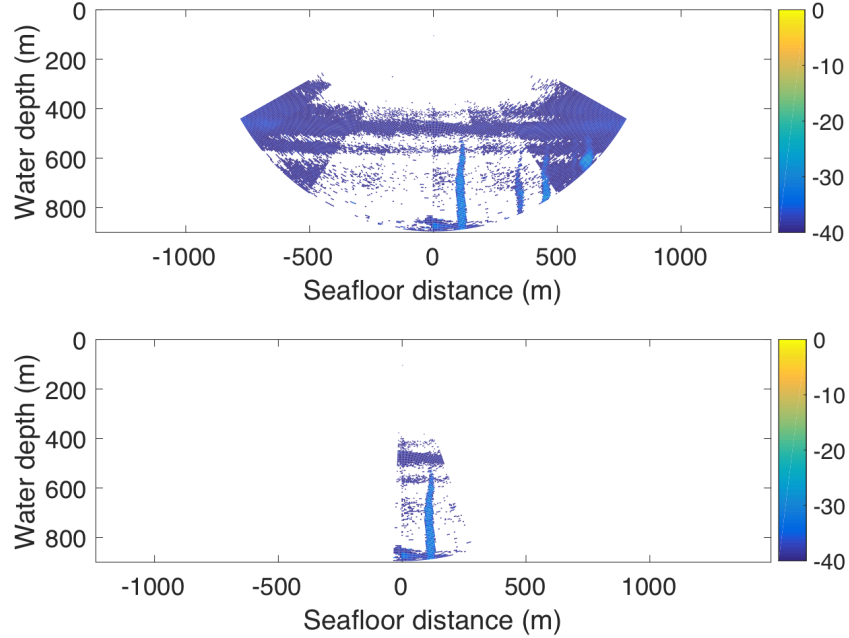


Figure 55: Visualization of seeps along the ship track during the total of 388 pings. All of the data with the target strength less than  $-40$  dB are eliminated for better visualization. Upper panel: all seeps; lower panel: the seep of interest, where the *in situ* data was collected.

To isolate the acoustic information related to the seep flare from that of the surrounding water, we apply a noise threshold to the target strength data. Figure 55 shows the result using a threshold of  $-40$  dB. In the upper panel, we show several of the seeps present in the area. Since we only have *in situ* camera and M3 measurements for one of these seeps, the lower panel of the figure shows the seep of interest isolated from the surrounding seeps. We use this last image to compute the average target strength profile as a function of water depth. This profile is reported in Figure 56. Using different threshold values, different amounts of background acoustic noise will be counted in the target strength profile. For this dataset,  $-40$  dB seems to be an optimal trade-off between capturing the acoustic response of the seep and eliminating background noise. In subsequent analysis, we later determined that the mean target strength at each depth level is the most appropriate threshold for removing background noise; see (Wang et al., 2020) for more details.

The target strength profile in Figure 56 contains information related to the size and number of bubbles in the seep flare at each height recorded in the dataset (10 m intervals in the figure). We use these measured target strength profiles to compare to target strength profiles from our numerical model of these seeps (see also Section D.4). Hence, using these algorithms, we can extract the acoustic target strength profiles of individual seeps of interest from the ship track data of the EM 302 multibeam echo sounder. To access the original multibeam data, see the datasets

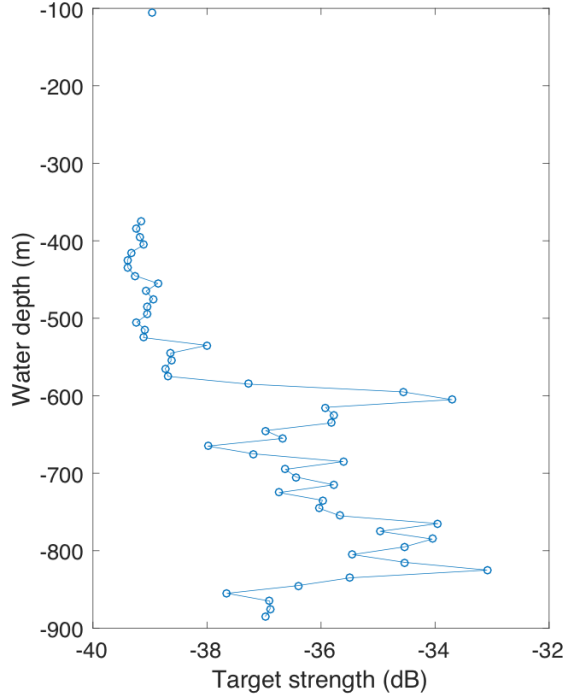


Figure 56: Profile of target strength for the seep of interest showing in Figure 55 (lower panel).

reported in Table tab:griidc.

### D.3 Kongsberg M3 Multibeam Echo Sounder

Our Matlab toolbox and analysis scripts for the M3 multibeam echo sounder are based on a toolbox provided by Kongsberg (personal email communication). Using this toolbox, we are able to read the acoustic data from the raw M3 recorded files (.imb format) and display and analyze them in the Matlab environment. The .imb files contain the data after beam forming. The data stored in these files are a series of complex numbers, which contain intensity and phase. The intensity is related to the target strength, and the phase provides some wave propagation information related to the range, angle of travel, and wavelength.

As an example, we demonstrate analysis of data stored in 2015apr15\_112039\_003d.imb and the sequential files for this survey. Figure 57 provides an example of a single ping image from the M3, plotted using our toolbox. The data are presented in fan view (which yields the slice observed by the M3 to proper scale) and in a Cartesian coordinate system of range and beam angle. Since the M3 was mounted in a forward-looking attitude on the ROV *Hercules*, this image shows a cross-section through the bubble flare. The core of the bubble plume is represented by the bright colors in the range of 2 to 9 m from the M3. The additional, bright object at about 15 m and 30° angle

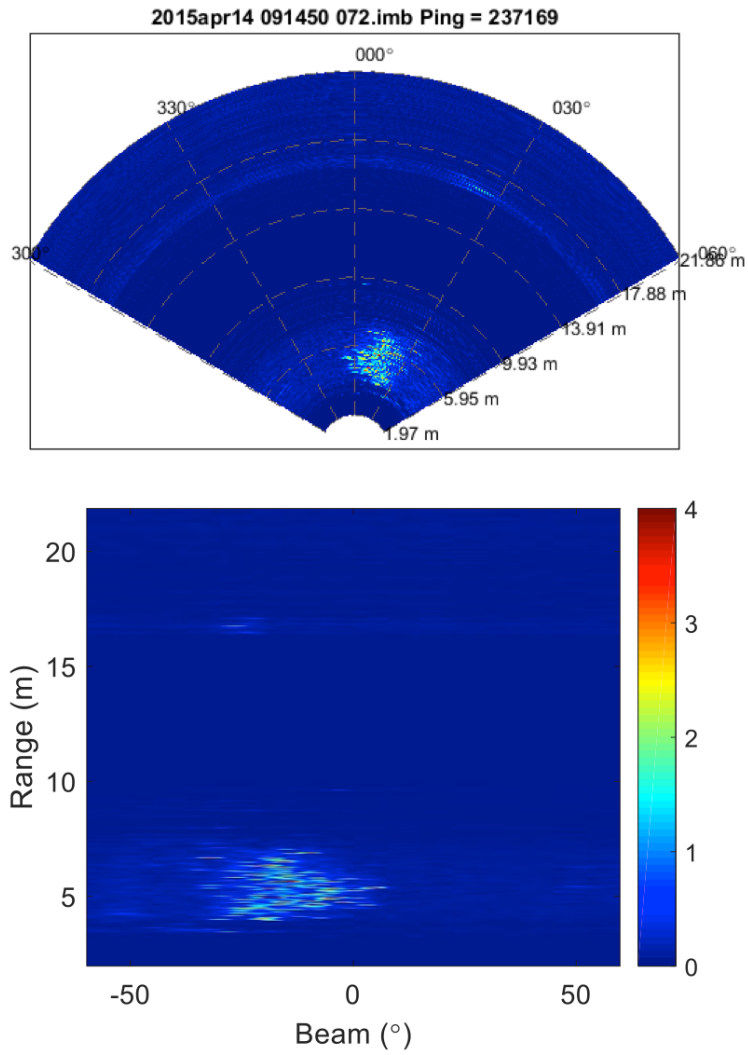


Figure 57: Example of an M3 sonar image. Upper panel: in fan view; lower panel: in Cartesian coordinate system.

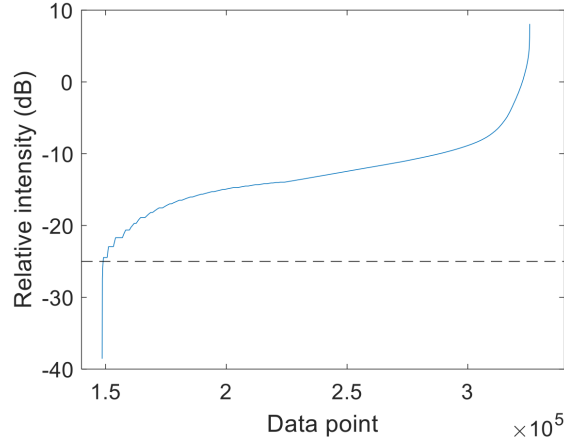


Figure 58: Cumulative distribution function of relative intensity of the bubble scattering shown in Figure 57. A noise level of  $-25$  dB (horizontal dashed line) was empirically determined from this distribution.

is a reflection from the *Argus* vehicle, which is part of the tether management system for *Hercules*. From the data in either coordinate system, geometric properties (e.g., length and width) of the seep flare as a function of height can be computed.

To isolate the bubble flare information in Figure 57 we need to apply a threshold to remove the background noise, similarly to what was done above for the EM 302 target strength data (i.e., Figure 55). To determine the correct thresholding value, we consider Figure 58, which shows the cumulative distribution function of the relative intensity for each pixel in Figure 57. Based on this figure, we determined a noise threshold of  $-25$  dB to remove pixels from the background.

If we apply the  $-25$  dB threshold and then sum the intensity from all remaining pixels, we can track the evolution of the acoustic response throughout a survey of the flare using the M3. Figure 59 shows the intensity data for each acoustic image as a function of time for one survey at MC 118. The top panel shows the total image intensity, the second panel presents the average acoustic intensity, the third panel shows the total area with a return above the threshold value, and the fourth panel reports the water depth of the sensor at each time. The first half of the data were recorded at the seep source, followed by a slow ascent of the sensor as we tracked the flare up through the water column.

The data in Figure 59 are computed from the raw acoustic data without calibration to obtain target strength. We can clearly see the variability of the acoustic response as a function of instrument settings in the figure. In the upper panel, we point out where the signal intensity changes as the range changes (in this case, the range is changed from 32 m (lower intensity) to 22 m (higher intensity)). To remove this range dependence, we can either convert all intensity values to relative

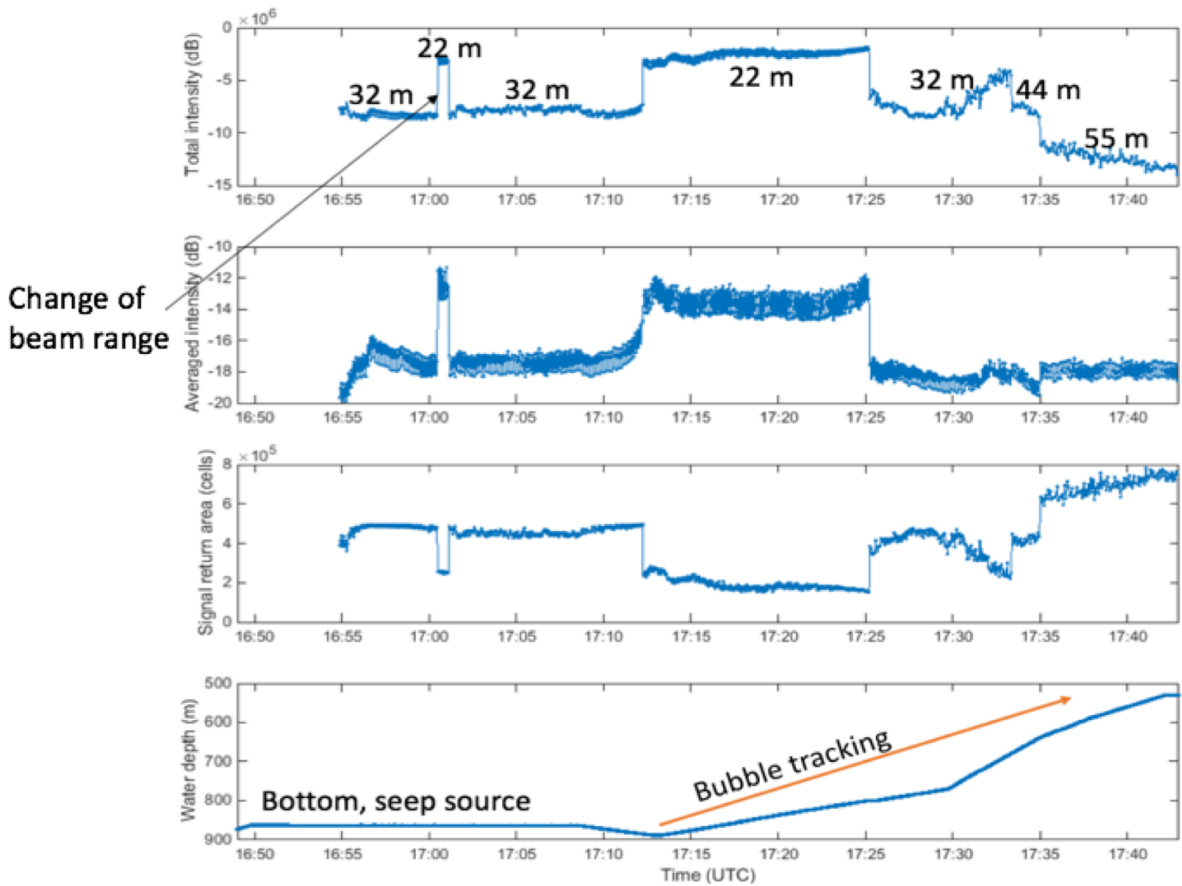


Figure 59: Time series of M3 sonar operation during a profiling survey, including the survey at the seep source and flare tracking through the water column. Panels from top to bottom: 1.) Summation of intensity for all cells that have signal  $> -25$  dB; 2.) Average intensity per cell that has signal  $> -25$  dB; 3.) Total number of cells that have signal  $> -25$  dB; and, 4.) Depth of the sensor (showing seep source survey at 890 m followed by bubble tracking).

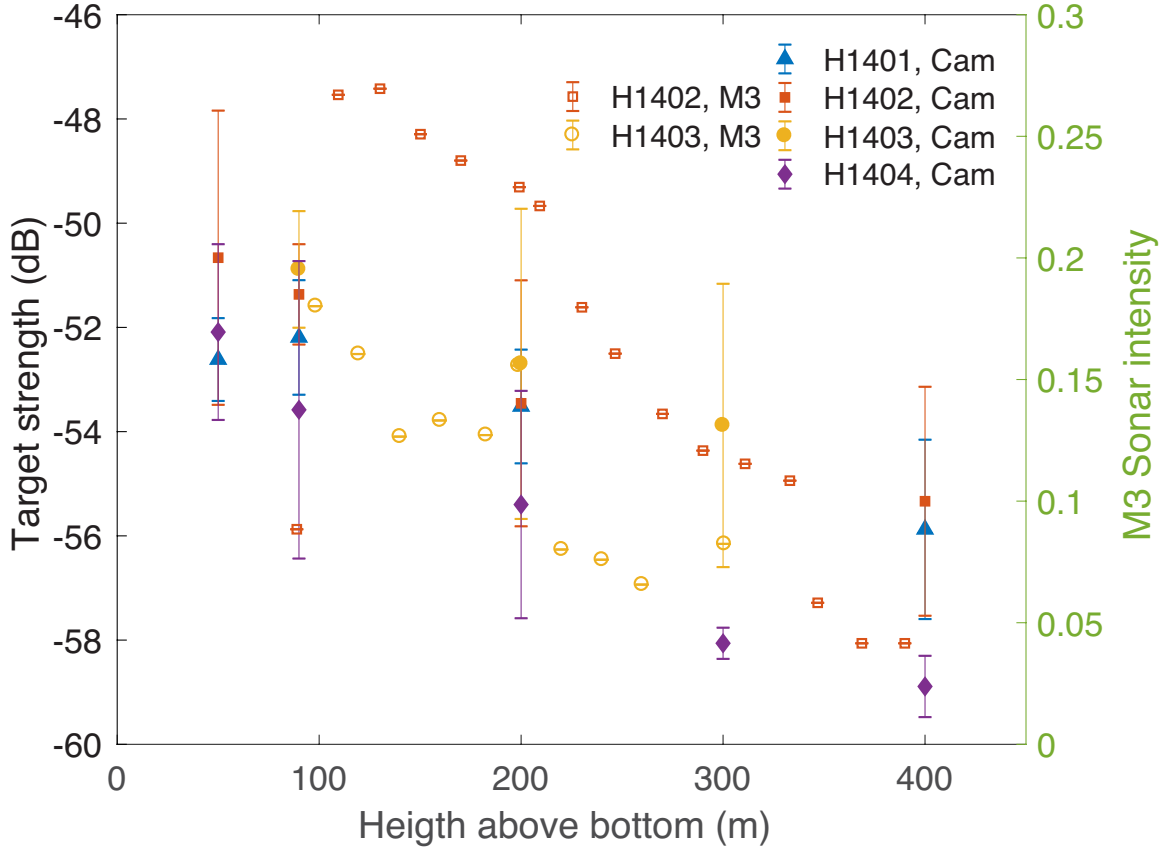


Figure 60: Comparison between the calculated target strength obtained from bubble characteristics observed by the *in situ* cameras and the calculated sonar intensity from the M3 acoustic imaging. The symbols are averaged results from all of the images at each height, and the errorbars show the standard deviation of each data sample.

intensity, scaled by the maximum intensity in each image, or we could convert the raw acoustic data to target strength using an appropriate calibration.

### D.3.1 Calibration of M3 using *in situ* camera observations

To develop a calibration curve between the M3 acoustic data and the bubble characteristics, we utilize the simultaneous high-speed camera data collected from ROV Hercules during the GISR cruises. This was originally reported in our quarterly Research Performance Progress Report for the second quarter of FY2018. This work is repeated here for completeness. This calibration has since been updated and revised, as described in Section 5 of this report, above.

Figure 60 shows the calibration curve we have obtained between the camera observations and the M3 sonar imaging. The optical images were taken at various heights above the seafloor (see data reported in Appendix B). From this imaging data, we are able to determine the bubble sizes

and the total number of bubbles in the sample volume. Then, the overall target strength from insonification of all bubbles can be estimated from the target strength equation

$$TS = 10 \log_{10} \frac{\sigma}{4\pi} = 10 \log_{10} \frac{a^2}{(f_R/f - 1)^2 + \delta^2} \quad (33)$$

where  $\sigma$  is the backscatter cross section,  $a$  is bubble radii which are determined from the images,  $f = 500$  kHz is the sonar frequency of the M3,  $f_R$  is the resonance frequency of the bubble, and  $\delta$  is a damping coefficient due to energy loss. We follow (Medwin and Clay, 1998) for calculation of the damping coefficient and the resonance frequency of the bubble.

The target strength from Equation (33) for each bubble is computed in log scale. To add the contributions for all bubbles in a sample volume together, we convert to linear scale, perform the summation, and then report the final result again in log scale to produce the results in the figure.

For the M3 sonar images, the insonifications were recorded by the sonar receiver, filtered and amplified based on unknown factors and gains applied by the manufacturer. Therefore, it was not possible to determine the true target strength from the M3. However, the arbitrary intensity from the sonar images provides useful quantitative information about the bubble scatter. Following a similar procedure as for the optical image data, we converted the arbitrary intensity values to linear scale, summed all samples, and then converted back to log-scale. In Figure 60, these results are plotted against the target strength calculated from the optical images. Here, only ROV dives H1402 and H1403 have enough acceptable data for comparison. Although the sonar intensity results could not yet be compared to theoretical values without further laboratory calibration (as was performed in Task 5, see Section 5, above), we still observe the overall decreasing backscatter from the seep bubbles away from the seafloor in both the camera images and the M3 data. Hence, our synchronized acoustic and camera datasets record the shrinkage of the bubbles as they rise above these natural seeps.

### D.3.2 Other quantitative aspects of the M3 data

Aside from obtaining a true calibration for acoustic backscatter for the M3 sonar, some of the most valuable quantitative data from the M3 are already depicted in Figure 57. These additional metrics include the shape and size of the flare cross-sections, which is recorded as a function of height throughout a survey. We can further analyze the relative intensity of the bubble cloud in the acoustic data, as shown in Figure 61. Plotting the data this way, we can also see the acoustic data for the bubble flare separately from the echo coming from the *Argus* vehicle. Here, the *Argus* signal is an abrupt peak in the intensity that scales with the size of the vehicle (about 3 m long and

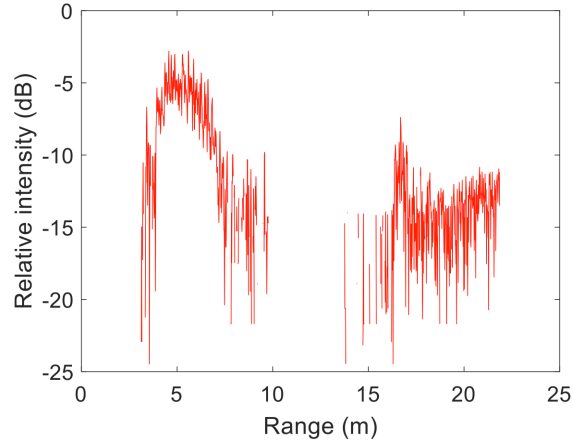


Figure 61: Range-averaged relative intensity of bubble scattering in the M3 sonar field-of-view after removing all noise (signal  $< -25$  dB).

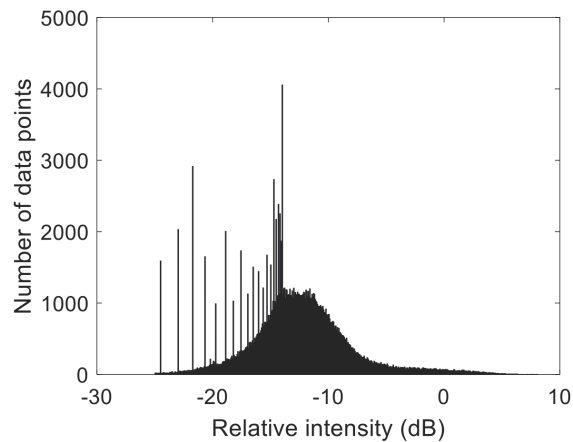


Figure 62: Histogram of relative intensity of bubble scattering in the Sonar field-of-view after removing all noise (signal  $< -25$  dB).

1 m wide), seen in Figure 61 at a range of about 17 m. The width and distribution of the relative acoustic intensity in the bubble flare region gives further information on the relative abundance of bubbles as a function of range away from the instrument.

We can also compute the statistical distribution of the intensity values for the bubble flare only. Figure 62 shows the frequency histogram of relative intensity for the data in Figure 57 after thresholding at  $-25$  dB. The distribution is close to Gaussian, with a few large spikes in the lower tail of the distribution. These spikes may relate to small-scale features in the acoustic image, such as the umbilical between *Hercules* and *Argus* or between *Argus* and the surface vessel, the *E/V Nautilus*. The mean and standard deviation of this distribution will be useful for estimating the width of the bubble size distribution when comparing to an appropriate acoustic model. Hence, these examples demonstrate the types of quantitative data that can be extracted from the M3 echo

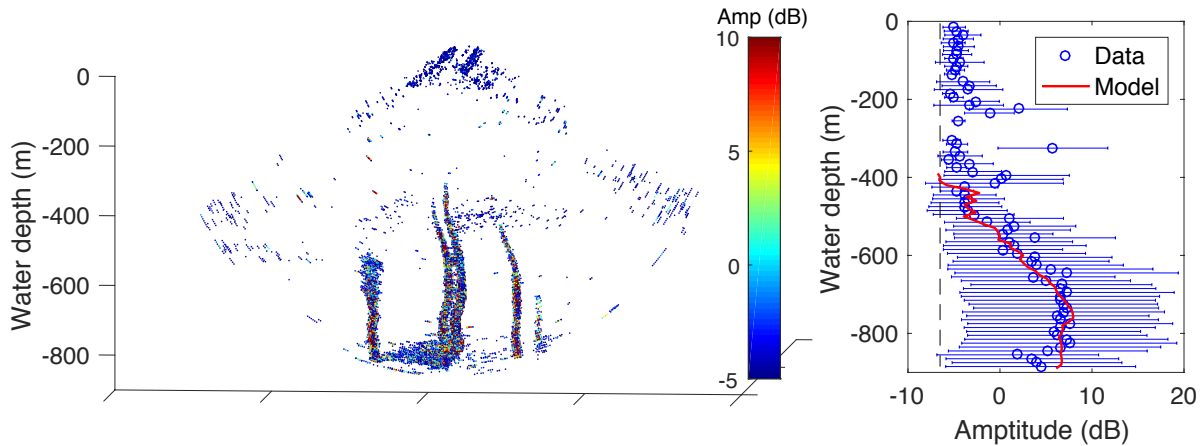


Figure 63: Comparison of the observed acoustic backscatter from the EM 302 with the predicted target strength of bubbles as a function of height from a simulation of the same flare using our numerical model.

sounder using our Matlab analysis routines. Each of these metrics was valuable for validating our numerical model of a seep plume in Task 6 of the project (see Section 5 of this report).

#### D.4 Comparison of Acoustic Measurements with Model Predictions

In this section, we have present examples of how this acoustic data can be used to compare with predictions from our numerical model. For the numerical model predictions, we compute the evolution of the bubble properties as they rise through the water column (hydrate formation, bubble size, dissolution, changes in density with depth, etc., see Section 4 for details). We then use the acoustic models in (Weber et al., 2012) and (?) to convert the simulated bubbles to an equivalent target strength. Finally, we compare the predicted target strength with the acoustic measurements from the EM 302 and M3 echo sounders.

As presented in Figures 54 to 56, we can identify individual bubble flares in the EM 302 acoustic data, convert the acoustic data to equivalent target strength, and isolate the target strength data for one flare of interest. In Figure 63 we show a similar analysis using the uncalibrated acoustic backscatter. In the left-hand panel, the watercolumn data from the EM 302 is shown after thresholding to remove the background noise, and in the right-hand panel, the laterally-averaged acoustic backscatter is plotted as data (similar to the profile in Figure 56 above) with the predicted acoustic backscatter from our numerical model. For the comparison in Figure 63, we are using the uncalibrated acoustic data, and we scaled the numerical model output to give an equal average value. In subsequent work, we replaced the raw acoustic data with the converted target strength, which makes the comparison more quantitative and allowed us to use the numerical model data

to estimate seep flow rates, which can be compared with the measurements of the seep flow rates made using the optical camera system. This more quantitative analysis has been reported in (Wang et al., 2020).

The acoustic data from the M3 are used in multiple ways. One example is to compare the spatial distribution of bubbles in the cross-sectional data from the M3 with predictions from the model. Figure 64 shows several cross-sections at different heights for one survey at MC 118 during the G08 cruise together with model predictions. The panels on the left show the relative frequency of the M3 sonar images after thresholding to remove the background noise; the panels on the right show the target strength prediction for our numerical model. This comparison demonstrates whether the numerical model is spreading the right amount in each direction, whether the bubbles are dissolving correctly to reduce the target strength with height, and can be also compared to optical camera observations at several measurement heights (see data reported in Appendix B). We can further compare the statistics of the measured relative response and predicted acoustic response using statistical distributions similar to Figures 61 and 62. In other work, we have also analyzed the lateral spreading data for each M3 image to estimate the lateral turbulent diffusivity (see results in (Wang et al., 2020)). Hence, both acoustic datasets (the EM 302 and M3 echo sounders) yield valuable quantitative metrics for validation of our numerical model, as reported in detail in Section 5 of this report.

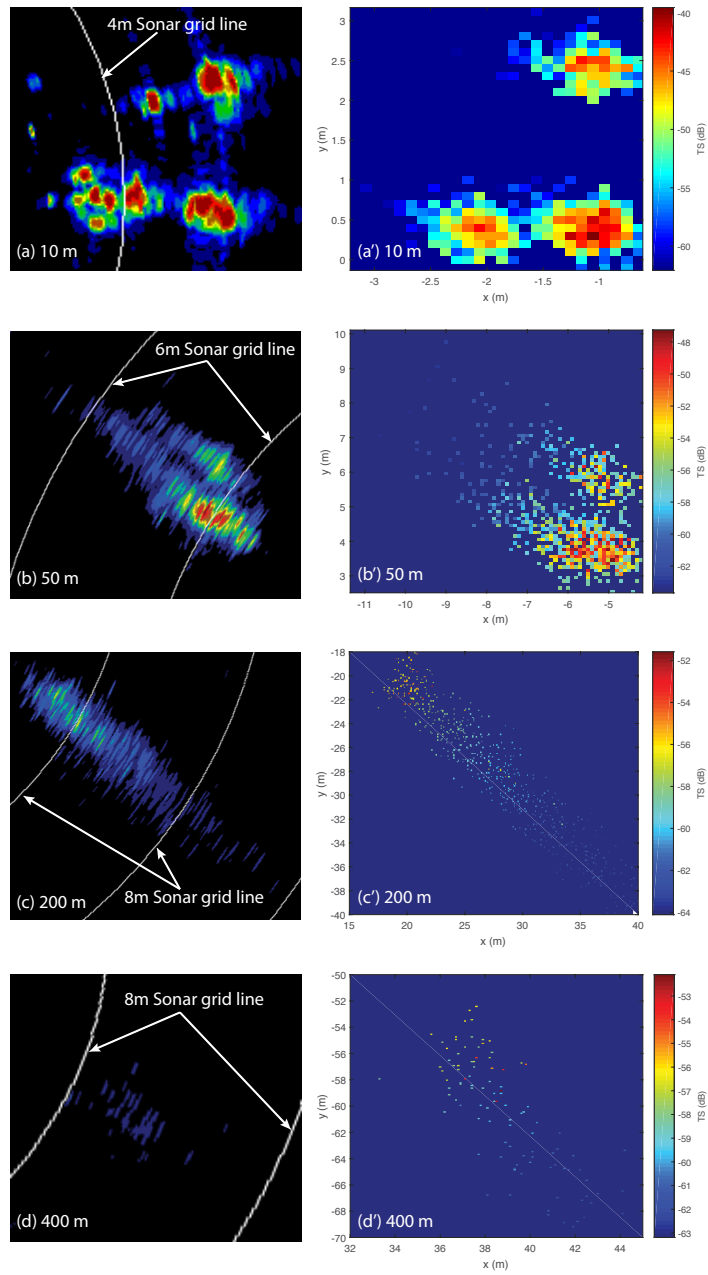


Figure 64: Comparison of the M3 raw acoustic backscatter after thresholding to remove noise to the predicted target strength of bubbles at each measured height from a simulation of the same flare using our numerical model.

## D.5 Matlab Scripts

We provide our Matlab acoustic analysis scripts in Digital Appendix D, included with this report. The top-level directory of this Appendix contains separate directories for the **EM302** and **M3**. Under each of these directories, the **./Toolbox** directory contains the Matlab function files that make up the analysis toolbox and the **./Sample\_scripts** directory contains **.m**-files that demonstrate the usage of these toolboxes and that created the figures presented in this report. Each toolbox and sample script is self documented.

## D.6 Amplitude Level in EM Water Column Datagram

Author: Ragnar Eckhoff

Date: 2008.01.02

Version: 1.0

The sonar equation is

$$EL = SL + TS - 2TL \quad (34)$$

where  $EL$  is the received echo level,  $SL$  is the transmitted source level,  $TS$  is the target strength, and  $TL$  is the one-way transmission loss. The transmission loss is

$$2TL = 2\alpha R + 40 \log R \quad (35)$$

where  $\alpha$  is the absorption coefficient (dB/m) and  $R$  is the slant range (m).

In the water column datagram, the received echo level is adjusted for system dependent parameters in addition to being amplified with a range dependent TVG function:

$$A_{WC} = EL - SL - 10 \log \Omega_{TX} \cdot \Omega_{RX} + 2\alpha R + X \log R + C \quad (36)$$

Default values for  $X$  and  $C$  are 30 and 0 (both values are included in the Water Column datagram).  $\Omega_{TX}$  and  $\Omega_{RX}$  are along-track (transmit) and across-track (receive) beam widths (radians). The values can be found in the Runtime Parameters datagram (Example: EM 3002:  $\Omega_{TX} = \Omega_{RX} = 1.5^\circ = 0.026$  rad).

By comparing the formulas for  $EL$ ,  $2TL$ , and  $A_{WC}$ , we find the following relationship between the latter and  $TS$ :

$$A_{WC} = TS - 10 \log \Omega_{TX} \cdot \Omega_{RX} + (X - 40) \log R + C \quad (37)$$

We use this equation to obtain true target strength  $TS$  from the EM 302 dataset.

## E Rise Heights of Bubble Flares for the GISR Cruises

As part of Tasks 3 and 4, we measured the rise heights for each of the seeps surveyed through the GISR G07 and G08 cruises to MC 118 and GC 600 in 2014 and 2015. Here, we report the final results of this analysis. These results are used in the model validation, as reported in Section 4 of this report.

Bubble flare rise heights were estimated by interrogating the EM 302 multibeam echosounder data for the water column anomalies, as described in Appendix D. Raw data are available as described in Table 6 of this report.

The EM 302 surveys and related model data were collected as follows. First, the ROV *Hercules* surveyed the seep source at the sea floor, and stereoscopic camera images were collected, which provided bubble size distributions and gas flow rates (see Appendix B). Second, following the end of the ROV dive, the ship performed EM 302 surveys traversing the seep site for several hours. Here, we collect the data for several surveys together into a set of superposed acoustic images depicting the bubble flare over several passes of the EM 302 sonar. We group together surveys for which the water column anomalies were similar. Table 9 reports the ship track numbers and data collection times for each sequence for the G07 (July 2014) cruise, and Table 10 reports this data for the G08 (April 2014) cruise.

Table 9: The combined survey periods for acoustic surveys during the G07 cruise.

Category	Shiptracking	Date	Time
1	1 – 2	20140719	14:02:54 – 16:47:18
2	3 – 5	20140719	16:56:23 – 18:15:27
3	6 – 7	20140719	18:57:54 – 20:20:12
4	8 – 11	20140719	20:32:11 – 23:16:11

Figure 65 shows the acoustic anomalies for each combined survey sequence during the G07 cruise. Figure 66 shows the same combined survey results for observations during the G08 cruise.

The rise height of the bubble flare used in the model validation is taken as the highest point of acoustic anomaly in each of these sequence images.

Table 10: The combined survey periods for acoustic surveys during the G08 cruise.

Category	Shiptracking	Date	Time
1	1 – 3	20150410	16:27:57 – 18:03:28
2	4 – 6	20150411	06:40:39 – 08:37:57
3	7 – 13	20150411	08:46:39 – 11:56:25
4	14 – 18	20150411	13:30:01 – 15:48:39
5	19 – 21	20150413	05:59:46 – 07:58:21
6	22 – 27	20150413	08:08:11 – 11:03:22
7	28 – 29	20150413	11:10:11 – 12:22:56
8	30 – 35	20150414	01:30:01 – 04:55:28
9	36 – 38	20150414	08:03:54 – 09:53:23
10	39 – 42	20150414	10:08:49 – 12:34:58
11	43 – 46	20150416	02:44:54 – 04:46:11
12	47 – 48	20150416	05:54:38 – 06:50:41
13	49 – 51	20150416	10:36:05 – 13:43:33
14	52 – 55	20150418	05:06:31 – 08:35:18
15	56 – 59	20150419	01:38:07 – 06:37:11
16	60 – 61	20150419	10:43:51 – 12:27:53

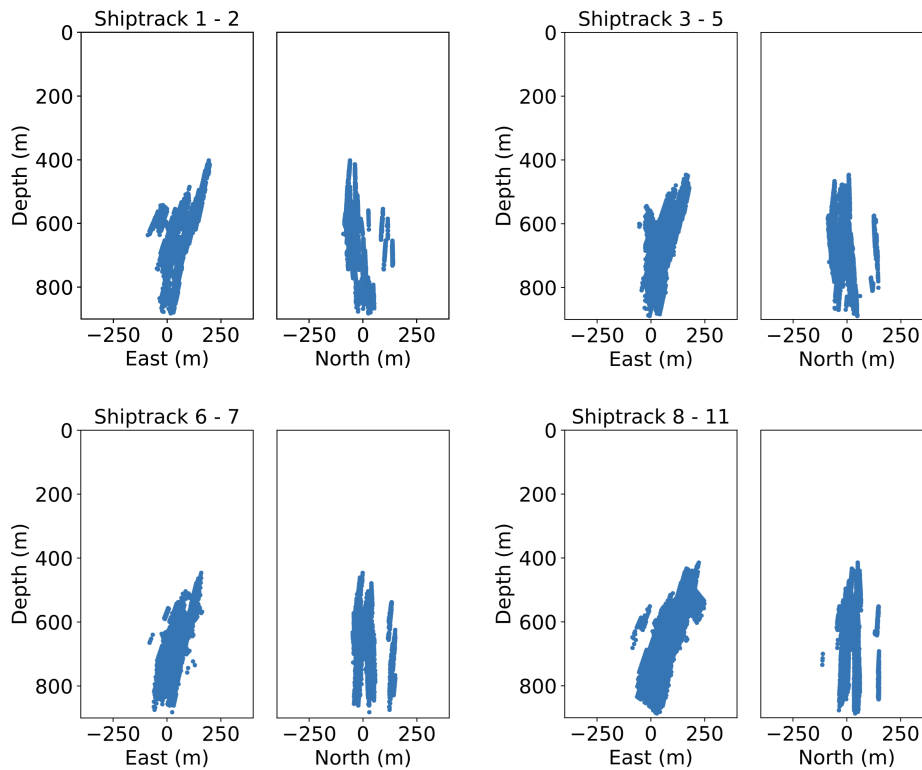
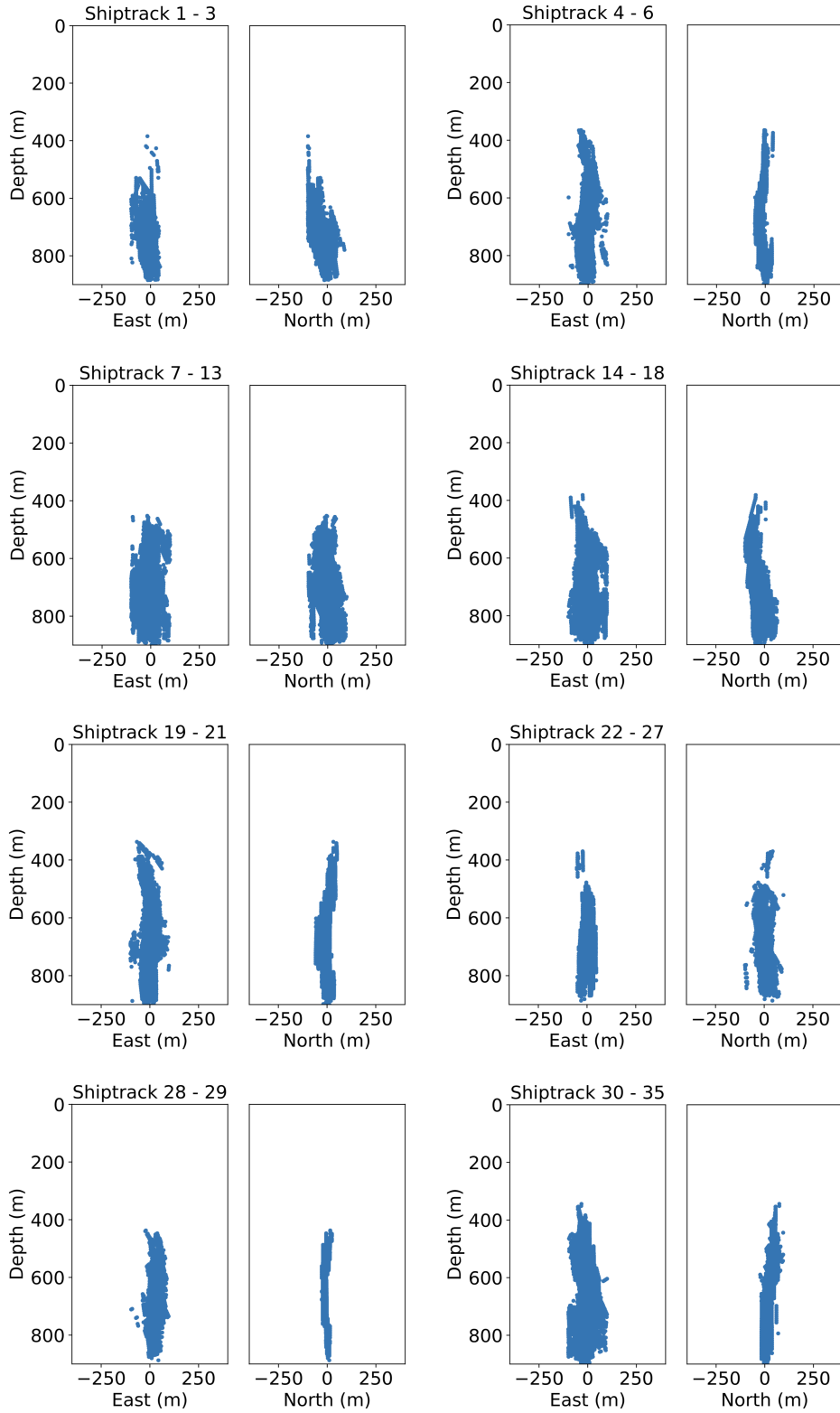


Figure 65: Combined surveys of bubbles emanating from the Sleeping Dragon vent (Woolsey Mound) in MC 118 during the G07 (July 2014) cruise.



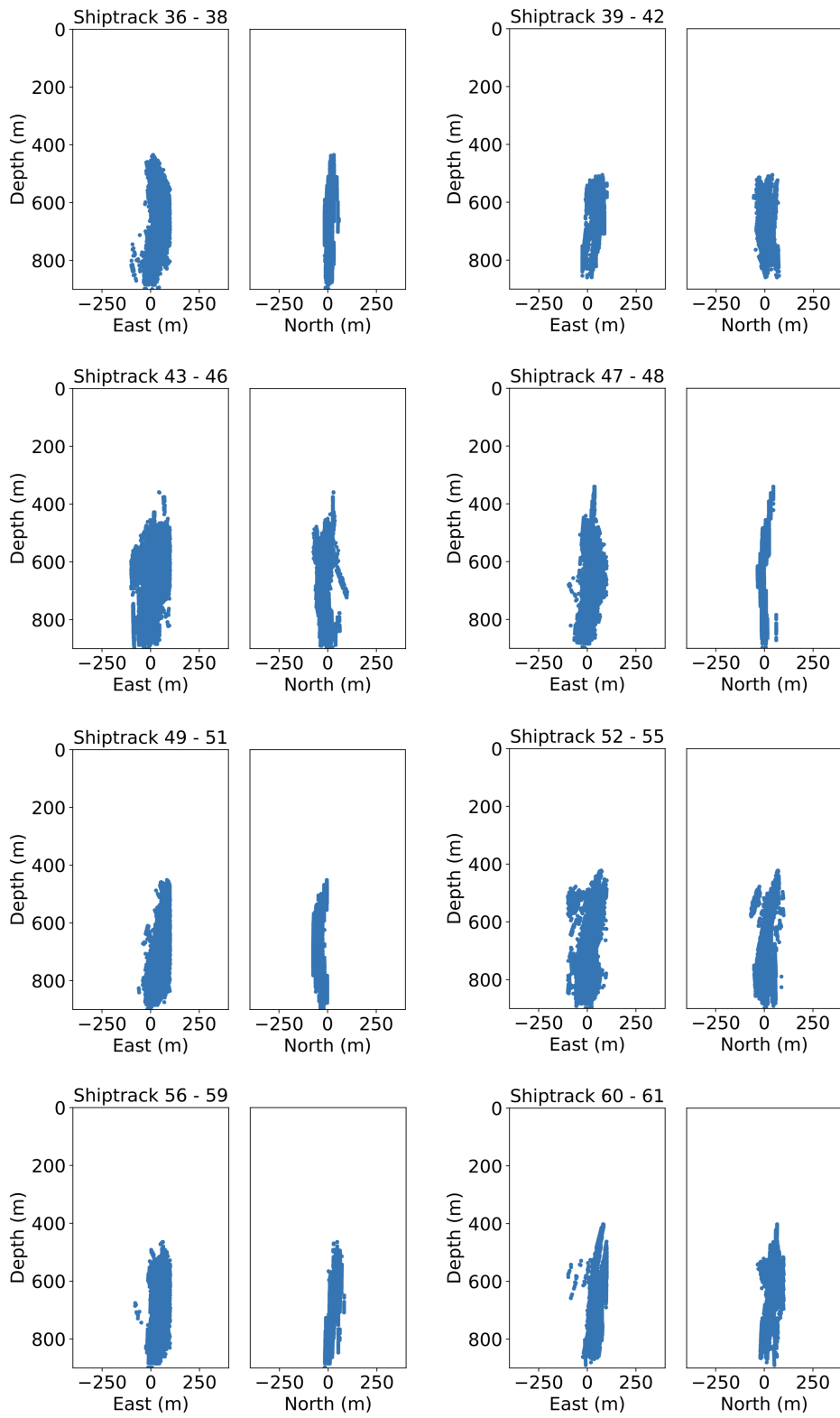


Figure 66: Combined surveys of bubbles emanating from the Sleeping Dragon vent (Woolsey Mound) during the G08 cruise.

## F M3 Calibration Experiment in the Offshore Technology Research Center

To develop a calibration curve between the M3 acoustic multibeam raw data and acoustic target strength of a bubble column, we conducted new experiments in the Offshore Technology Research Center (OTRC), using an M3 sonar and synthetic natural seep bubble flares. Our technical report summarizing the methods and results of these experiments follows.

### F.1 Introduction

During the field experiments of the Gulf Integrated Spill Research (GISR) program, acoustic data were collected in the field using a hull-mounted EM-302 multibeam echosounder and an M3 multibeam sonar mounted on a remotely operated vehicle (ROV). These instruments imaged the acoustic signature of natural seep flares in the ocean water column at two sites in the Gulf of Mexico: Green Canyon lease block 600 (GC 600) and Mississippi Canyon lease block 118 (MC 118). The EM-302 is a field-scale instrument, and some calibration information is available from the manufacturer. The M3 is designed to measure at smaller scale (as little as a few meters using a 500 kHz acoustic beam), and it is possible to test and calibrate an M3 in large-scale laboratory experiments. In order to obtain more quantitative information on bubble properties and concentration for the field data collected through the GISR cruises, we conducted calibration experiments for the M3 sonar in the Offshore Technology Research Center (OTRC).

The OTRC is a large-scale wave, wind, and current testing basin housed at the Research Park at Texas A&M University. This basin is part of a Texas A&M Engineering Experiment Station (TEES) Center and primarily serves clients designing floating structures in the Gulf of Mexico. The basin is 45.7 m long, 30.5 m wide, and has a nominal depth of 5.8 m. In the center of the basin there is a deep pit that measures 9.1 m in length, 4.6 m in width, and extends to a total depth of 16.8 m. For the present project, we created bubble plumes with similar gas flow rate and bubble size distribution to the seeps measured by GISR in the deep Gulf of Mexico. These plumes originated from the base of the deep pit. We positioned an M3 sonar to view the plume in cross-section, and measured the bubble plumes at 12.0 m above the pit floor. This configuration (imaging plume cross-sections) matches the way the M3 was used on the ROV during the GISR experiments.

We conducted two different types of measurements with the M3 in the OTRC basin. To calibrate the acoustic properties of the M3, we used a tungsten carbide sphere and placed the sphere throughout the measurement domain of the M3. To test our calibration and validate our acoustic models, we also measured the acoustic signatures of several gas bubble plumes.



Figure 67: Tungsten carbide calibration sphere.

For the gas bubble plumes, two different gas injection diffusers were used at five different flow rates each, for a total of 10 different experimental conditions. We measured the gas bubble size distribution at a position 11.45 m above the air source using an *in situ* CCD video camera. The camera provides the bubble sizes and shapes, their rise velocity, and the gas concentration. For the same experimental conditions, we also measured the acoustic signature of each plume using the M3, located about 4 m away from the plume and sampling the cross-section 12.0 m above the plume source. Acoustic models together with the M3 calibration data allow us to estimate the gas concentration from the M3 measurements. These are compared to the *in situ* images to validate their performance. The details of each experimental run are provided in Section F.5.

These experiments were conducted from February 25 to March 4, 2019. The remainder of this report describes our experimental methods in more detail and presents typical experimental results.

## F.2 M3 Calibration

To develop a calibration curve for the M3 multibeam sonar, we needed to image a known object throughout the measurement plane of the instrument. This is typically done using tungsten carbide ball bearings since these materials are well characterized and the ball bearings are manufactured to a tight tolerance. Figure 67 shows a pictures of the calibration sphere used in these experiments. The sphere is held in place by a fishing line and net. In our calibration experiments, we positioned the sphere throughout the measurement domain of the M3 sonar.

Figure 68 shows a typical M3 sonar image of the calibration sphere. In this image, the sphere was positioned about 4.5 m away from the M3 at an angle of zero degrees to the beam head. The bright spot in the M3 image at this location registers the acoustic response of the calibration sphere. Other, weaker spots evident in the image, especially those at about  $50^\circ$ , are background noise, weak targets, and some basin ringing that may alias the calibration sphere.

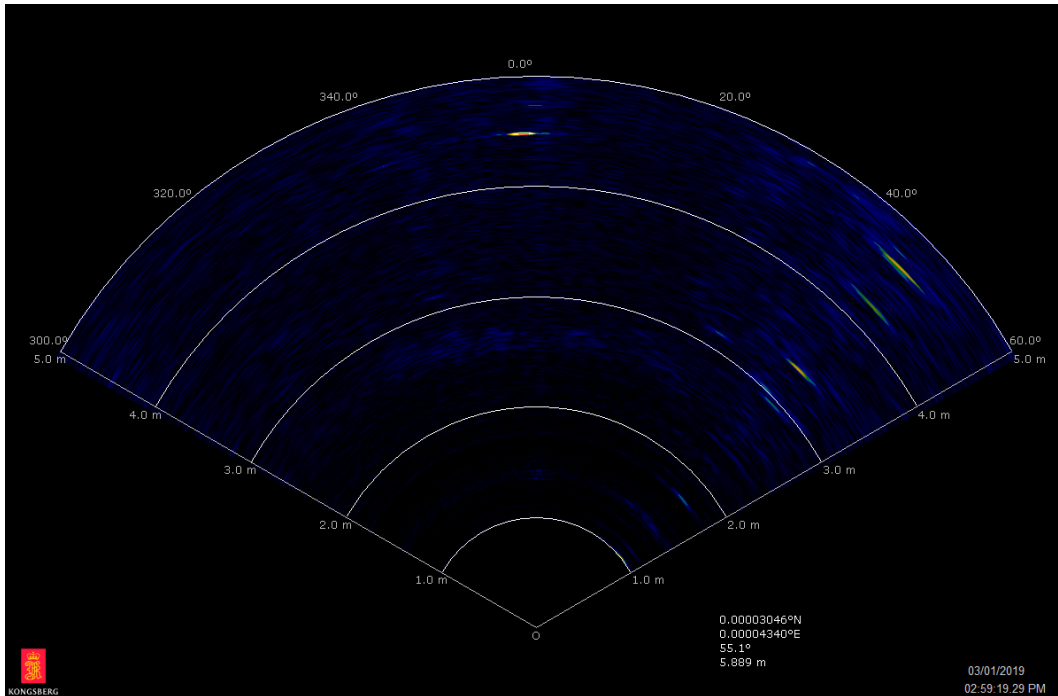


Figure 68: Acoustic image from M3 of the calibration sphere at a single location.

To complete the calibration, the sphere was moved throughout the measurement domain. These data allowed us to understand the uncalibrated acoustic intensity of the measured signal and to convert it to a calibrated value. Using this calibration curve, measured acoustic responses of bubble plumes can be converted to real acoustic backscatter intensity and, thereby, related to the bubble properties and concentration.

### F.3 Application of M3 to Laboratory Bubble Plumes

To validate our acoustic models of bubbles in the M3 measurement plane, we conducted experiments with two different bubble diffusers and five different air flow rates. The bubble diffusers were a standard aquarium airstone and a single orifice. The airstone produces a fairly narrow bubble size distribution, and the dynamics of airstone plumes have been well studied in other laboratory experiments. The single orifice was a straight hole 0.5 mm in diameter at the end of a pressurized bulkhead. This orifice produces a broader bubble size distribution. Both diffusers produce bubbles in the size ranges observed in the deep Gulf of Mexico.

Figure 69 shows a typical M3 acoustic image of one of the bubble plumes at 11.45 m height above the plume source. This image is for an airstone diffuser at a nominal gas flow rate of 3.0 Nl/min at standard conditions. The bubble plume is the strong, textured signature at zero degrees to the M3 axis.

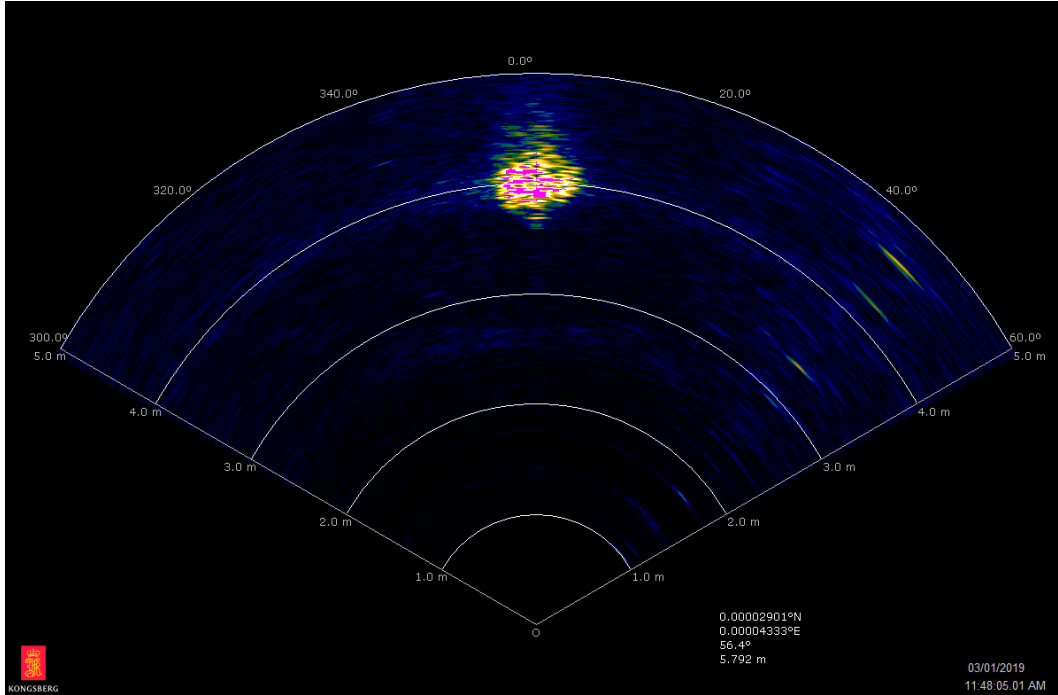


Figure 69: Acoustic image from M3 of an airstone bubble plume at 3.0 NI/min gas flow rate at 12.0 m above the source.

The images obtained at the OTRC are very similar to those observed in the field. As an example, Figure 70 shows an image of a seep bubble plume at MC 118 taken at 190 m above the sea floor (700 m depth). In both images, the bubble plume occupies a similar area within the measurement plane and has a similar acoustic shape. For the example in the laboratory, the scale was smaller and the acoustic amplitude is larger. However, the two images have otherwise very similar characteristics. Images taken closer to the seep source in the field appear similar in intensity to those in the laboratory. Hence, we were very satisfied with the quality of the acoustic data in the laboratory and observed no influence of the confinement of the tank walls on the experimental data.

#### F.4 *In Situ* Imaging of Laboratory Bubble Plumes

To test the accuracy of our acoustic models and the calibration curve for the M3, we also measured the bubble size distribution and gas concentration for each diffuser and gas flow rate using *in situ* video imaging. Figure 71 shows a typical CCD camera image for the same experiment as depicted for the M3 in Figure 69 (airstone diffuser at 3.0 NI/min). The camera lens and  $f$ -stop were selected so that only a narrow imaging plane would be in focus within the imaging volume. This is necessary to avoid parallax errors when measuring bubble sizes using a single camera.

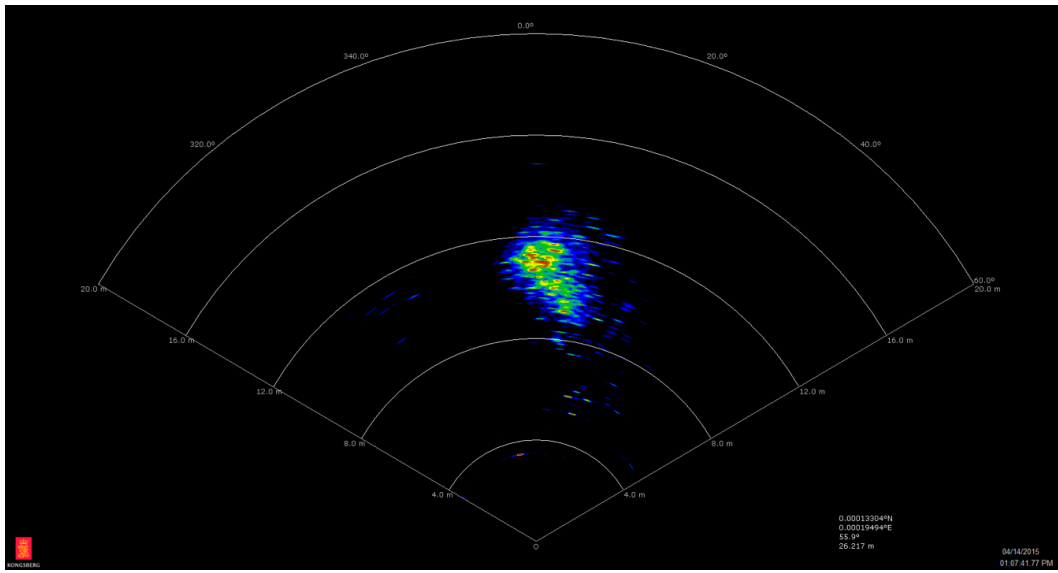


Figure 70: Acoustic image from M3 of a natural seep flare at MC 118 imaged at 190 m above the sea floor (700 m depth).



Figure 71: CCD video camera image of an airstone bubble plume at 3.0 NI/min gas flow rate at 11.45 m above the source.

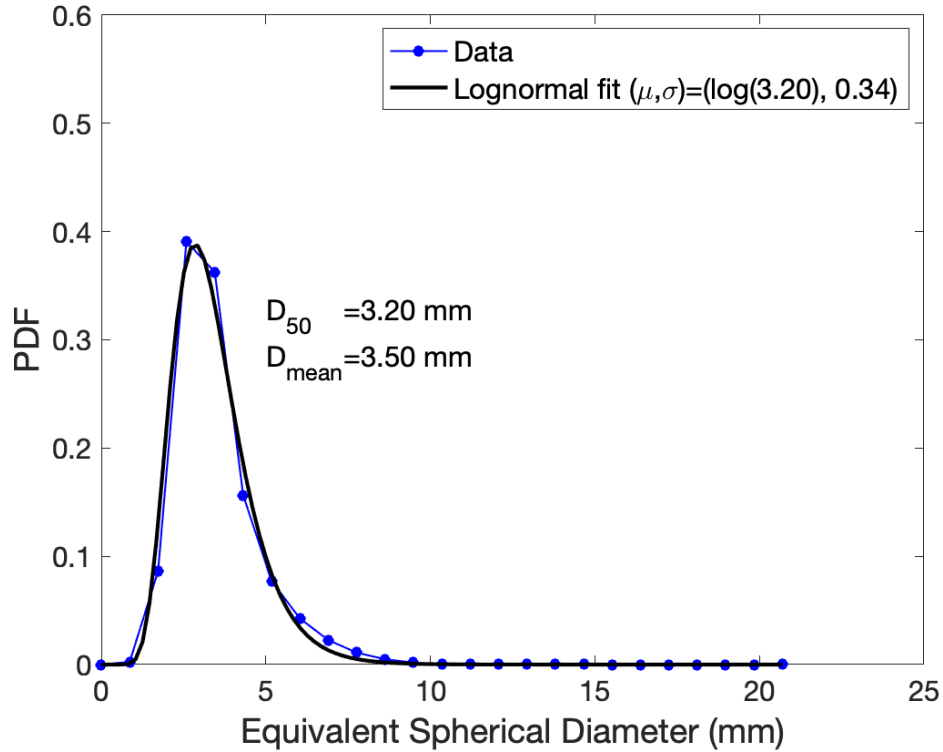


Figure 72: Bubble size distribution for an airstone bubble plume at 3.0 NI/min gas flow rate at 11.45 m above the source.

We applied our image processing tools developed through Task 2 of this project to identify the in-focus bubbles and extract their equivalent spherical diameter. Figure 72 shows the volume size distribution of all measured bubbles within a continuous video sequence of the plume. The bubble size distribution has a volume median diameter of 3.2 mm and conforms well to the log-normal probability density function. This bubble size is in a similar range to the median bubble sizes observed in the field (3 to 5 mm range, see (Wang et al., 2016) and (Wang et al., 2020); see also Appendix B). Bubble concentration data are further obtained by observing the percentage of time each image pixel is within a bubble.

### F.5 Experimental Matrix

The complete experimental matrix with sample raw data is provided in the included Excel spreadsheet (Digital Appendix F). This matrix includes the following columns:

- **SN.** Sample number. Unique numbers for each experiment.
- **Sortable Date.** Date the data were collected in yyyyymmdd format.

- **Data Type.** Describes the measurement platform; these are:
  - **M3.** Data were collected using the M3 sonar.
  - **Bubble Size Distribution (BSD).** Data were collected using the *in situ* CCD video camera.
- **Height from OTRC pit bottom (m).** Distance from the air diffuser source to the measurement plane.
- **Diffuser Type.** Reports the diffuser used in the experiment; either an aquarium airstone or a single orifice.
- **Designated Flowrate.** The normal air flow rate (Nl/min) of air planned for each experiment.
- **Measured Flowrate.** The actual, normal air flow rate (Nl/min) measured during each experiment.
- **Observ. Time.** Duration of the measurement in mm:ss format.
- **Raw data file address.** Directory where the raw data were stored on the data archive.
- **Description.** Includes comments unique to each experiment. Sometimes this column is blank; in that case, the other columns are self-explanatory for describing this experiment.
- **M3 Sample Image.** A single snapshot of the M3 image record.
- **Bubble Sample Image.** A single image of the CCD camera video sequence.

## National Energy Technology Laboratory

626 Cochrans Mill Road  
P.O. Box 10940  
Pittsburgh, PA 15236-0940

3610 Collins Ferry Road  
P.O. Box 880  
Morgantown, WV 26507-0880

13131 Dairy Ashford Road, Suite 225  
Sugar Land, TX 77478

1450 Queen Avenue SW  
Albany, OR 97321-2198

Arctic Energy Office  
420 L Street, Suite 305  
Anchorage, AK 99501

Visit the NETL website at:  
[www.netl.doe.gov](http://www.netl.doe.gov)

Customer Service Line:  
1-800-553-7681



U.S. DEPARTMENT OF  
**ENERGY**

**NATIONAL ENERGY  
TECHNOLOGY LABORATORY**